COMPUTATIONAL PREDICTIVE MODELING OF A NOVEL PULMONARY VALVED CONDUIT

Rick van Tunen

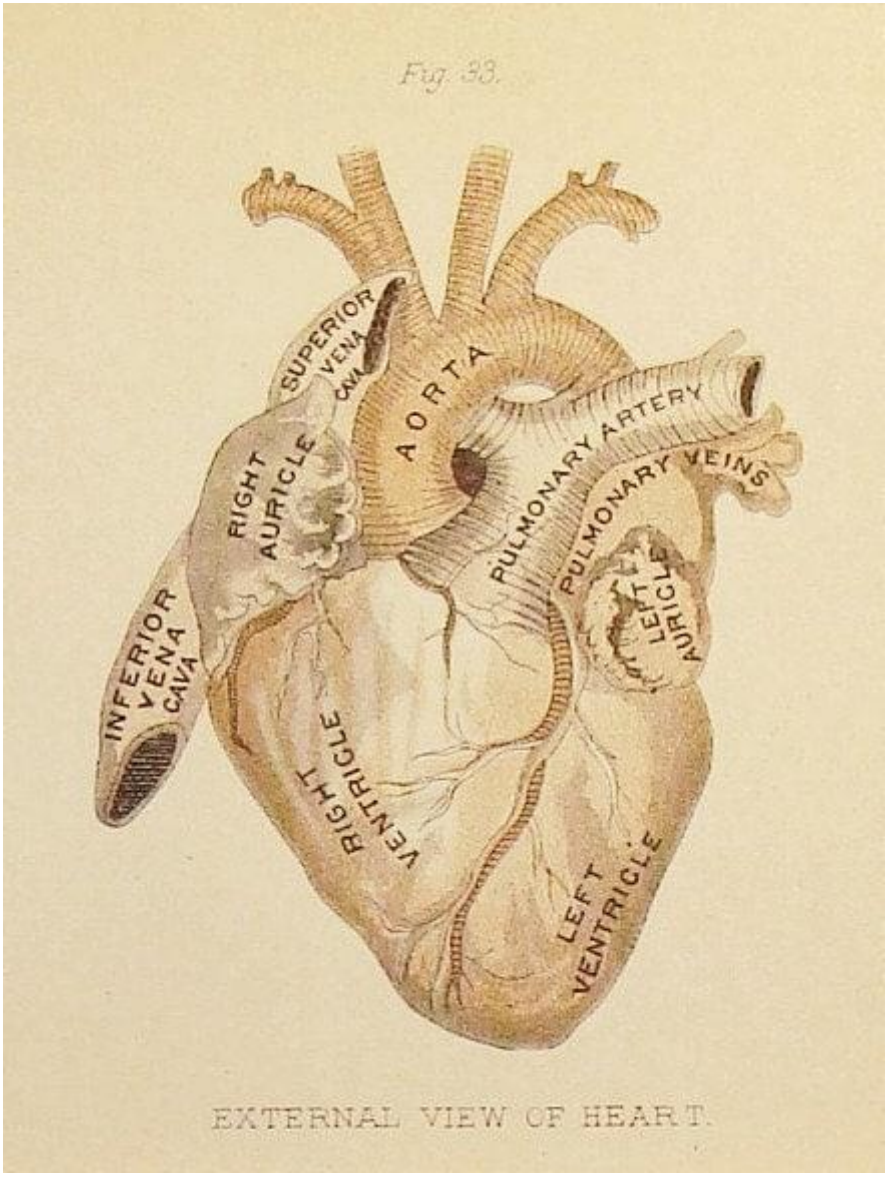

TU Delft

Cover image from (1)

COMPUTATIONAL PREDICTIVE MODELING OF A NOVEL PULMONARY VALVED CONDUIT

By

Rick van Tunen

in partial fulfilment of the requirements for the degree of

Master of Science
in Biomedical Engineering

At the Delft University of Technology,
to be defended publicly on Thursday, October 26, 2023, at 12:30.

Thesis committee:	Dr. ir. M.J. Mirzaali,	TU Delft
	Dr. ir. M. Peirlinck,	TU Delft
	Dr. ir B. Fereidoonnezhad,	TU Delft
	Dr. ir N. Götzen	4RealSim™
Additional supervisor:	Ir. Tahir Turgut	4RealSim™

This thesis is confidential and cannot be made public until October 26, 2025.

PREFACE

This project was definitely challenging. During this project, I learned a lot. From performing FE simulations to performing the experiments in the lab. In the end, I am proud of the results and the knowledge I gained. I hope I can share some of that knowledge with you, the reader, and I hope you have fun reading it.

I could not have done it without the help of a lot of people. Specifically, I would like to thank Dr. ir. Mohammad J. Mirzaali for the advice and feedback on designing the experiments and doing research. I would like to thank Dr. ir. Mathias Peirlinck for the advice and feedback for the simulations and for providing knowledge on cardiac simulations, I learned a lot. I would also like to thank Sander Leeflang for helping me perform the experiments and brainstorming about the experiment design. Furthermore, I would like to thank everyone at 4RealSim™, specifically Dr. ir. Nils Götzen for the feedback and advice on performing the simulations and Ir. Tahir Turgut for helping me with the simulations so they actually work in the end.

I would also like to thank Anindya Paramaarti for her emotional support during this time and for listening to my struggles during the project. Furthermore, I would like to thank all my friends Jamie Hoetmer and Joep van der Hagen to name a few for their support. Finally, I would like to thank my family for supporting me during this project.

Rick van Tunen
Delft, October 2023

ABSTRACT

Congenital heart disease (CHD) affects almost 1% of newborns. Right ventricular outflow tract (RVOT) CHD affects 20% of newborns and includes anomalies such as tetralogy of Fallot (TOF) with or without pulmonary atresia, transposition of the great vessels, and truncus arteriosus. All these anomalies require RVOT reconstruction. Prosthetic heart valves are needed to improve the quality of life of patients suffering from CHD. One such prosthetic device is the pulmonary valved Conduit developed by Xeltis™. This study aimed to investigate the difference in the mechanical response of the Xeltis™ pulmonary valved Conduit sizes 16, 18, and 20 (XPV16, XPV18, and XPV20) using mechanical experiments and a predictive finite element model.

Experiments of two load cases, Leaflet opening behavior (LC1) and parallel compression (LC2) have been done where measurements were taken for input parameters used for uncertainty quantification (UQ) in the FE model. Furthermore, the reaction force and displacement were measured to calculate the force values and stiffness values of the device during each experiment. The experiments were replicated with a developed FE model. From the results of the FE model, a metamodel (MM) was developed and a Monte Carlo simulation was performed to retrieve a distribution of the force values and stiffness values obtained in the simulation. Furthermore, UQ was performed and the sensitivity of the input parameters on the force values and stiffness values were quantified. Finally, with an area metric the accuracy of computational finite element (FE) models in simulating the mechanical response observed in the experiments of the Xeltis™ pulmonary valved Conduit size 16, 18, and 20 mm was quantified.

For the Leaflet opening behavior, the reaction force increases when the device size increases while the stiffness doesn't change with device size. As for the accuracy of the predictive FE model, the predictive FE model can simulate the mechanical response of the stiffness with an accuracy of at least 70.7% for the reaction force and at least 50.3% for the stiffness.

For the parallel plate compression, the reaction force and the stiffness increase when the XPV size decreases from size 18 to size 16. Furthermore, the difference between the XPV18 and the XPV20 is smaller for both the reaction force and the stiffness. As for the accuracy of the predictive FE model, the predictive FE model can simulate the mechanical response of the stiffness with an accuracy of at least 37.3% for the reaction force and at least 38.1% for the stiffness.

As for the important variables influencing the mechanical response, the reaction force and the stiffness are influenced mostly by the fiber stiffness of the component that is subjected to the load. Furthermore, the reaction force and stiffness are also influenced by the direction of the fibers. If the fibers are in the same direction as the load, the reaction force and stiffness increase. Although specifically for the Leaflet the amount of material has more influence on the reaction force and stiffness for larger XPV sizes with the Leaflet opening behavior load case. This indicates that for larger XPV sizes the material properties of the Leaflet have a smaller influence and the Leaflet geometry has a higher influence on the stiffness of the Leaflet opening.

Improvements are possible for a better agreement between the simulation and the experiment. These include performing more experiments with different samples from different production batches, and better estimation of input parameters with a high sensitivity to the output parameters.

This study provides a step in the direction of predictive computational device modeling that will help shorten the development time of new pulmonary heart valve devices. As the devices in this study are designed for pediatrics, this will help improve the quality of life of pediatrics suffering from congenital heart disease.

CONTENTS

Preface 4
Abstract 5
1 Introduction 8
1.1 Background 8
1.2 Problem Definition 9
1.3 Study Goal and Research Questions 9
1.4 Thesis Layout 9
2 Materials and Methods 11
2.1 Experimental Setup 11
2.1.1 LC1, Leaflet Opening Behavior 11
2.1.2 LC2, Parallel Plate Compression 14
2.2 Model Geometry 18
2.2.1 Conduit 18
2.2.2 Leaflets 22
2.2.3 XPV Assembly 26
2.2.4 Conduit Forming Assembly 27
2.2.5 LC1, Leaflet Opening Behavior Assembly 28
2.2.6 LC2, Parallel Plate Compression Assembly 29
2.3 Material Model 30
2.3.1 XPV Material Model 30
2.3.2 Experiment Setup Material 34
2.4 Model Definitions 35
2.4.1 Conduit Forming 35
2.4.2 XPV 37
2.4.3 Leaflet Opening Behavior 38
2.4.4 Parallel Plate Compression 40
2.5 Computational Model Data Generation Process 41
2.6 Computational Model Data Generation 42
2.6.1 Leaflet Opening Behavior 43
2.6.2 Parallel Plate Compression 45
2.6.3 Data Processing 46
3 Results and Discussion 47
3.1 Experiment Results 47
3.1.1 LC1, Leaflet Opening Behavior 47
3.1.2 LC2, Parallel Plate Compression 50

3.2 Simulation Results 55
3.2.1 LC1, Leaflet Opening Behavior 55
3.2.2 LC2, Parallel Plate Compression 59
3.3 Model Assessment 63
3.3.1 Validation Metric 63
3.3.2 LC1, Leaflet Opening Behavior 65
3.3.3 LC2, Parallel Plate Compression 69
3.4 Implications on the Research Questions 72
3.4.1 The Mechanical Response of the XPV16, XPV18 and XPV20 72
3.4.2 Capturing the Mechanical Response of the XPV with a Computational FE model 72
3.4.3 The Variables with the Highest Influence on the Mechanical Response of the XPV 73
3.4.4 The Accuracy of the Predictive Finite Element Model 74
3.4.5 The Difference in Mechanical Response based on Experiments and a Finite Element Model 75
3.5 Limitations and Future Directions 77
4 Conclusion 78
Bibliography 79
Appendix A, Leaflet Opening Behavior Experimental Setup 81
Appendix B, LC1 Misalignment Measurements 83
Appendix C, XPV FE Model Pressure Load Case Test 85
Step-2 pre-load 85
Step-3 leaflet opening and closing 86
Simulation Results 87
Appendix D, Material Parameters Description 88
Formulas 88
Undamaged Hyperelastic response 88
Mullins effect 88
Permanent set 88
Viscoelasticity 89
Solver specific 89
Appendix E, LC1 Force Displacement Curves of the Experiments 92
Appendix F, LC2 Force Displacement Curves of the Experiments 95

1 INTRODUCTION

1.1 BACKGROUND

Congenital heart disease (CHD) affects almost 1% of newborns. Right ventricular outflow tract (RVOT) CHD affects 20% of newborns and includes anomalies such as tetralogy of Fallot (TOF) with or without pulmonary atresia, transposition of the great vessels, and truncus arteriosus. All these anomalies require RVOT reconstruction. Furthermore, RVOT reconstruction must be performed after the Ross operation to treat congenital aortic heart valve disease. RVOT reconstruction includes prosthetic valve replacement (1).

There are multiple types of heart valves available. Heart valves can be mechanical where the Leaflets are of a rigid material, such as pyrolytic carbon. Mechanical heart valves provide excellent hemodynamics but have a risk of thromboembolism. Thus, mechanical prosthetic heart valve patients require anticoagulation therapy (3). Figure 1-1 shows multiple mechanical heart valves used for pulmonary heart valve replacement.

Bioprosthetic valves provide a different option where the valves are made of biological tissue and closely resemble the geometry of the native heart valve. These valves are more biocompatible and are less thrombogenic. A significant disadvantage of these valves is the risk of valve degeneration and the potential need for reoperation, but the possibility of a transcatheter delivery procedure of the prosthetic valve reduces this clinical limitation (3). Figure 1-1 shows multiple bioprosthetic heart valves used for pulmonary valve replacement.

More development has been done on developing polymeric tissue heart valves, such as ePTFE valves. These heart valves are showing promising results for pediatric patients (4). Another polymeric tissue heart valve showing promising results is the pulmonary valved Conduit developed by Xeltis™. The device is designed to treat children from age 2 up to adolescents aged 21 with a congenital heart defect of the right ventricle outflow tract. The XPV device is implanted via open chest surgery. Early outcomes of two clinical trials show promising results (5).

The Xeltis™ Pulmonary Valved Conduit (XPV) is made of a porous bioabsorbable polymer material undergoing endogenous tissue restoration (ETR) when implanted in the patient. The material uses the RestorX™ polymer platform where the polymer is built with supramolecular 2-ureido-4[1H]-pyrimidone (UPy) (5).

It is manufactured via electrospinning. Electrospinning fibers are spun around a cylinder forming the component. First, the three Leaflets are manufactured individually and are made of poly-carbonate-based UPy (XP-034), which provides flexibility for Leaflet motion. Afterward, the three leaflets are put in a mold and a poly-caprolactone-based UPy (XP-005) material is electro-spun on top, creating the Conduit. In this way, the Conduit and Leaflets are merged, forming the pulmonary valved Conduit assembly (5).

The electrospinning process results in a porous material that functions as a scaffold for cell growth, enabling ETR. The patient's tissue invades the implant and, while the implant dissolves into the body, the patient's tissue grows into the porous structure of the device (5)(6). This process is schematically shown, together with the device, the microstructure, and the electrospinning process in Figure 1-2.

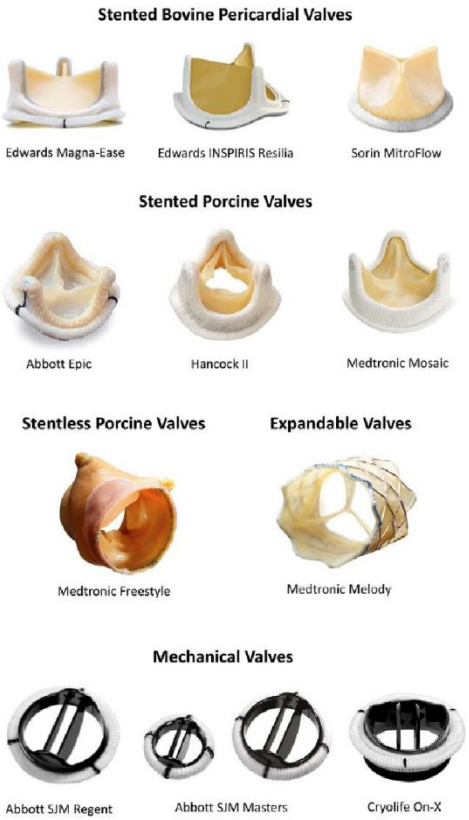

Figure 1-1: Commonly used bioprosthetic and mechanical prosthetic heart valves used (4).

Prosthetic heart valves are needed to improve the quality of life of patients suffering from CHD. For such a device to become available, it must first undergo rigorous testing. The device development, from brainstorming to clinical testing, continues to be refined. One such refinement is the use of computational models for the development of a new device. Computational device modeling can be used to reduce, refine, and replace animal experiments. It should be validated to retrieve reliable information through a computational model (7).

1.2 Problem Definition

Multiple studies have developed a computational model to simulate the mechanics of an aortic prosthetic heart valve and applied different validation strategies to assess the accuracy of the developed computational model (8)(9)(10)(11)-(12)(13). However, the development of a computational model to simulate the mechanics of a pulmonary prosthetic heart valve has not yet been done.

It is estimated that a validated computational model of the XPV is a useful tool to test the safety and performance of the device, allowing for the testing of new designs and shortening its development time. A validated computational model of the XPV predicts the mechanics of the device with sufficient accuracy so reliable data is created. Such a computational model does not yet exist.

1.3 Study Goal and Research Questions

This paper highlights the development and validation of a computational model of the XPV device. Here the following research question will be answered: **What is the difference in the mechanical response of the Xeltis™ pulmonary heart valve conduit size 16, 18, and 20 mm based on mechanical experiments and a predictive finite element model?**

This research question will be answered by answering the following sub-questions.

- How do the mechanical responses of the Xeltis™ pulmonary heart valve conduit sizes 16, 18, and 20 mm differ under two ISO 5840-1 specified mechanical loading conditions?
- To what extent can finite element analysis capture the mechanical responses of Xeltis™ pulmonary heart valve conduits of varying sizes (16, 18, 20 mm)?
- What variables most significantly influence the reaction force and stiffness of the Xeltis™ pulmonary heart valve conduit sizes 16, 18, and 20 mm according to finite element models?
- How accurately can a predictive finite element model simulate the mechanical responses observed in experimental tests on Xeltis™ pulmonary heart valve conduits of varying sizes (16, 18, 20 mm)?

These questions were investigated by performing mechanical experiments with samples from the three different sizes. Furthermore, three computational models were developed of the three XPV sizes.

1.4 Thesis Layout

First, the experimental setup will be described together with the method of data extraction from the experiments. Second, the computational model will be described whereas first the geometry used in the computational model will be described. After the geometry, the material model and material definitions including anisotropy used in the computational model will be described. After the material, the model definitions for the solver, boundary conditions, constraints, and contact will be described. After this, the finite element (FE) simulation workflow is summarized, leading to the desired computational output. Afterward, the processing of the computational data is described. This concludes the description of the computational model and the material and methods sections. The results will be highlighted and discussed in the next section. Here the current state of the art will also be discussed. The findings of the research questions will be discussed here as well. Finally, a conclusion will be given, and the most important findings will be summarized.

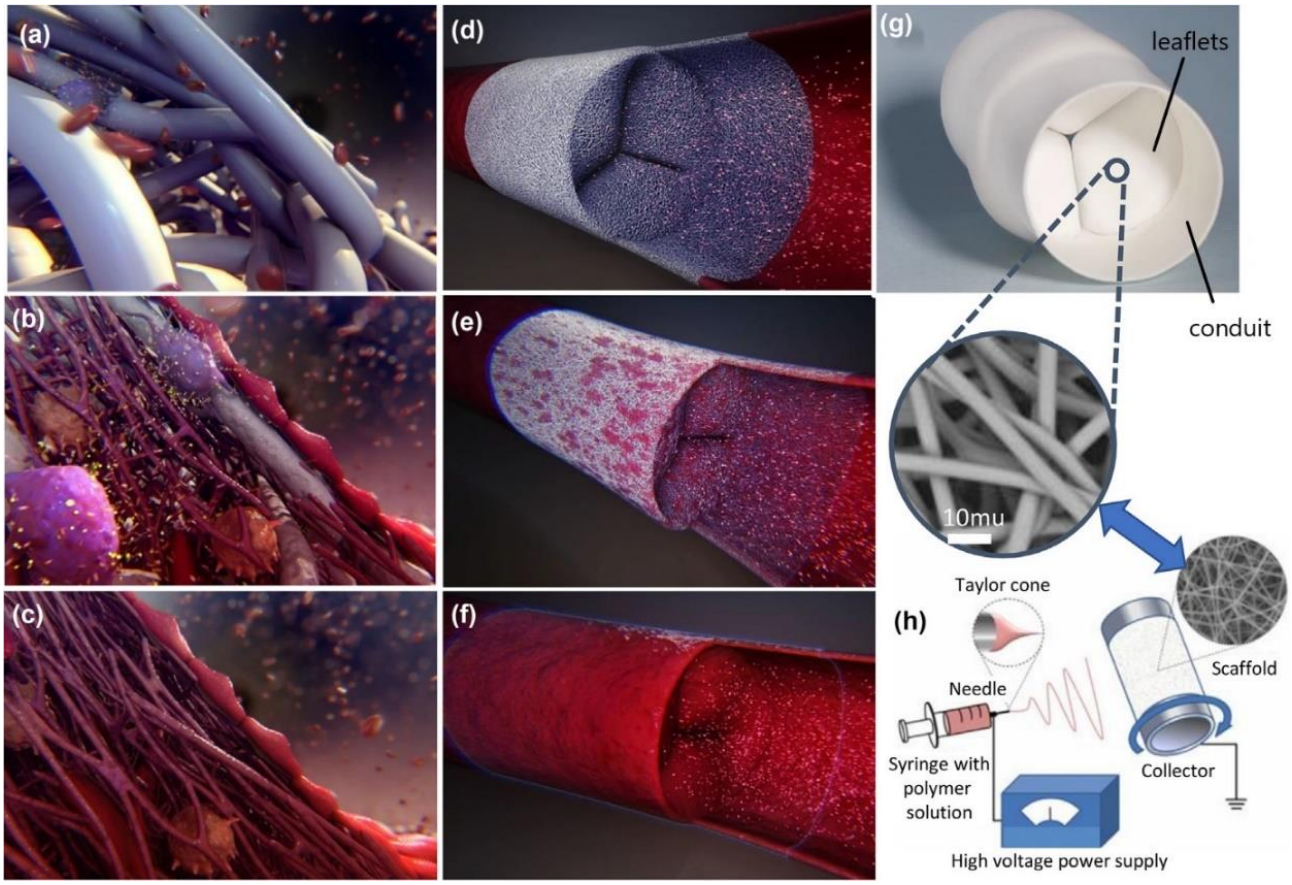

Figure 1-2: ETR process in the XPV at the start (a, d), during ETR (b, e), and after ETR (c,f). Microscopically shown (a-c) and macroscopically shown (d-f). XPV device picture (g) and high magnification Scanning Electron Microscopy inset showing the microstructure, together with the electrospinning process (h) (adapted from (6)).

2 Materials and Methods

2.1 Experimental Setup

To quantify the mechanical behavior of the XPV, two load cases were defined. ISO 5840-1 'Cardiovascular implants – Cardiac valve prostheses – General requirements' (14) provides guidelines for load cases that can be used for design validation. Using load cases from ISO 5840-1 ensures that the load cases considered in this study are realistic. From this, the differential pressures across the valve and transverse compression load cases were considered.

2.1.1 LC1, Leaflet Opening Behavior

Taking guidance from the differential pressures across the valve load case from the ISO 5840-1 'Cardiovascular implants – Cardiac valve prostheses – General requirements' (14), the pressures across the valve are important to validate the opening and closing mechanics of the Leaflets. Because fluid dynamics were not considered, it was decided to replicate the opening and closing behavior of the valve with a cylindrical rod called the Pushrod. The name of this load case is Leaflet opening behavior (LC1).

The Pushrod was pushed through the valve, opening the valve. Afterward, the Pushrod was retracted, which closed the valve. The load case is shown in Figure 2-1. For each device size, a different Pushrod diameter was used to ensure maximum valve opening. Pushrod diameters of 10-, 11- and 12 mm were used for XPV16, XPV18, and XPV20, respectively.

The tests have been done on a Lloyd Instruments LR 5K test machine. With a 5N load cell which has been calibrated by an outside party called Ametek Inc. Based on this calibration the load cell exceeds the requirements of BS EN ISO 7500-1:2015 Class 0.5 and Class 1, ASTM E4 and DIN 51221. Thus, the calibration of the load cell is done successfully. The errors of the load cell for different load levels are shown in Table 2-1.

Table 2-1: Load cell measured values in comparison to the true values on multiple load levels.

Load level (%)	True Value (N)	Measured Value (N)	Error (%)
Zero	0	0.0000	0.000
20%	1	1.0001	0.010
100%	5	5.0059	0.118

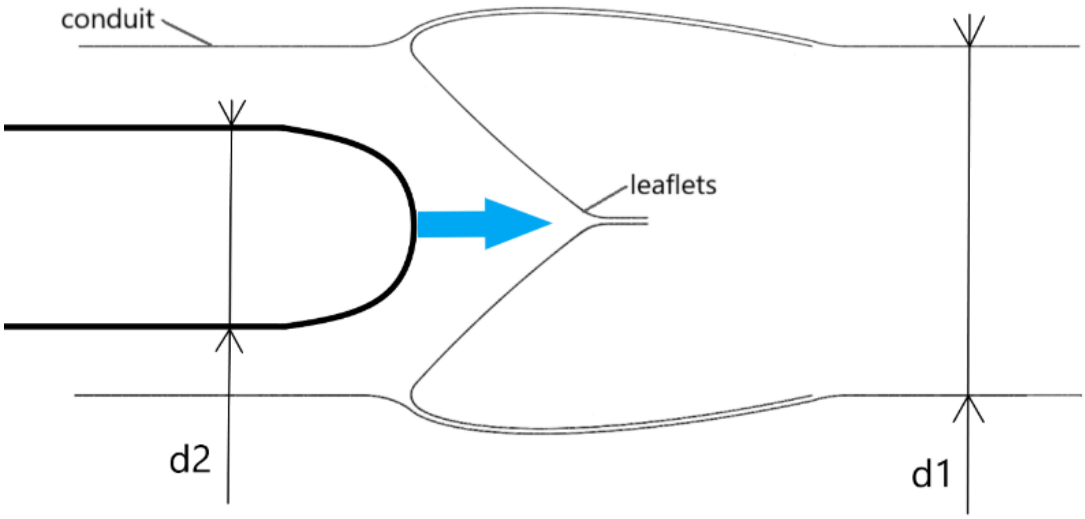

Figure 2-1: LC1, Leaflet opening behavior. d1 is the inner Conduit diameter and d2 is the Pushrod diameter. d1 = 16, 18, 20 mm and d2 = 10, 11, 12 mm respectively.

The total displacement and the displacement speed were prescribed as inputs. The output of the experimental data consisted of numerical data of the reaction force, displacement, and time. The experiments consisted of ten cycles, where one cycle is pushing and pulling (opening and closing). This was done to capture the hysteresis, Mullins softening effect and plastic-strain accumulation expected in the material. The speed of the Pushrod was 50 mm/min.

In this test, 15 samples were tested. 5 samples of each XPV size (16, 18, and 20). Each sample had a length of $80 \pm 10\ mm$ and an inner diameter corresponding to the number of the sample size (e.g., a diameter of 16 mm for the XPV16).

The material model was based on material experiments done under wet conditions. Thus, the ideal test condition for the test samples was a fully submerged wet environment. However, it was not possible to test the samples in a fully submerged wet environment. For this reason, it was decided to do experiments with wet samples in a dry environment. The samples were soaked in room-temperature water the day before the experiments.

A drawing of the test assembly for LC1, labeling all the components, and a picture of the test setup in the lab are shown in Figure 2-2. A detailed drawing of the test setup is in Appendix A, Leaflet Opening Behavior Experimental Setup. Besides the Pushrod, the Top Fixture and Bottom Fixture had a different size as well depending on the XPV size. There were three versions of the Bottom Fixture and the Top Fixture, one for each XPV size. This was to ensure all three XPV samples could be fixed.

During testing some concentric misalignment was expected between the Pushrod and the sample. For this reason, video measurements were taken to quantify the misalignment of each test. The measurement software used was Tracker (15), an open-source video analysis program. More information about the misalignment measurements is found in Appendix B, LC1 Misalignment Measurements.

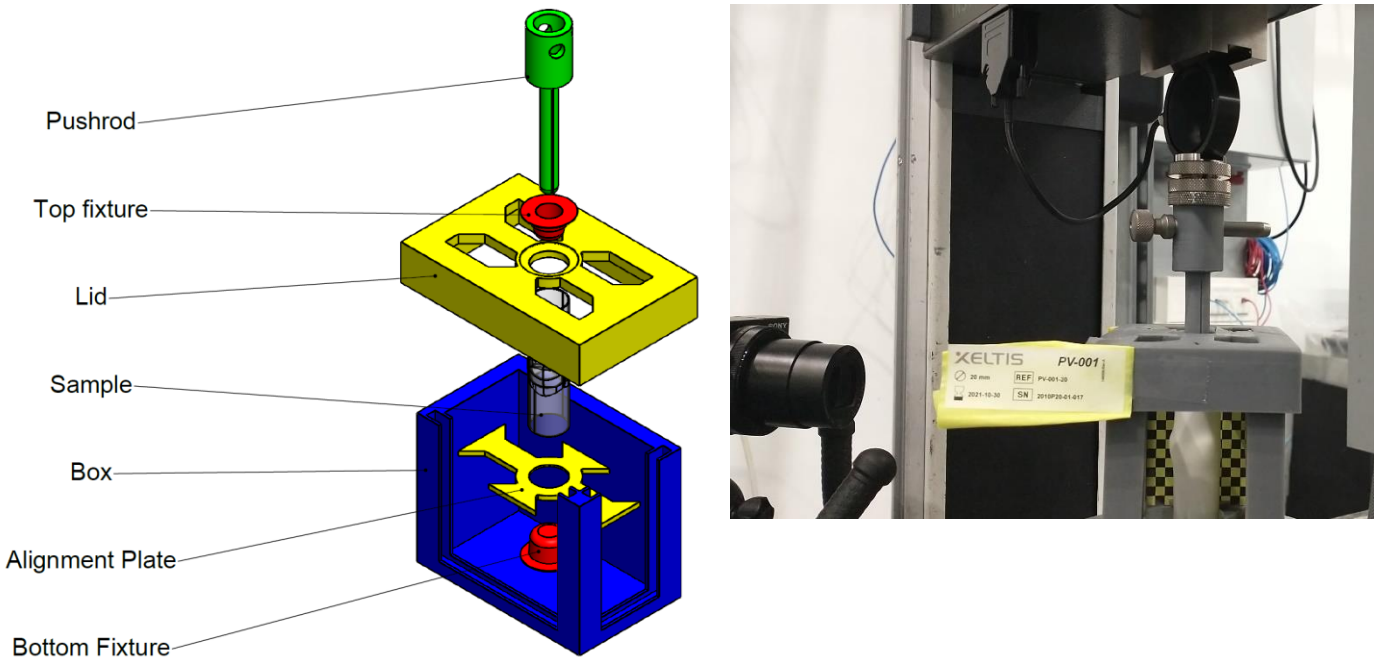

Figure 2-2: LC1, drawing test setup (left) and a picture of the test setup in the lab (right).

Besides the components shown in Figure 2-2, the following components were used during testing:

- A large circular aluminum bottom plate to which the box was attached.
- A 5N Load cell
- Two cameras attached to a tripod, to film in two perpendicular perspectives.
- Tape
- Double sided tape
- A sheet of water-absorbing material to protect the machinery in the Lloyd machine.
- Post-its, for labeling

The steps to assemble the test setup on the Lloyd machine were as follows:

1. Put a water-absorbent sheet on the bottom of the Lloyd.
2. Mount the large circular bottom plate on the bottom attachment of the Lloyd machine.
3. Apply double-sided tape on the circular bottom plate.
4. Attach the 5N load cell to the top attachment of the Lloyd machine.
5. Assemble the test setup as shown in Figure 2-2 (left) without the sample and attach the Pushrod to the load cell. Make sure the Pushrod, Bottom Fixture, and Top Fixture are of the correct size.
6. Attach the Pushrod_attachment_test1 for the XPV20 to the load cell.
7. Align the Box so that the Pushrod will not touch the Top Fixture and the cameras can film from two perspectives. Put the box on the bottom aluminium plate, where it will be fixed with double-sided tape.
8. Bring the load cell down until the tip of the Pushrod is above the bottom fixture, set this to the home position.
9. Bring the load cell up 29 mm and set the new position as the home position.
10. Place the two cameras, and make sure they are filming from two perspectives.

With the test setup assembled the testing following load protocol was applied:

1. Bring the load cell up so that the Pushrod is above the lid.
2. Take the Lid off.
3. Place a sample on the bottom fixture with the ventricle side facing up.
4. Place the lid on the test assembly, and make sure the top fixture slides into the sample.
5. Send the load cell to the home position.
6. Start filming with both cameras.
7. Start the test program, the load cell moves 29 mm down and up at a speed of 50 mm/min for 10 cycles.
8. Stop filming.
9. Bring the load cell up so that the Pushrod is above the lid.
10. Take the Lid off.
11. Remove the sample and put it in its water container.
12. Repeat from testing step 1 with the next sample, make sure to keep track of the sample serial numbers. Change the Pushrod, Bottom Fixture, and Top Fixture when changing the sample size (e.g., from an XPV16 to an XPV18).

For each experiment, the data was processed to retrieve the force-displacement curve of that experiment. One force-displacement plot of an XPV16 sample is shown in Figure 2-3. In the graph all the cycles are highlighted in green, the first half cycle of each test is shown in red. From the first half cycle, the peak force was extracted and is highlighted by a red dot in the graph. Also, from the first half cycle, the stiffness was calculated. The region of the first cycle where the stiffness was calculated is highlighted in blue in the graph. The upper and lower bounds of these regions were defined as being respectively 75% and 60% of the peak force.

Above the graph, the serial number of the sample is listed with the load case as the prefix. In this case, the prefix is PR which is short for Pushrod. The number after the second P in the number stands for the sample size, e.g., xx_xxxxP16-xx-xxx is a sample of the XPV16 and xx_xxxxP20-xx-xxx is a sample of the XPV20.

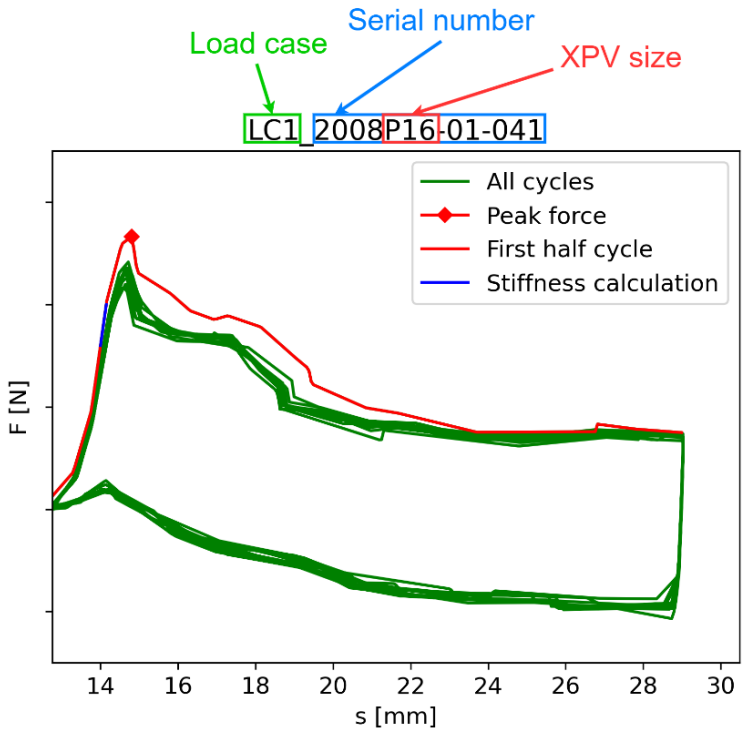

Figure 2-3: A force-displacement curve of one XPV16 sample for the Leaflet opening test. F is the force measured by the load cell in N and s is the displacement of the load cell in mm. The force-displacement curve with the numerical values is in Confidential Appendix F, LC1, Force-Displacement Curves of the Experiments.

2.1.2 LC2, Parallel Plate Compression

Taking guidance from the transverse compression load case from the ISO 5840-1 'Cardiovascular implants – Cardiac valve prostheses – General requirements' (14), transverse compression is a recommended load case to validate the structural integrity of the device. Thus, a transverse compression load case was decided to be the second experimental load case. The name of this load case is parallel plate compression (LC2).

For this load case, a sample was put between two parallel plates horizontally. The top parallel plate was attached to a load cell and moved down compressing the sample. The load case is shown in Figure 2-4. A picture of the test setup in the lab is shown in Figure 2-5.

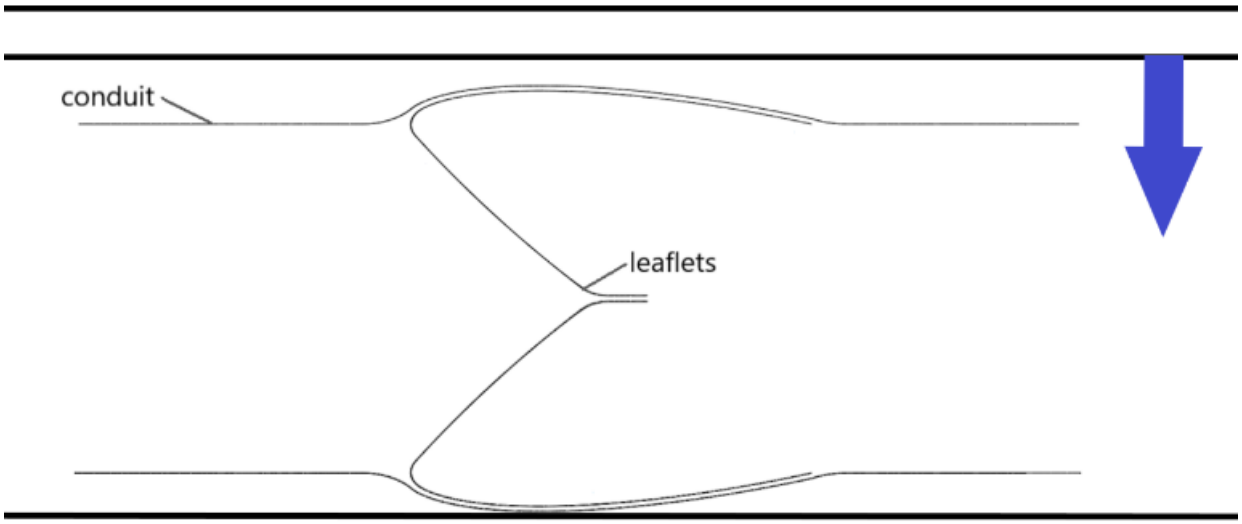

Figure 2-4: Parallel plate load case

The same load cell was used as with the Leaflet opening experiment. Thus, the same error values apply here for the load cell. These numbers are listed in Table 2-1.

The total displacement and the displacement speed were assigned as input. The output of the experimental data consisted of numerical data of the reaction force, displacement, and time. The experiments consisted of 27 cycles, one cycle was compression and release. The first three cycles were with 20% inner diameter compression, the second three cycles were with 30% inner diameter compression and the last three cycles were with 50% inner diameter compression. After the 9 cycles, the sample was rotated 120 degrees and was loaded again for 9 cycles. After this the sample was rotated again 120 degrees for the final 9 cycles, giving a total of 27 cycles. The speed of the top plate was 100 mm/min. A large number of cycles and different compressions were done to capture the hysteresis, Mullins softening effect and plastic-strain accumulation expected in the material. The amount of compression or displacement of the top parallel plate was defined from the point where the load cell measures a pre-load of 0.05 N. The top parallel plate displacement for all the sample sizes and the amount of compression are listed in Table 2-2.

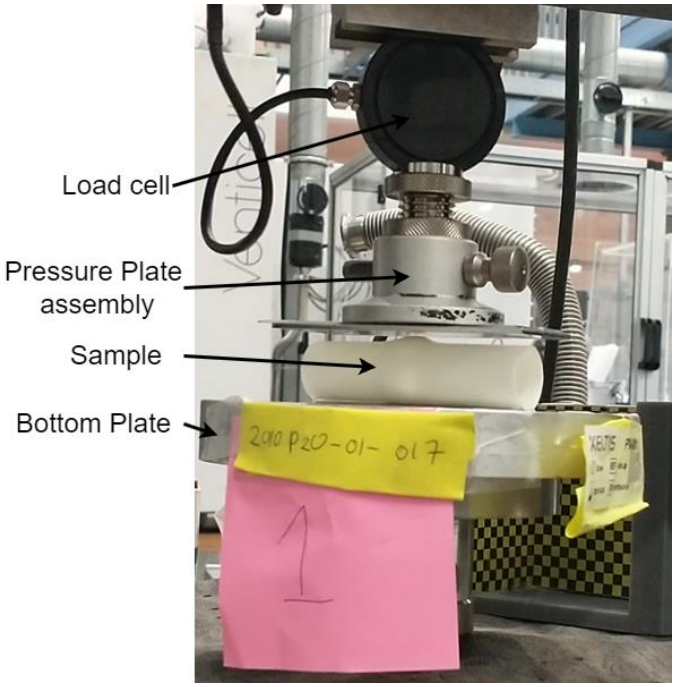

Figure 2-5: A picture of the parallel plate compression test.

The same 15 samples that were used in the experiment of LC1 were used in this experiment. Just as with the experiment of LC1, the tests were done with wet samples in dry conditions. The samples were soaked in room temperature water the day before the tests.

Table 2-2: LC2, top plate displacement for all the variants. Displacement was measured from the moment the load cell measured a force of 0.05 N.

	Compression (%)		
	20	30	50
XPV variant	Displacement (mm)		
XPV16	5	6.6	9.8
XPV18	5.4	7.2	10.8
XPV20	6.2	8.2	12.2

The following components were used during the tests:

- A Bottom Plate.
- The Pressure Plate assembly.
- A 5N Load cell
- Two cameras attached to a tripod, to film in two perpendicular perspectives.
- Tape
- Double sided tape
- A sheet of water-absorbing material to protect the machinery in the Lloyd machine.
- Post-its, for labeling

The Pressure Plate assembly was created by attaching a 2 mm thick aluminium plate to a large circular aluminium plate with double-sided tape. The assembly was pressed with a punch device in the workshop to ensure the pressure plate was fixed onto the top plate. The steps to assemble the test setup on the Lloyd machine for LC2 were as follows:

1. Put a water-absorbent sheet on the bottom of the Lloyd.
2. Mount the Bottom Plate on the bottom attachment of the Lloyd machine.
3. Attach the 5N load cell to the top attachment of the Lloyd machine.
4. Attach the Pressure Plate assembly to the load cell.
5. Place an XPV20 sample on the Bottom Plate.
6. Move the load cell down until the Pressure Plate is close to the XPV20 sample, set this as the home position.
7. Remove the XPV20 sample.
8. Place the two cameras, and make sure they are filming from two perspectives.

The test setup is shown in Figure 2-5. With the test setup assembled the testing following load protocol was applied:

1. Make sure the Lloyd machine is in its home position.
2. Place a conditioned sample on the bottom plate with the ventricle side facing one of the cameras.
3. Take the Lid off.
4. Start filming with both cameras.
5. Start the test program, the load cell down compressing the sample 20%, 30%, and 50% respectively for three cycles each. The distances are defined in Table 2-2.
6. Stop filming.
7. Remove the sample and put it in its water container.
8. Repeat from testing step 1 with the next sample, make sure to keep track of the sample serial numbers.

For each experiment, the data was processed to retrieve the force-displacement curve in the same way as LC1. One force-displacement plot of an XPV16 sample is shown in Figure 2-6. All the cycles are highlighted in green and the first half cycle of each test is shown in red. From the first half cycle, the force at the displacement value of 3 mm (F_p) was extracted and is highlighted by a blue dot in the graphs. From the first half cycle, the stiffness was also calculated. The region of the first cycle where the stiffness was calculated is highlighted with a blue line in the graph. The upper and lower bounds of these regions are defined as being respectively 0.5 N above F_p and 0.5 N below F_p.

Above the graph, the serial number of the sample is listed with the load case as the prefix. In this case, the prefix is PP which is short for Parallel Plate. The number after the second P in the number stands for the sample size, e.g., xx_xxxxP16-xx-xxx is a sample of the XPV16 and xx_xxxxP20-xx-xxx is a sample of the XPV20. The last number indicated the position of the sample. Number 1 indicates the first position; number 2 indicates the second position where the sample was 120 degrees turned axially from the first position. Finally, number 3 indicates the last position where the sample was 240 degrees turned axially from the first position. This is shown in Figure 2-6.

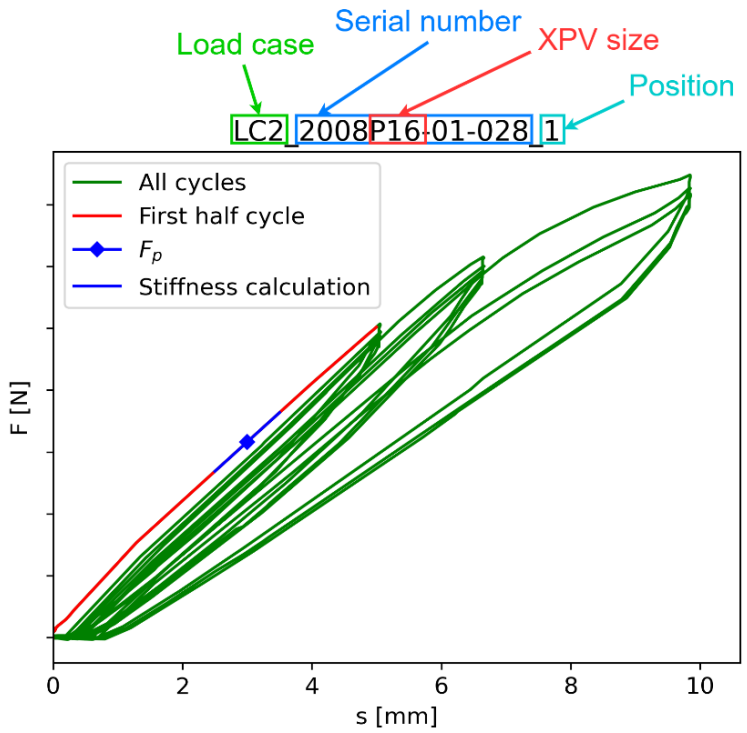

Figure 2-6: A force-displacement curve of one XPV16 sample for the parallel plate compression test. F is the force measured by the load cell in N and s is the displacement of the load cell in mm. The force-displacement curve with the numerical values is in Confidential Appendix G, LC2, Force-Displacement Curves of the Experiments.

2.2 MODEL GEOMETRY

The XPV comprises the following components: a Conduit and three Leaflets forming the valve. The model was developed in three sizes, XPV16, XPV18, and XPV20 where the number corresponds to the inner diameter of the Conduit. Figure 2-7 shows an XPV20 FE model. Further components were added to the XPV assembly for the two load cases considered. To account for different types of uncertainties the model was developed parametric. This was done using Abaqus CAE together with Python scripts (16). The Abaqus CAE files and Python scripts are stored at 4RealSim™.

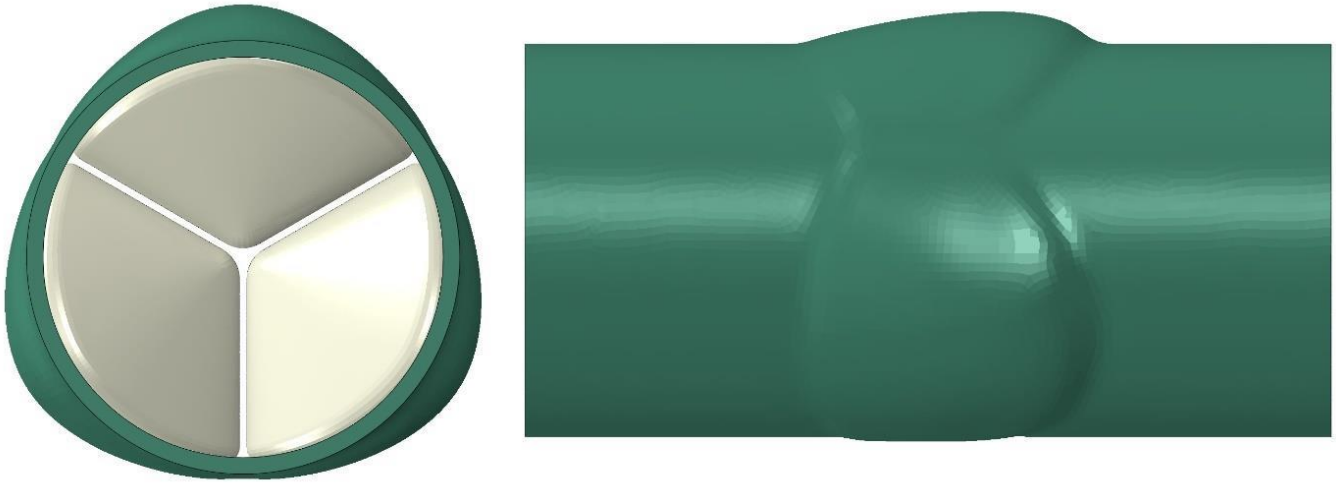

Figure 2-7: XPV20 FE model

2.2.1 CONDUIT

The design of the Conduit was provided as a CAD drawing by Xeltis™ and is shown in Figure 2-8. Due to the additive nature of the device manufacturing, the geometry of the Conduit is dependent on the geometry and positioning of the Leaflets. In the geometry cut-outs have been created where the Leaflets are situated, these cut-outs are in the middle of the Conduit.

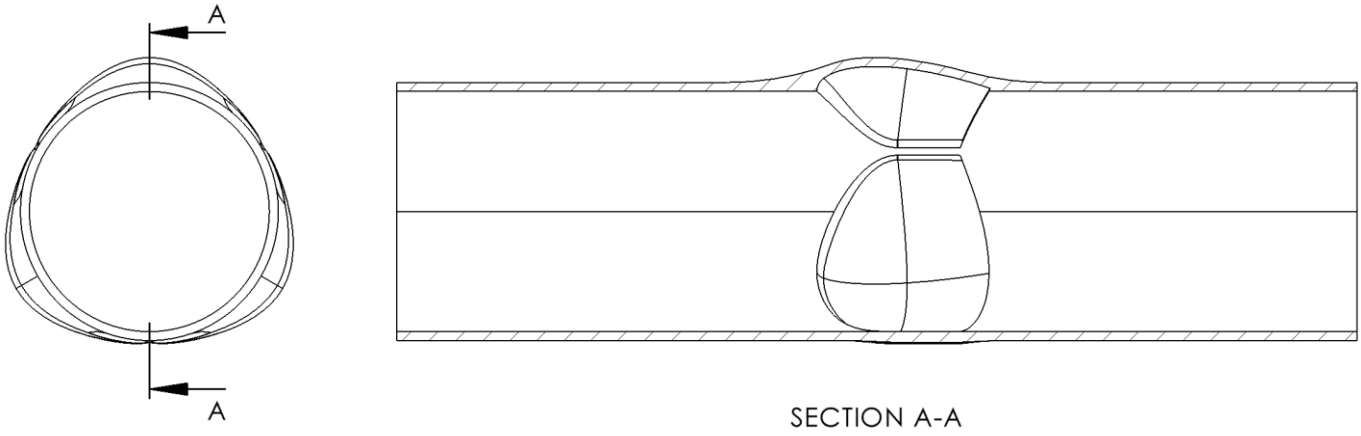

Figure 2-8: Conduit CAD geometry

The electrospinning manufacturing method creates the Conduit on a mold and the CAD geometry of the Conduit was extracted from CAD files of these molds. Thus, the Conduit CAD geometry was different from the real Conduit geometry. Because of the manufacturing method, there is a non-uniform thickness across the length of the Conduit. During manufacturing, the needle where the polymer is dispensed from moves back-and-forth axially in relation to the collector (see Figure 1-2). This back-and-forth motion causes the thickness to be thicker in the middle of the collector than at the edges. Furthermore, when the device is placed inside a patient the Conduit is trimmed in length and at an angle to make the device fit. Thus, the length, thickness distribution, and geometry of the cut-outs deviate from the CAD files provided. A µCT scan of part of the real device geometry is shown in Figure 2-9.

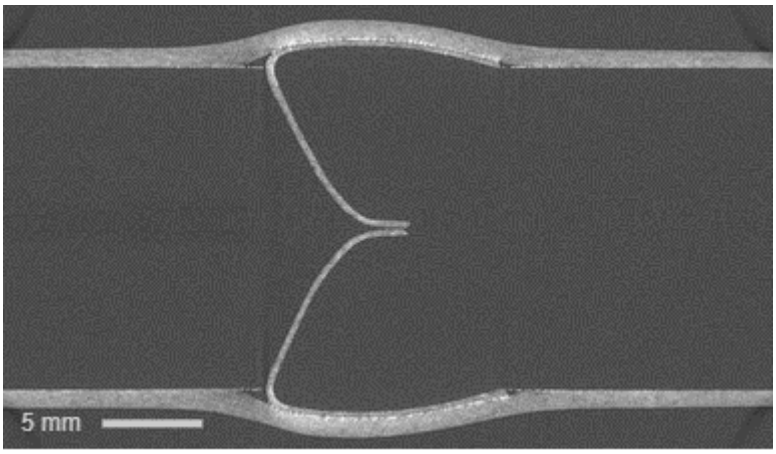

Figure 2-9: µCT scan of the Conduit with two Leaflets shown.

To account for these uncertainties, parameters were defined for the length, trimming angle, distance from the ventricle side to the sinus, and thickness distribution of the Conduit as shown in Figure 2-11. A description of the geometry parameters for the Conduit is listed in Table 2-3. The inside diameter of the device was assumed fixed and had the same diameter as the mold (e.g., 20 mm for XPV20). The numerical values of these parameters are in Confidential Appendix A, Conduit Geometry Parameter Values.

Table 2-3: Conduit geometry parameters, numerical values are in Confidential Appendix A, Conduit Geometry Parameter Values.

Parameter	Unit	Description
L	mm	Conduit Length
D	mm	Inner Diameter
VS	mm	Ventricle side to Sinus
TA_V	deg	Trim Angle ventricle side
TA_P	deg	Trim Angle pulmonary side
TPA_V	deg	Trim Plane Angle ventricle side
TPA_P	deg	Trim Plane angle pulmonary side
t1, t2, t3, t4, t5	mm	Conduit thickness at five points

Values for the parameters were obtained by measurements done on µCT data performed by 4RealSim™. The length of the Conduit and distance from the ventricle side to the sinus were measured using a caliper.

To obtain the accurate geometry of the Leaflet cut-outs an ad-hoc forming model was developed. In this forming simulation, the Conduit was modeled as a cylinder, and three rigid Leaflets were pushed into the Conduit (see Figure 2-10).

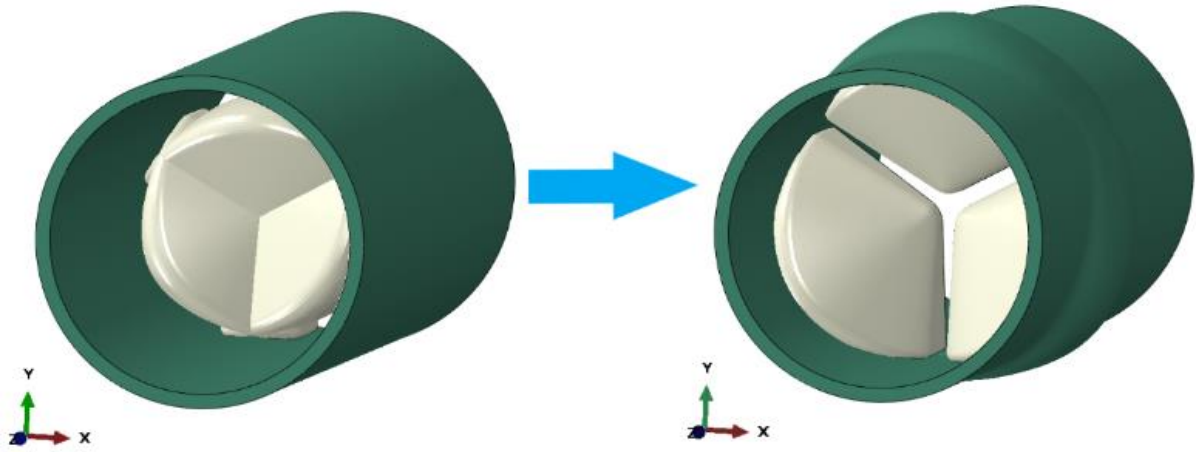

Figure 2-10: Conduit forming.

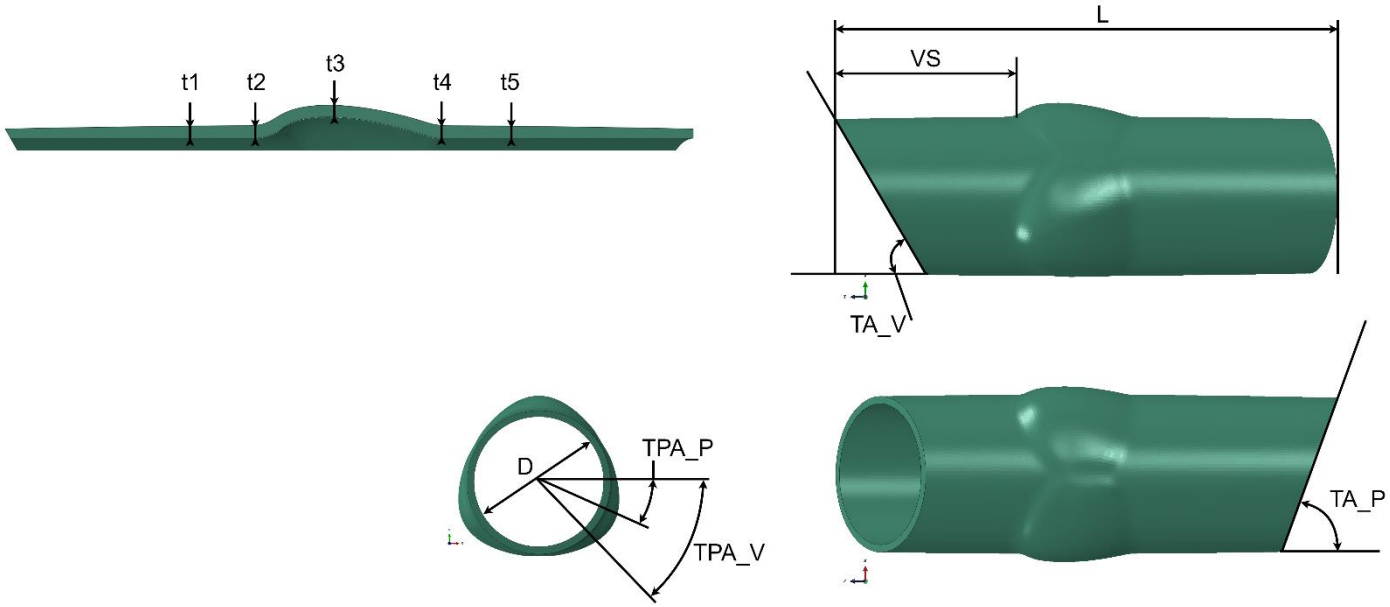

Figure 2-11: Conduit geometry parameters visualization

The Conduit consisted of a mesh with solid linear elements with reduced integration (C3D8R) with a mesh resolution of 0.4 mm with 2 elements through the thickness. Enhanced hourglassing was used to reduce the hourglassing of the elements. This was based on a mesh convergence study done by 4RealSim™. In this convergence study the element size, number of elements through the thickness, and element type were investigated. The mesh convergence study consisted of a simplified parallel plate compression test. Here a portion of the conduit was modeled as shown in Figure 2-12. The maximum logarithmic strain in the circumferential direction was used to compare the different mesh definitions. The comparison was done by comparing the mesh definitions to a converged second-order mesh definition (C3D20) which was the most accurate at a greater computational cost. Considering the maximum logarithmic strain in the circumferential direction and computational cost, element C3D8R was chosen with a mesh resolution of 0.4 mm and two elements through the thickness. This resulted in a total of 61584, 69488, and 76220 elements in the Conduit for the XPV16, XPV18, and XPV20 respectively with mean parameter values.

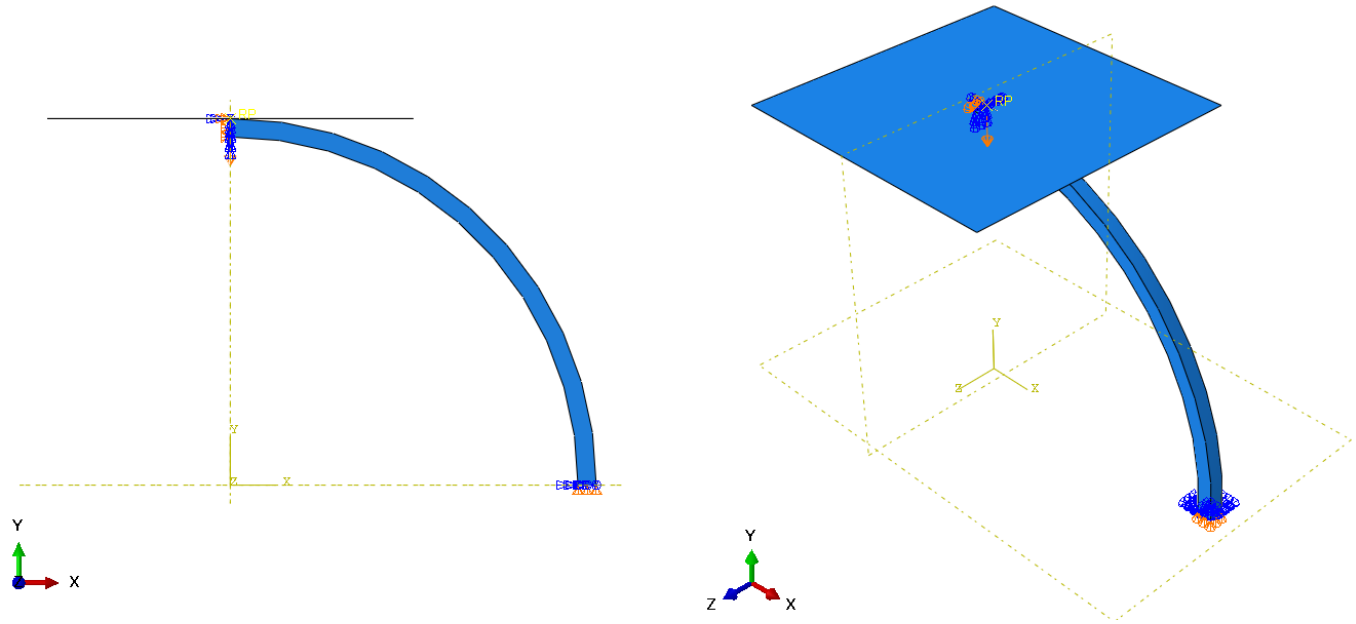

Figure 2-12: Conduit mesh convergence model

Multiple partitions were made in the Conduit to improve the quality of the mesh as is shown in Figure 2-13. The mesh was generated with a sweep path to increase uniformity across the thickness (16). The sweep path was from the inside to the outside. The mesh of the formed Conduit is shown in Figure 2-14.

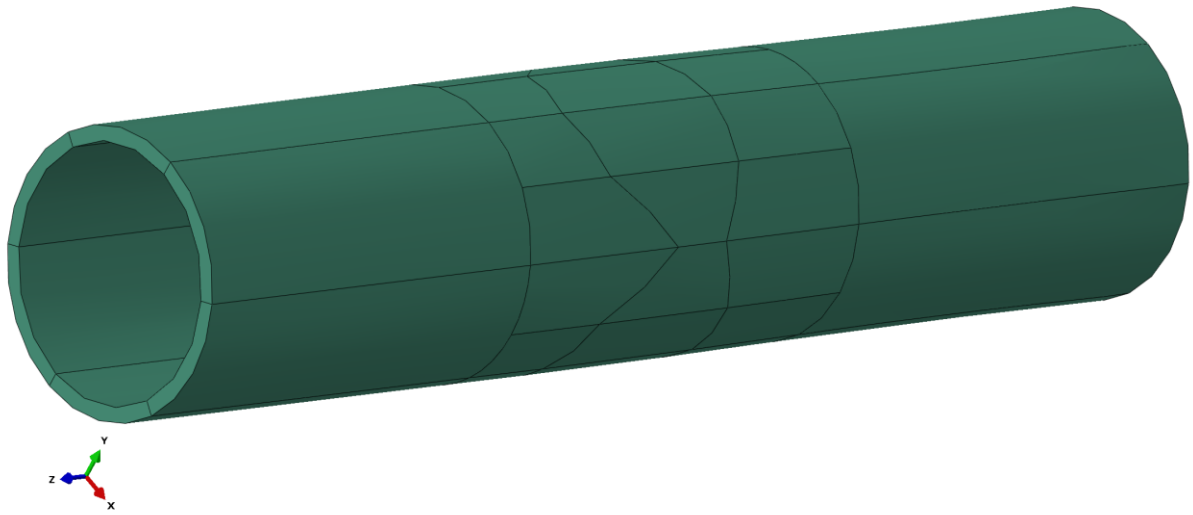

Figure 2-13: Partitions made in the Conduit to improve the mesh quality.

Figure 2-14: Formed Conduit mesh.

2.2.2 LEAFLETS

As with the design of the Conduit, the design of the Leaflets was provided as CAD files from Xeltis™. The CAD geometry of these Leaflets is shown in Figure 2-15. The thickness distribution in the CAD file was uniform. As with the Conduit, the geometry of the Leaflet CAD geometry was extracted from CAD files of the molds. Thus, it deviated from the actual geometry of the Leaflets. Because of the manufacturing method, there is a non-uniform thickness across the Leaflet. During manufacturing, the needle where the polymer is dispensed from moves back-and-forth axially in relation to the collector (see Figure 1-2). This back-and-forth motion causes the thickness to be thicker in the middle of the collector than at the edges. After the electrospinning process, the Leaflets are trimmed to the right angle and length. A µCT scan of the device in Figure 2-16 shows the real geometry of the Leaflets. In the FE model, the CAD geometry was imported and modified to resemble the shape of the Leaflets after manufacturing. This was done by removing faces until only the inner surface of the Leaflet was left. Afterwards, the Leaflet trimming was incorporated into the geometry of the Leaflets by defining parameters for the Leaflet trim length and Leaflet trim angle as shown in Figure 2-16. An explanation of the Leaflet trimming parameters is listed in Table 2-4.

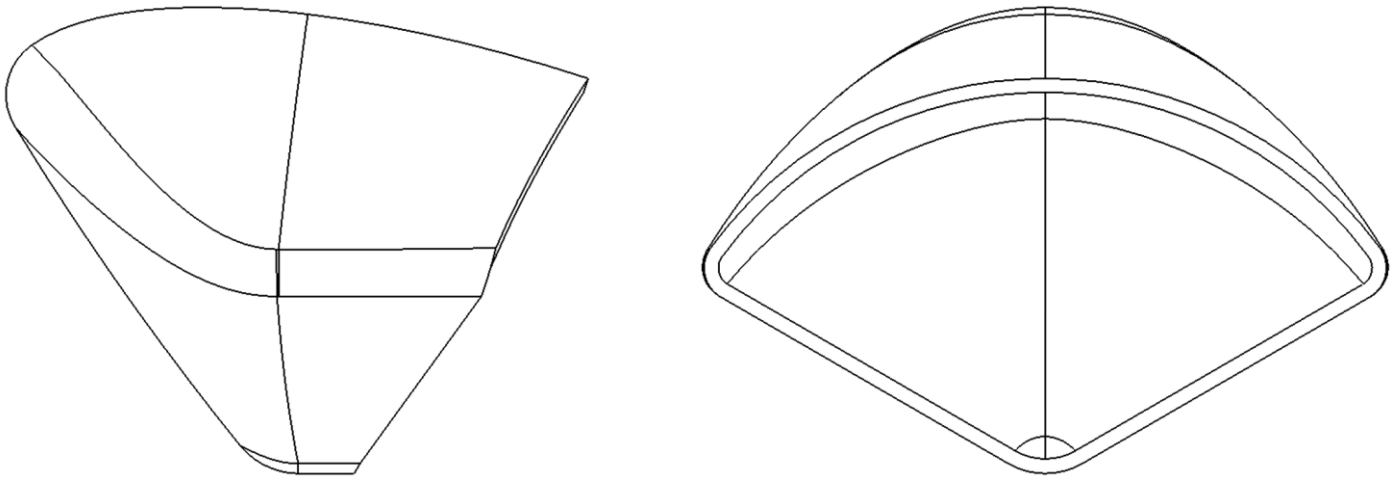

Figure 2-15: Provided Leaflet CAD geometry.

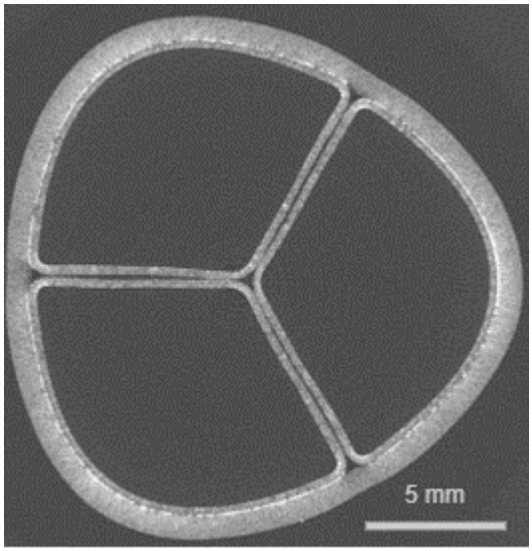

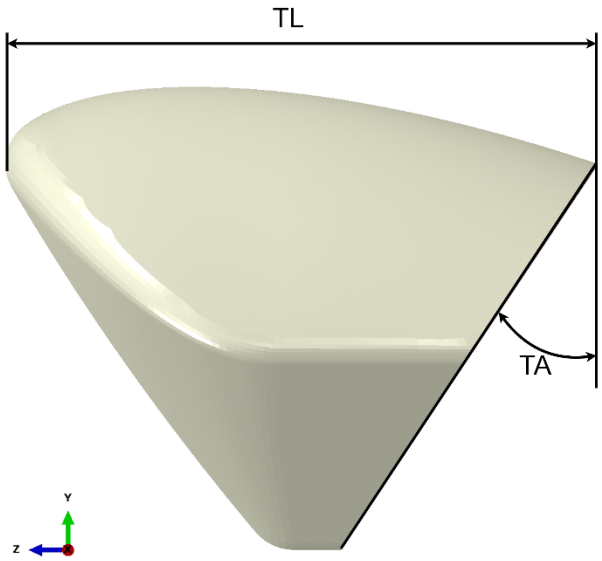

Figure 2-16: µCT scan of the real XPV showing three Leaflets with the Conduit (right) and Leaflet trimming visualization (right).

Table 2-4: Leaflet trimming parameters description, numerical values are in Confidential Appendix B, Leaflet Geometry Parameter Values.

Parameter	Unit	Description
TL	mm	Trim length
TA	deg	Trim angle

Furthermore, the non-uniform thickness of the Leaflets was included in the model with a discrete field. Here every node was assigned a thickness. This thickness distribution was divided into regions of the Leaflet, shown in Figure 2-17. There were two types of regions, the main regions, and the transition regions. The main regions consisted of the Top, Belly, and Side. The transition regions consisted of bt_transition (bt is belly and top), sb_transition (sb is side and belly), st_transition (st is side and top), and sbt_transition (sbt is side belly and top). These parameters were defined for the individual Leaflets. This way, differences between the Leaflets were included in the model. The thickness of every node in the main regions was defined with a second-order regression function, shown in Formula 2.1. The regression function calculates the thickness of the specific node by six parameters and the y-z location of the node. An explanation of the parameters used in the formula is in Table 2-5. Values for the parameters regarding the Leaflet trimming and the non-uniform thickness distribution were obtained by measurements done on µCT data performed by 4RealSim™. These values are in Confidential Appendix B, Leaflet Geometry Parameter Values.

$$T_{node} = \begin{pmatrix} \beta_0 + \beta_1 y + \beta_2 z + \beta_{11} y^2 \\ +\beta_{22} z^2 + \beta_{12} yz \end{pmatrix} \quad (2.1)$$

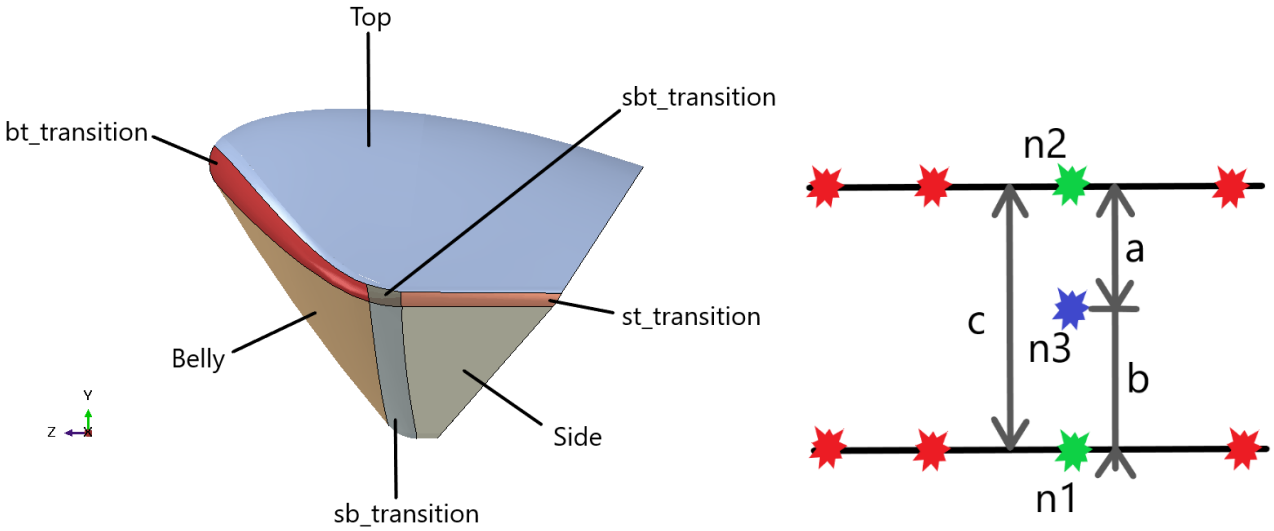

Figure 2-17: Leaflet thickness distribution regions (left) and thickness calculation of a node in a transition region (right).

Table 2-5: Thickness distribution of the main regions formula parameters, numerical values are in Confidential Appendix B, Leaflet Geometry Parameter Values.

Parameter	Unit	Description
T_{node}	mm	Thickness of the node
β_0, β_1, β_2, $\beta_{11}, \beta_{22}, \beta_{12}$	mm - 1/mm	Six different thickness parameters,
y, z	mm	The y -and z-coordinates of the node

The thickness in the transition regions is dependent on the thickness of the main regions. The thickness of the transition regions was calculated by taking the thickness of the two nodes on the edge of the adjacent main regions and scaling the thickness with the distance between the nodes as done in Formula 2.2. An explanation of the parameters used in the formula is in Table 2-6 and the calculation is schematically shown in Figure 2-17.

$$t_{n3} = b * \frac{t_{n1} - t_{n2}}{c} + t_{n1} \quad (2.2)$$

Table 2-6: Thickness distribution of the transition regions formula parameters

Parameter	Unit	Description
t_{n1}	mm	The thickness of the node lying on the edge of the first main region.
t_{n2}	mm	The thickness of the node lying on the edge of the second main region.
t_{n3}	mm	The thickness of the node lying in the transition region.
b	-	Distance between the node in the first main region and the node in the transition region.
c	-	Distance between the nodes on the first and second main region

The Leaflets were meshed with solid linear elements with reduced integration (C3D8R). The mesh resolution was 0.2 mm with 3 elements through the thickness. Enhanced hourglassing was used to reduce the hourglassing of the elements. This was based on a mesh convergence study done by 4RealSim™. In this convergence study the element size, number of elements through the thickness, and element type were investigated. Here a 1/6th symmetry model of the XPV was used as shown in Figure 2-18. Two load cases were considered, a Leaflet opening load case and a Leaflet closing load case. For both load cases, the maximum logarithmic strain in the circumferential direction and the axial direction were compared in a region of interest (ROI) specific to the load case considered, as shown in Figure 2-19. The comparison was done by comparing the mesh definitions to a converged second-order mesh definition (C3D20) which was the most accurate at a greater computational cost. From this study element C3D8R was chosen with a mesh resolution of 0.2 mm and three elements through the thickness. This was chosen by comparing the maximum logarithmic strain in the circumferential direction and the axial direction, and the computational costs. This resulted in a total of 26022, 36234, and 44115 elements in the Leaflet for the XPV16, XPV18, and XPV20 respectively with mean parameter values.

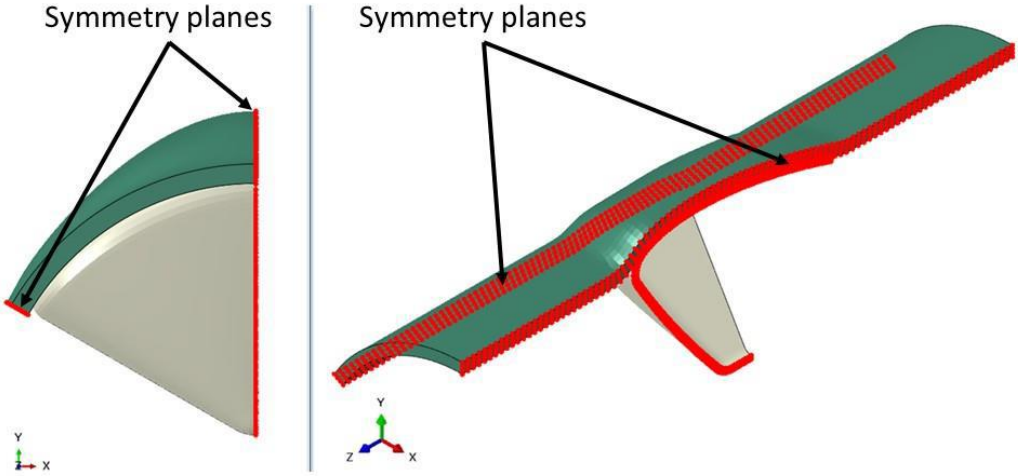

Figure 2-18: Leaflet mesh convergence model

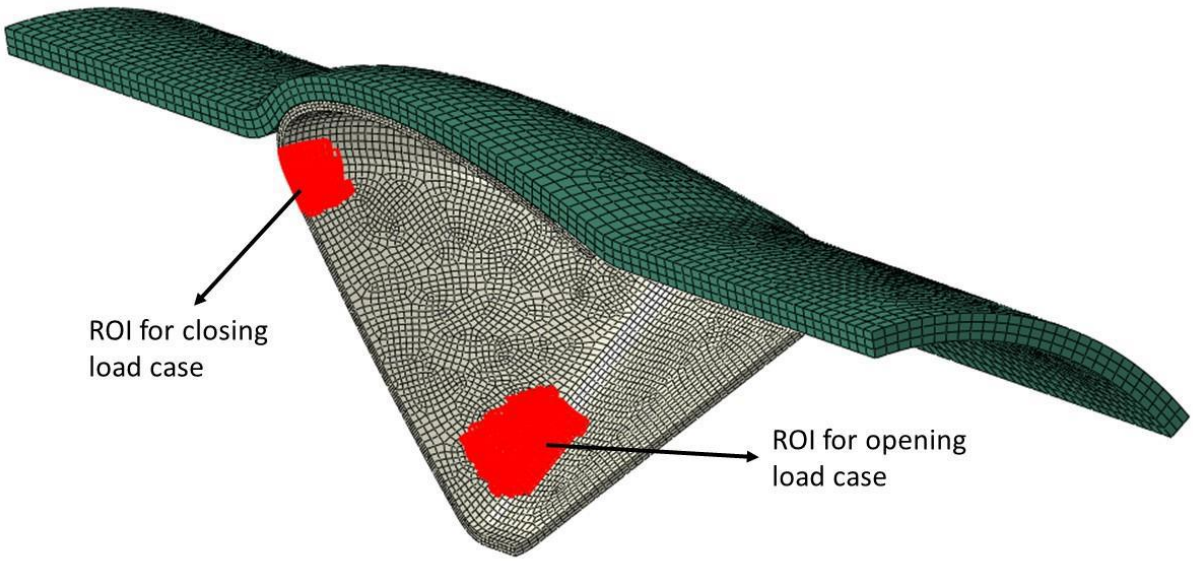

Figure 2-19: ROIs for the two Leaflet mesh convergence study load cases

The first step in generating the Leaflet mesh was to create a shell mesh. The second step was to create a solid mesh by offsetting the shell mesh to the outside direction. The shell mesh was defined as a combination of a free-form mesh and a sweep mesh to improve the mesh quality. Furthermore, multiple partitions were defined to the geometry to improve the mesh quality (16). The partitions, regions with free mesh, and sweep mesh are shown in Figure 2-20. The resulting Leaflet mesh is shown in Figure 2-21.

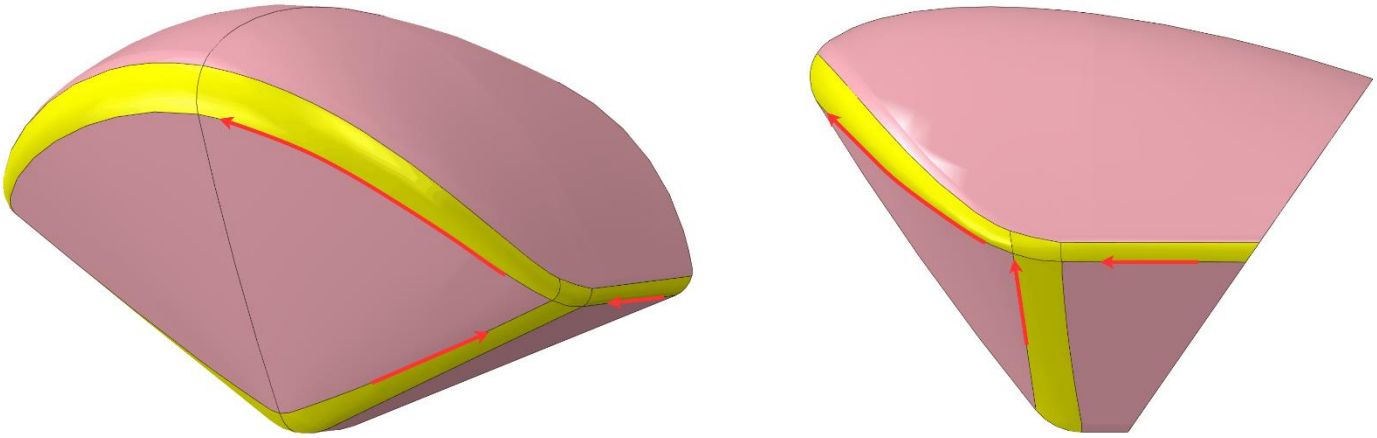

Figure 2-20: Leaflet mesh definitions. In pink, a free-form mesh is defined. In yellow, a sweep mesh is defined. The sweep path is shown with red arrows.

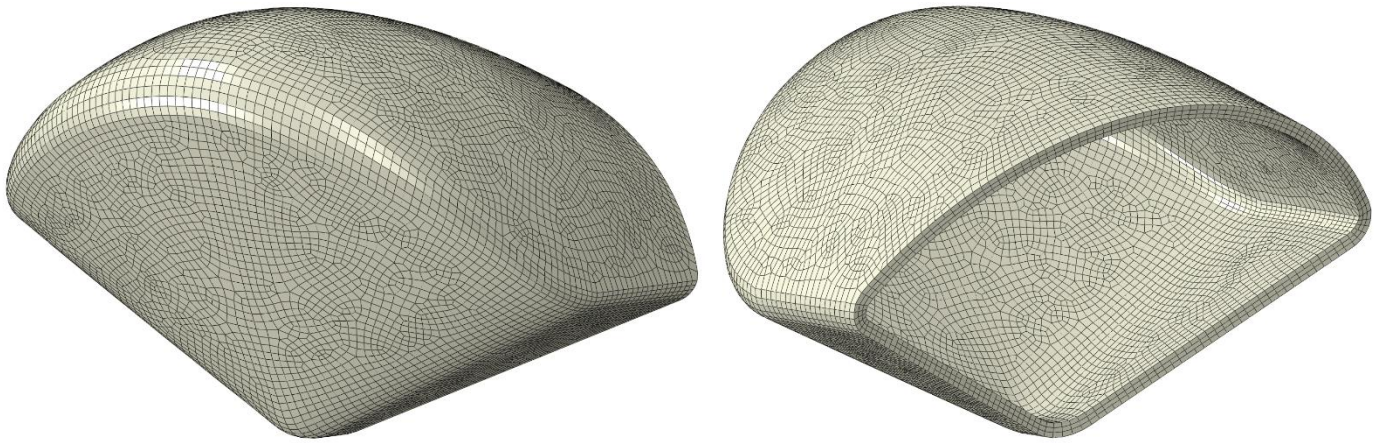

Figure 2-21: Leaflet mesh

2.2.3 XPV ASSEMBLY

Putting the three individual Leaflets and the Conduit together gives the XPV assembly. In the assembly, the position of the Leaflets to the Conduit was defined with parameters as shown in Figure 2-22 and explained in Table 2-7. These parameters were defined for the three Leaflets individually and the numerical values are in Confidential Appendix B, Leaflet Geometry Parameter Values.

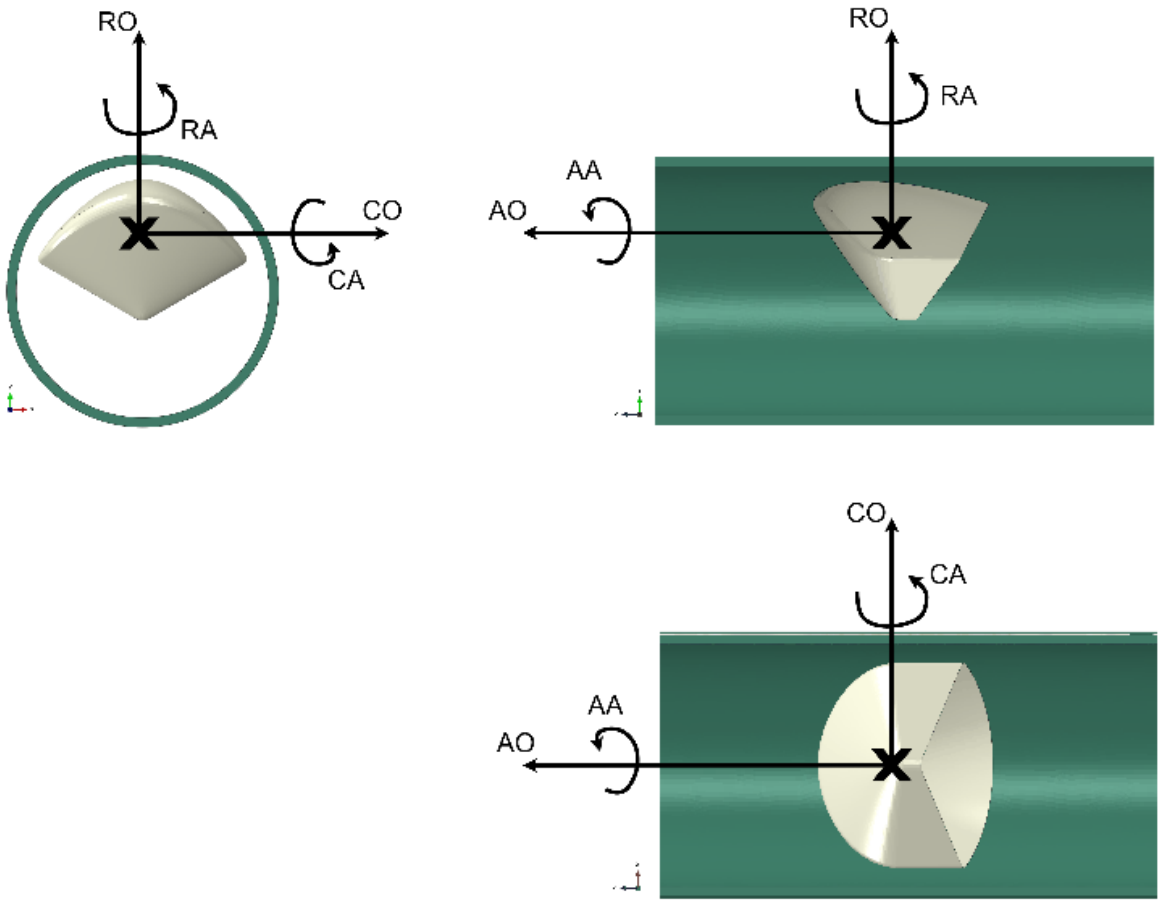

Figure 2-22: Leaflet position parameters about the Conduit, the Conduit is in its unformed state.

Table 2-7: Leaflet assembly position parameters

Parameter	Unit	Description
RO	mm	Radial Offset
CO	mm	Center Offset
AO	mm	Axial Offset
RA	deg	Radial Angle
CA	deg	Center Angle
AA	deg	Axial Angle

2.2.4 Conduit Forming Assembly

For the Conduit forming simulation (FS), additional geometry was added to the XPV assembly. Besides the Conduit and Leaflets, an analytical rigid cylinder was added to the assembly. The inside of the Conduit was in contact with the outside of the rigid cylinder and was used to keep the Conduit in place during the forming simulation. In Figure 2-23 the forming model assembly is shown.

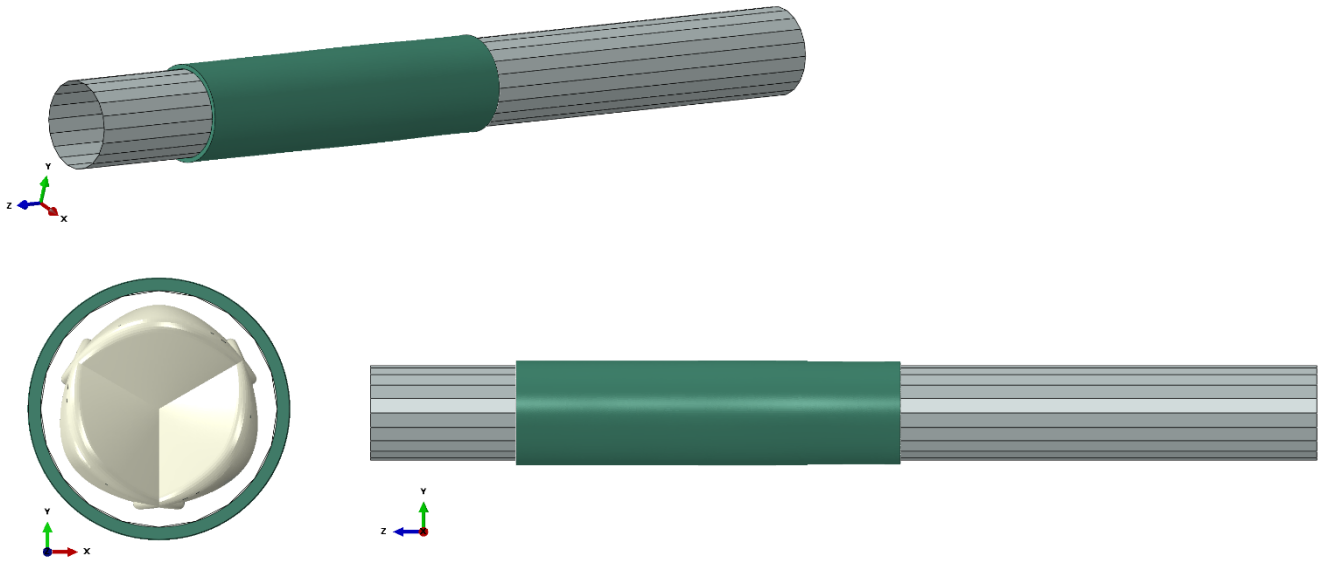

Figure 2-23: Forming model assembly isometric (top), front view (bottom-left), side view (bottom-right)

2.2.5 LC1, Leaflet Opening Behavior Assembly

The formed Conduit and the Leaflets from the FS are imported without stress into the Leaflet opening behavior assembly. Furthermore, to simulate the first load case the XPV assembly was modified to a half-symmetry model, this was done to improve computational time while still allowing for the misalignment of the Pushrod to be incorporated in the model. Because of symmetry, an analytical rigid symmetry plane was added to the model for the contact definitions. Furthermore, the Pushrod was added to the assembly. The Pushrod was modeled as an analytical rigid part. Adding all the parts to the XPV assembly gives the Leaflet opening behavior assembly and is shown in Figure 2-24.

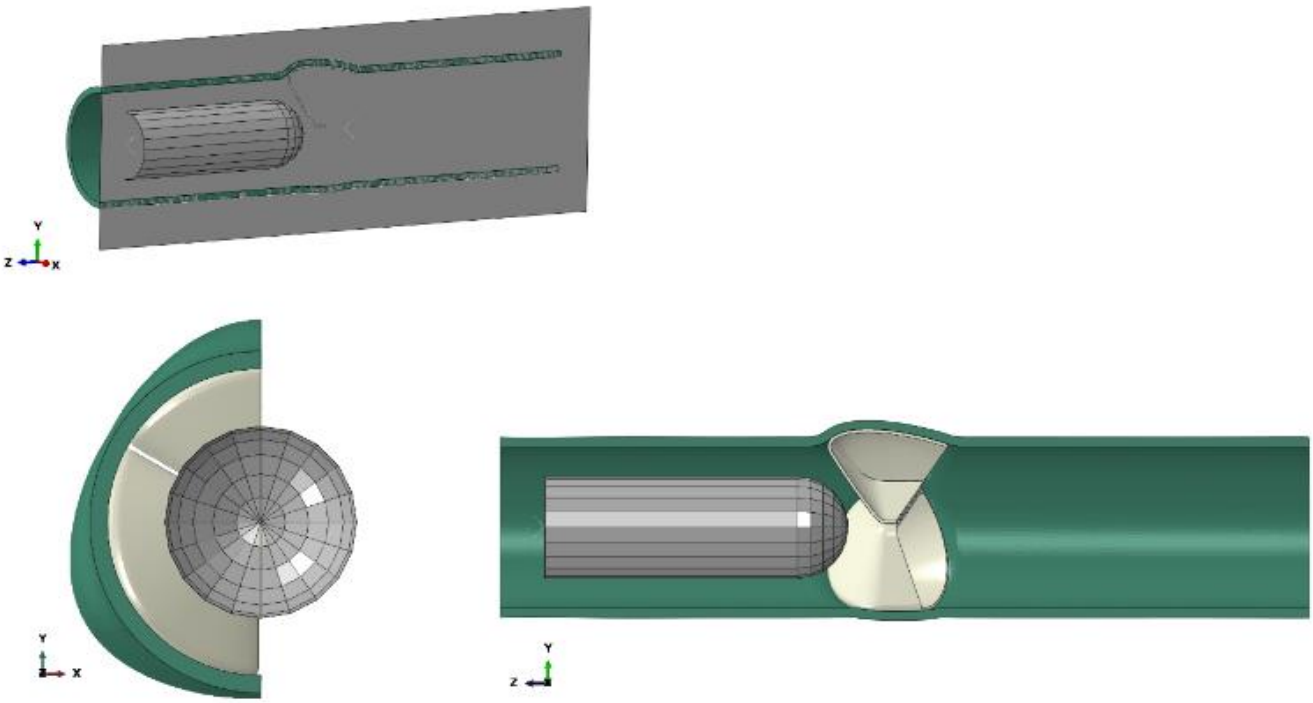

Figure 2-24: Leaflet opening behavior assembly isometric (top), front view (bottom-left), side view without symmetry plane (bottom-right)

Only the part of the Pushrod that interacts (collides) with the XPV was modeled. Two misalignment parameters were added to the model. One parameter was defined to quantify the radial misalignment and one parameter was defined to quantify the angular misalignment of the Pushrod to the Conduit. The angular misalignment was defined from the point where the Pushrod was attached to the load cell. This was the expected location where the Pushrod misalignment would occur. This point was placed at 107 mm from the tip of the Pushrod in the positive z-direction as shown in Figure 2-25. Thus, the misalignment was an offset in the y-direction and an angle around the x-axis in Figure 2-25.

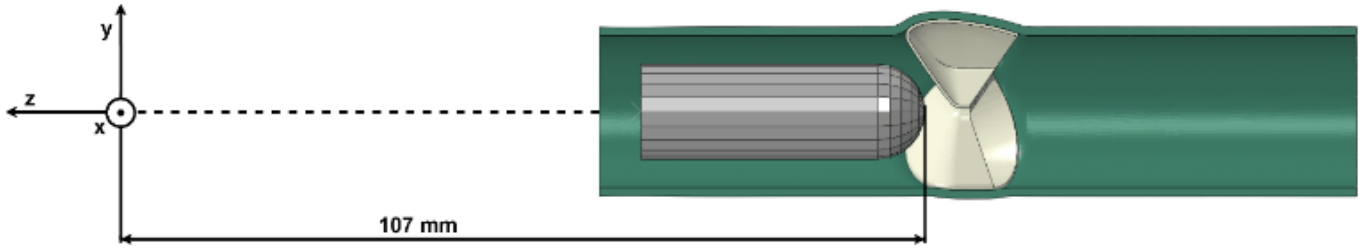

Figure 2-25: Pushrod misalignment. Misalignment is defined as an offset in the y-direction and a rotation around the x-axis.

2.2.6 LC2, Parallel Plate Compression Assembly

The formed Conduit and the Leaflets from the FS are imported without stress into the Leaflet opening behavior assembly. Furthermore, to simulate the parallel plate compression load case, the XPV assembly was modified to a half-symmetry model in the same way as the Leaflet opening behavior assembly, this was done to improve computational time. Because of symmetry, an analytical rigid symmetry plane was added to the model for the contact definitions. Furthermore, two additional analytical rigid planes were used to simulate the pressure plates used in the experiments. Putting all the components together gives the parallel plate compression assembly, which is shown in Figure 2-26.

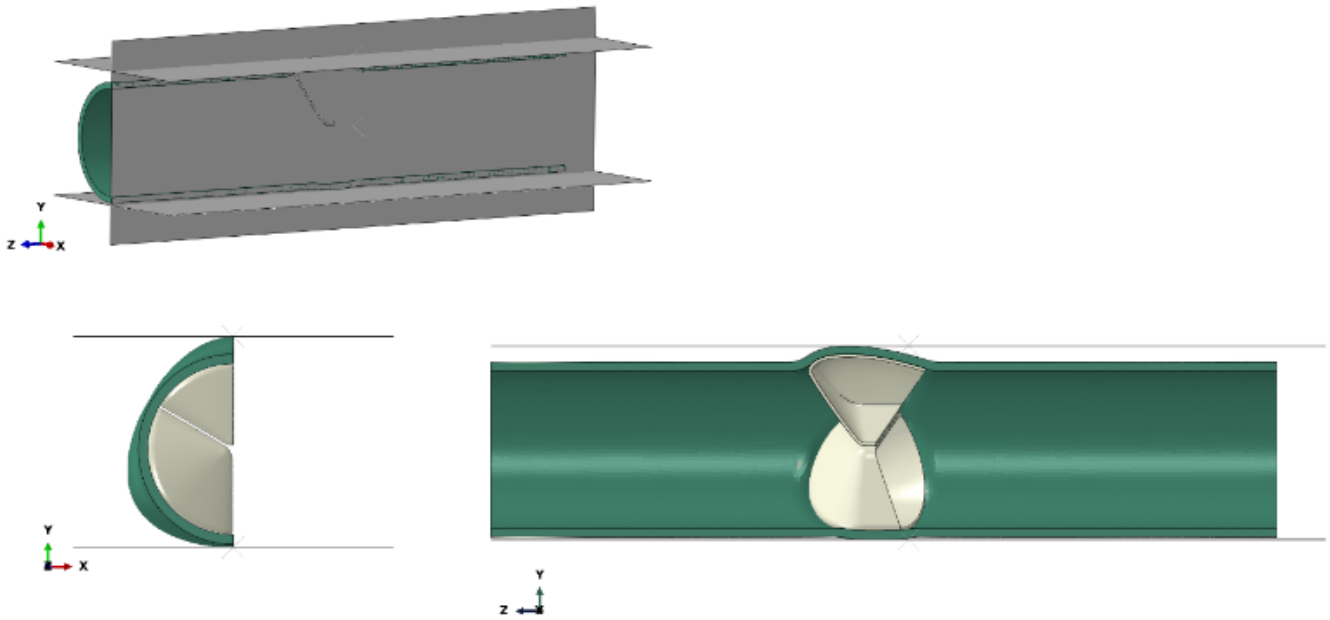

Figure 2-26: Parallel plate compression assembly isometric (top), front view (bottom-left), side view without symmetry plane (bottom-right)

2.3 MATERIAL MODEL

2.3.1 XPV MATERIAL MODEL

To describe the material behavior a user-defined material model was developed for both the Conduit (XP-005) and the Leaflet (XP-034) material. The material behavior was described through a material model containing characteristics for anisotropic, hyperelastic, and viscoelastic behavior with plastic deformation, also including cyclic stress softening (Mullins effect). Temperature dependency was ignored as the body temperature was assumed to be constant. The material behavior was taken at 37 degrees Celsius. Furthermore, the material was calibrated with three different types of experiments. These include cyclic biaxial tensile tests, multiple uniaxial tensile tests, and multiple uniaxial stress relaxation tests after cyclic loading.

The tests have been done in two directions for both materials. The two directions were defined as the circumferential direction and the axial direction of the cylinder used during the electrospinning process. The material experiments were done by Leartiker™ (17). The material calibration and material model development were done by TU-Graz (18, 19). The material model with its parameters from TU-Graz was directly imported into the computational model. The formulas from the material model together with their parameters are in Appendix D, Material Parameters Description. Numerical values of the material parameters are in Confidential Appendix C, Material Model Values.

To understand the material model, a cyclic tensile test simulation has been performed with a single 1 by 1 mm element. The cyclic load case consisted of 5 cycles of 1.05 stretch level followed by 5 cycles of 1.1, 1.2, 1.3, and 1.5 stretch levels. Here, one cycle consisted of loading to the stretch level and unloading to the starting length of the material. Furthermore, the load speed was 10 mm/min. From the simulation, the Cauchy stress and logarithmic strain were extracted to get the stress-strain curve of each load case. Both materials, XP-034 and XP-005, have been tested in the axial and circumferential direction. The obtained stress-strain curves are shown in Figure 2-27. The graphs with the numerical values are in Confidential Appendix C, Material Model Values. From the stress-strain curves, it can be observed that both materials are stiffer in the axial direction than in the circumferential direction, indicating anisotropy. Furthermore, the hysteresis due to the viscoelasticity of the material is visible by the difference in the loading and unloading curve (20). Also, the Mullins softening effect is visible, as the reloading curve follows approximately the unloading curve for each cycle (21). The unloading curve doesn't follow the unloading curve exactly because of plastic deformation. Furthermore, the stress at zero strain goes further below zero with each cycle, indicating plastic deformation.

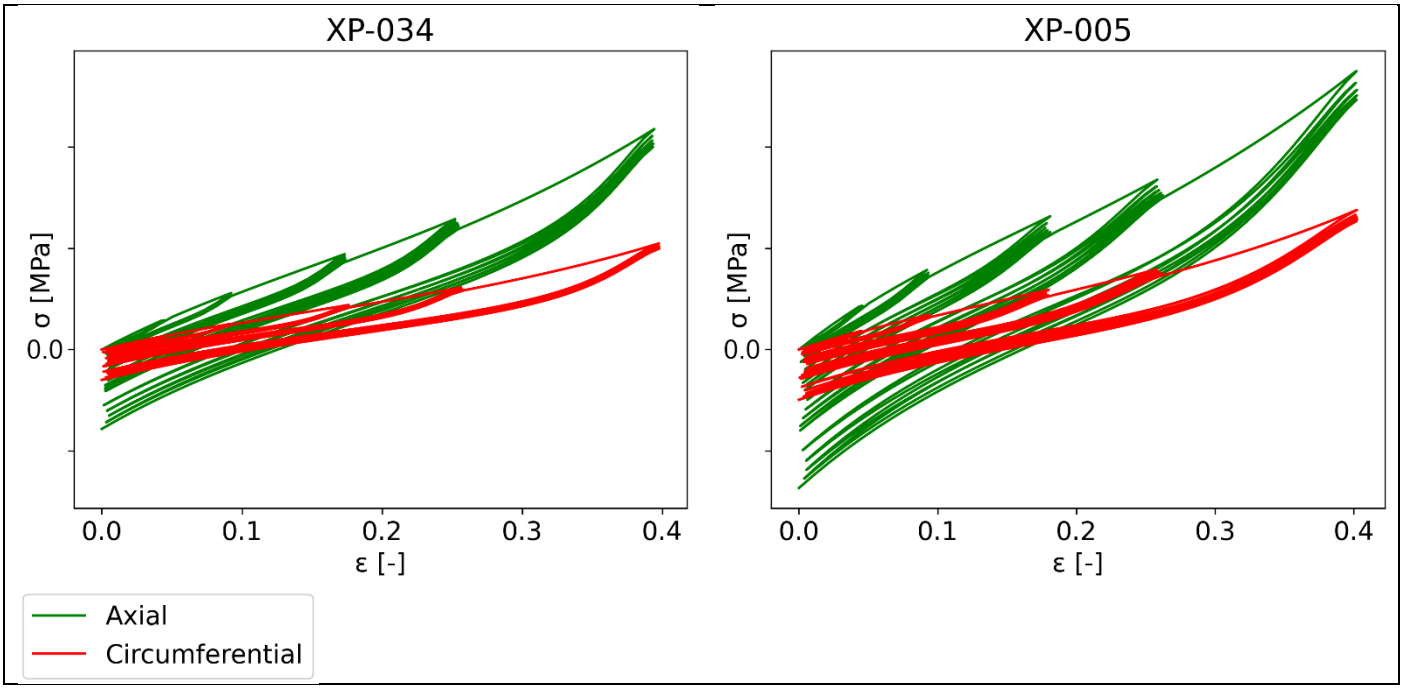

Figure 2-27: Material behavior for a cyclic load case in multiple directions, highlighting the anisotropy of XP-034 (left) and XP-005 (right). σ is the Cauchy stress in MPa and ε is the logarithmic strain both obtained from the simulation. The graphs with the numerical values are in Confidential Appendix C, Material model values.

The anisotropy definition in the material model requires a material orientation to be added to the FE model. In this material orientation definition, three directions need to be defined. The first material direction (1-axis) corresponds to the axial direction of the cylinder used during the electrospinning process. Furthermore, the second material direction (2-axis) corresponds to the circumferential direction of the cylinder used during the electrospinning process. Finally, the third material direction (3-axis) corresponds to the radial direction of the cylinder used during the electrospinning process. The difference between the nominal stiffness along the 1-axis and the 2-axis is shown in Figure 2-27. The nominal thickness in the 3-axis is approximately zero.

The material orientation definition was implemented with a discrete field. In this way, every element of the component had its material orientation. Furthermore, this ensures that two orientations lie on the element's surface, while one orientation is normal to the element's surface. This was to accurately resemble the fiber orientation due to the electrospinning process.

For the Conduit, the material orientation definition was defined such that the 1-axis points in the axial direction of the Conduit. Secondly, the 2-axis pointed in the circumferential direction of the Conduit. Finally, the 3-axis pointed to the center of the Conduit.

For the Leaflets, the 1-axis pointed in the same axial direction as when the Leaflet was assembled into the Conduit. Secondly, the 2-axis pointed in the same circumferential direction as the Conduit. To ensure the 2-axis was in the circumferential direction, three rings have been modeled around the Leaflet. The inside circumferential of these three rings was selected as the 2-axis. This is shown by the blue arrows on the three rings in Figure 2-28. Finally, the 3-axis pointed to the inside of the Leaflet. For uncertainty quantification two parameters were defined for a rotation around the 3-axis. The material orientation of the Conduit and the Leaflet is shown in Figure 2-29. All the material parameters used in the Python script are listed in Table 2-8. Numerical values of these parameters are in Confidential Appendix C, Material Model Values.

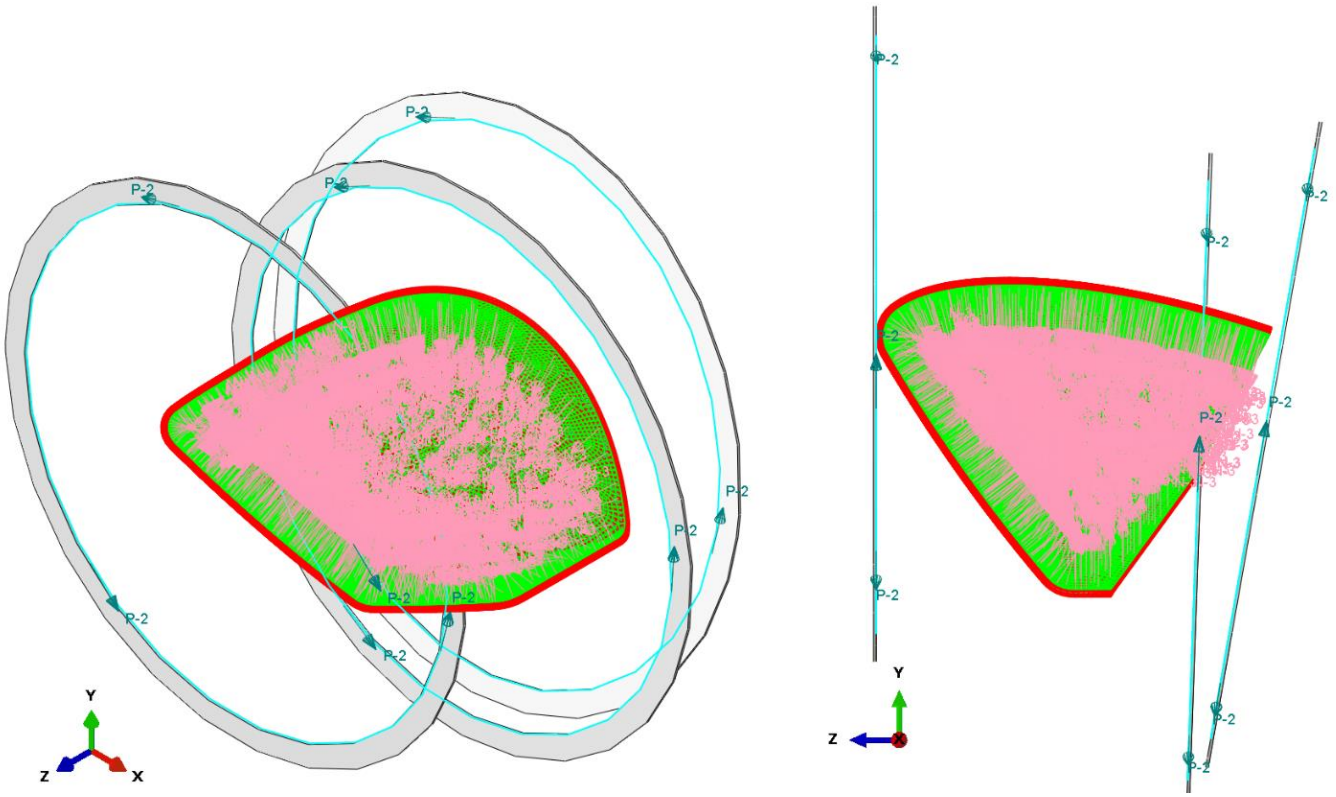

Figure 2-28: Leaflet material orientation definition, P-2 is the circumferential directional axis used by 2-axis material orientation.

Table 2-8: Material parameters, numerical values of the material parameters are in Confidential Appendix C, Material Model Values.

Parameter	Unit	Description
Mat Conduit Rotation	deg	Rotation along the third axis of the material orientation.
Mat Leaflet Rotation	deg	
Mat XP034 Density	tonne/m 3	The density of the material used in Abaqus Explicit.
Mat XP034 PR01 a11	-	Undamaged anisotropy (fiber direction, fiber stiffness, fiber geometry)
Mat XP034 PR02 a22	-	
Mat XP034 PR03 mp	MPa	
Mat XP034 PR04 gp	-	
Mat XP034 PR05 dp	-	
Mat XP034 PR06 mn	MPa	
Mat XP034 PR07 gn	-	
Mat XP034 PR08 dn	-	
Mat XP034 Poisson Ratio		Used to calculate the inverse of the bulk modulus.
Mat XP034 PR10 eta0m	-	Mullins Effect
Mat XP034 PR11 alphm	-	
Mat XP034 PR12 eta0r	-	Permanent set
Mat XP034 PR13 alphr	-	
Mat XP034 PR14 tvis1	sec	Viscoelasticity
Mat XP034 PR15 mvis1	1/MPa	
Mat XP034 PR16 tvis2	sec	
Mat XP034 PR17 mvis2	1/MPa	

Mat XP034 PR18 tvis3	sec	
Mat XP034 PR19 mvis3	1/MPa	
Mat XP005 Density	tonne/m 3	Density of the material used in Abaqus Explicit
Mat XP005 PR01 a11	-	Undamaged anisotropy (fiber direction, fiber stiffness, fiber geometry
Mat XP005 PR02 a22	-	
Mat XP005 PR03 mp	MPa	
Mat XP005 PR04 gp	-	
Mat XP005 PR05 dp	-	
Mat XP005 PR06 mn	MPa	
Mat XP005 PR07 gn	-	
Mat XP005 PR08 dn	-	
Mat XP005 Poisson Ratio	-	Used to calculate the inverse of the bulk modulus.
Mat XP005 PR10 eta0m	-	Mullins Effect
Mat XP005 PR11 alphm	-	
Mat XP005 PR12 eta0r	-	Permanent set
Mat XP005 PR13 alphr	-	
Mat XP005 PR14 tvis1	sec	Viscoelasticity
Mat XP005 PR15 mvis1	1/MPa	
Mat XP005 PR16 tvis2	sec	
Mat XP005 PR17 mvis2	1/MPa	
Mat XP005 PR18 tvis3	sec	
Mat XP005 PR19 mvis3	1/MPa	

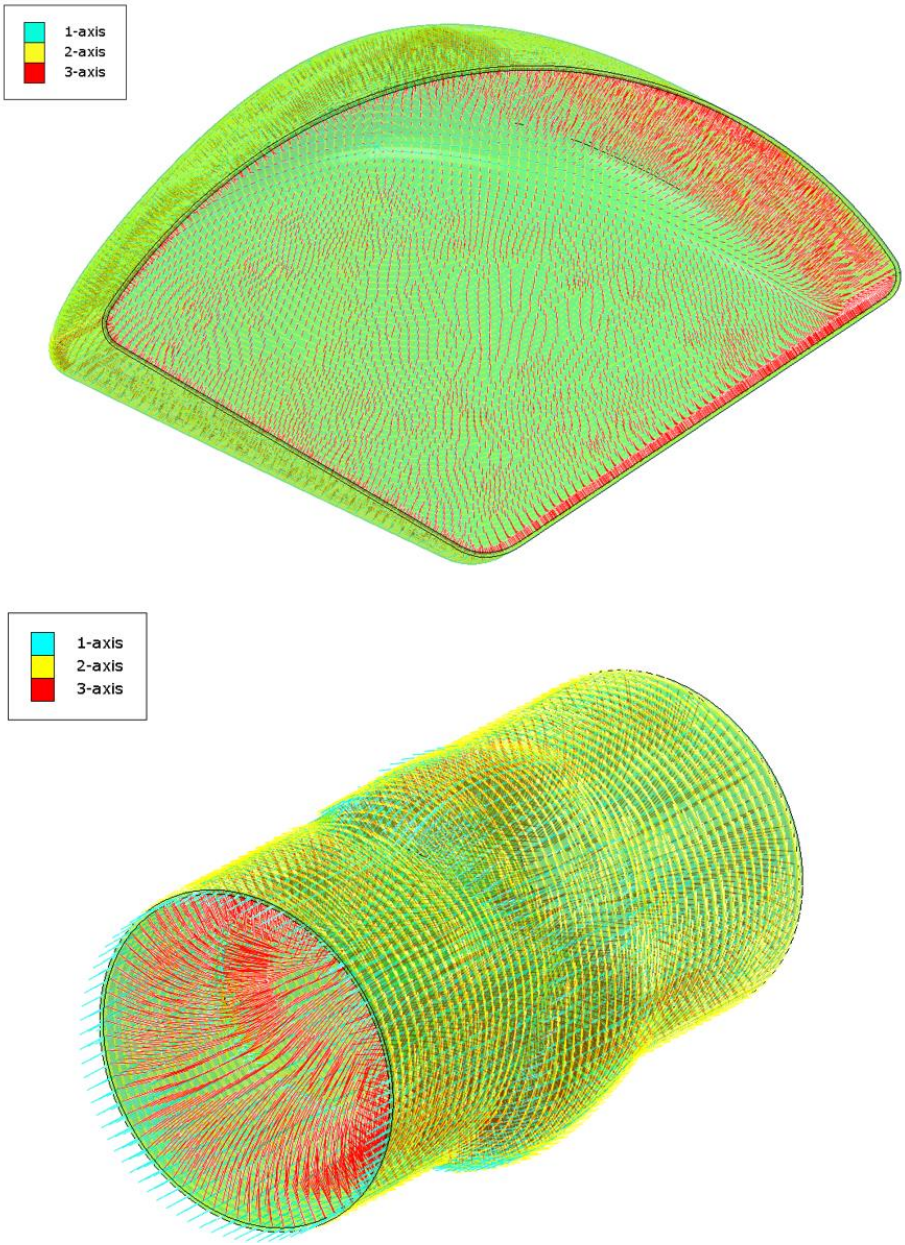

Figure 2-29: Material orientation of the Leaflet (up) and the Conduit (below)

2.3.2 Experiment Setup Material

The Pushrod and parallel plates were modeled as rigid bodies. This was an assumption as the parts are not rigid. Thus, the stiffness of the material used for the Pushrod and parallel plates needed to be compared to the stiffness of the XPV after the experiment. This was to assess the influence of the rigid body assumption.

Regarding the Leaflet opening behavior experiment, the Pushrod was manufactured with SLA 3D printing using the Formlabs™ SLA 3D printer and the material was grey resin. Regarding the parallel plate compression experiment, the bottom parallel plate and top parallel plate were made of aluminum. Specifically, EN-AW 1050A was used. From the tensile modulus and the part geometry, the part stiffness was calculated. The tensile modulus of both materials and the stiffness of the Pushrod and the parallel plates are listed in Table 2-9.

Table 2-9: Experiment components' material properties

Component	Material	Tensile modulus	Standard	Stiffness
Pushrod	Grey Resin (22)	1.6 GPa	ASTM D638-14	$1.8 * 10^3$ N/mm
Parallel plates	Aluminium (23)	69 GPa	BS EN 485-2	$1.31 * 10^8$ N/mm

2.4 MODEL DEFINITIONS

Model definitions include solver definitions, boundary conditions, constraints, and contact definitions. For the solver definitions, Dassault Systèmes Abaqus FEA software version 2021HF7 was the software used to create the model. Both the Abaqus/Implicit FE solver and the Abaqus/Explicit FE solver were used in the computational device modeling workflow. Abaqus/Implicit was used for the FS, while Abaqus/Explicit was used for the Leaflet opening behavior and parallel plate compression simulation. Abaqus/Explicit was chosen here because Abaqus/Implicit showed convergence issues caused by the non-linear material dynamics in combination with the contact dynamics between the components.

Depending on the load case, different solver definitions, BCs, constraints, and contact definitions were used. The FS used its own set of BCs, constraints, and contact definitions. The Leaflet opening behavior simulation and parallel plate compression simulation shared similar BC, constraints, and contact definitions, but there are differences.

2.4.1 CONDUIT FORMING

The FS consisted of two steps. In the first step, a negative pressure of 5 MPa was applied on the inside surface of the Conduit to fixate the Conduit in place on the rigid cylinder. In the second step, the Leaflets were moved into the Conduit, which formed the Conduit in the desired shape.

The following solver definitions were used in the first step. The step was defined as an implicit static step with a time period of 1 second. The step was solved in 10 increments. Furthermore, the following BCs were applied. First, the rigid cylinder was fixated in all degrees of freedom with a reference point (RP) located at one end of the cylinder as shown in Figure 2-30. Secondly, the Conduit was constrained in the axial direction at both ends using a cylindrical coordinate system. To prevent rotation around the axial axis the nodes lying on the yz-plane had a symmetry boundary condition in the circumferential direction. The BCs for the Conduit are shown in Figure 2-31. Finally, the Leaflets were fixed in all degrees of freedom at a reference node placed at the centroid of each Leaflet, this is shown in Figure 2-32. Regarding constraints, the Leaflets were constrained to the RP at the centroid with a rigid body constraint, which made them rigid during the simulation. A penalty formulation was used for the contact definition of the Conduit with the rigid cylinder and the Conduit with the three Leaflets. The contact stiffness was chosen as 50,000 MPa/mm. Furthermore, contact was considered with zero friction.

For the second step, the following solver definitions were used. The step was defined as an implicit static step with a time period of 1 second. The step was solved in 50 increments. In this step, the Leaflets were moved into the Conduit with a displacement BC moving the Leaflets 3 mm in the radial direction. As with the previous step, the BC was applied to the centroid of the Leaflets as shown in Figure 2-32. The Leaflets displacement forms the Conduit into the correct shape. The beginning and end state of the FS is shown in Figure 2-10. The same contact definition as the previous step was used.

The numbers for the pressure, time periods, time increments, and contact stiffness were based on a verification study done by 4RealSim™. Furthermore, the contact stiffness was chosen so that the Conduit deformation follows the Leaflet shape closely.

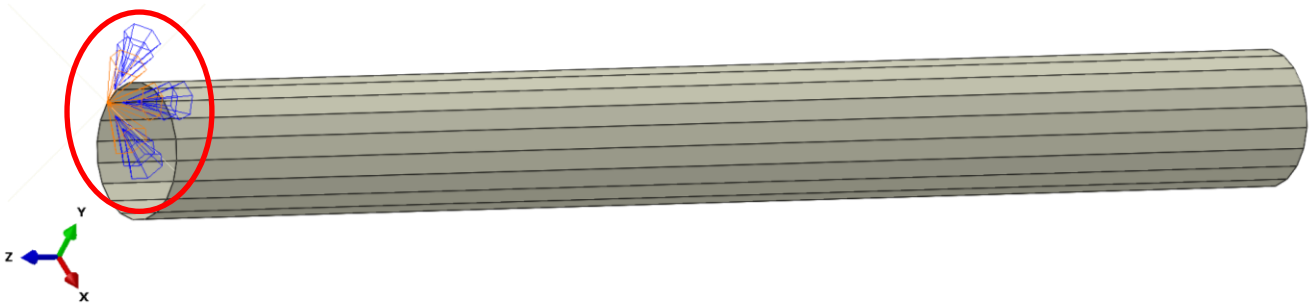

Figure 2-30: FS rigid cylinder BCs, the red circle highlights the RP used for the BC.

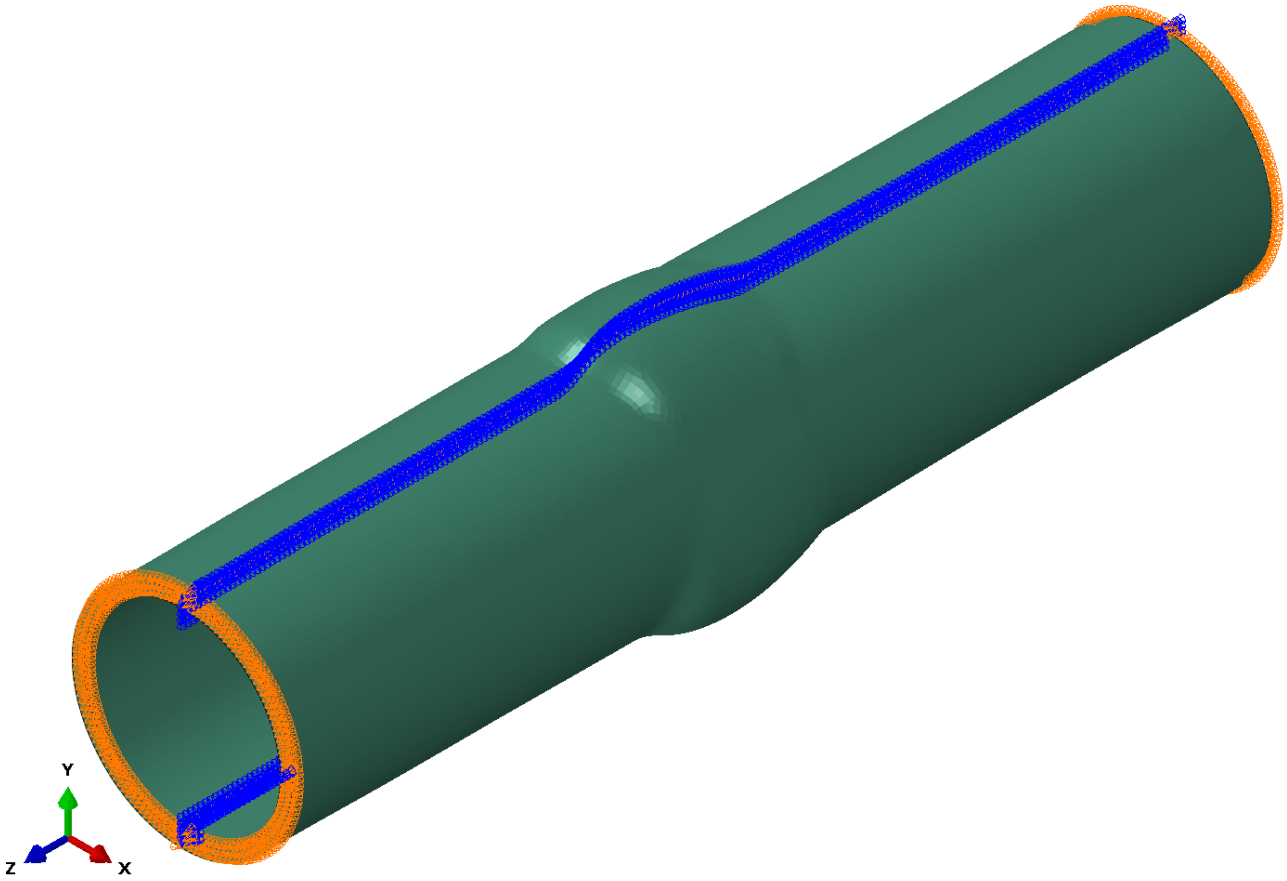

Figure 2-31: FS Conduit BCs, the BCs were applied on the highlighted edges.

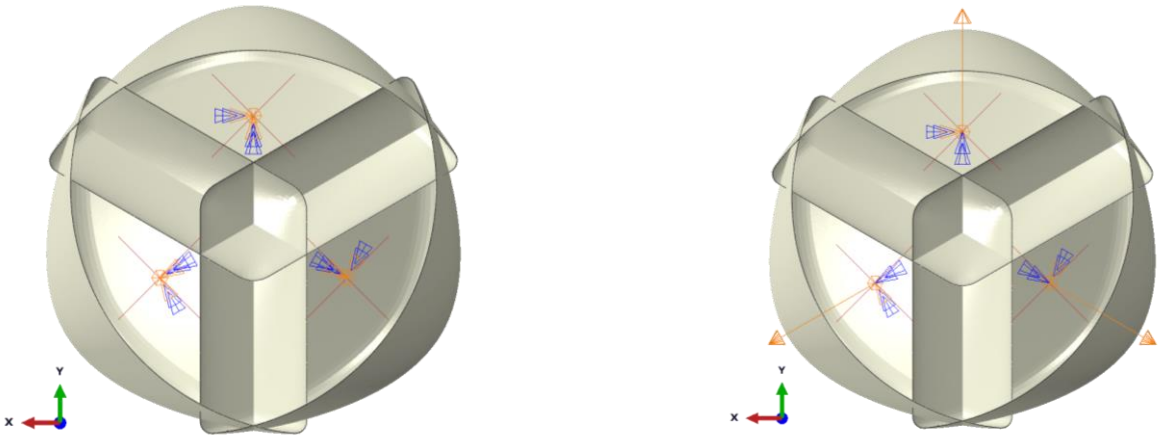

Figure 2-32: FS step 1 Leaflets BCs, the BCs were applied to the centroids of the Leaflets (left). FS step 2 Leaflets BCs, the three arrows indicate the displacement direction of the three Leaflets (right).

2.4.2 XPV

The solver definitions, BCs, constraints, and contact definitions in the XPV assembly were the same for the Leaflet opening behavior and parallel plate compression model. Thus, they will be described here separately.

The two load cases consisted of two steps. The first step was a contact initialization step where initial contact between the Leaflets was resolved as an interference fit. The following solver definitions were applied to this step. The step was defined as a dynamic explicit step with a time period of 0.1 seconds. Furthermore, the following BCs were applied. First, the Conduit was fixed in the axial and circumferential direction in a cylindrical coordinate system with a boundary condition at both ends of the Conduit as shown in Figure 2-33.

A penalty formulation was used for the contact definition of the Conduit with the three Leaflets. Furthermore, a penalty formulation was used for the contact definition between the Leaflets. A friction coefficient of 0.01 was used to improve the numerical stability of the simulation. Finally, the Leaflets were fixed to the Conduit with a tie constraint.

The second step adds BCs, constraints, and contact definitions specific to the load case considered. Before applying BCs, constraints, and definitions for LC1 and LC2, the XPV model has been tested with a pressure load case as described in Appendix C, XPV FE Model Pressure Load Case Test.

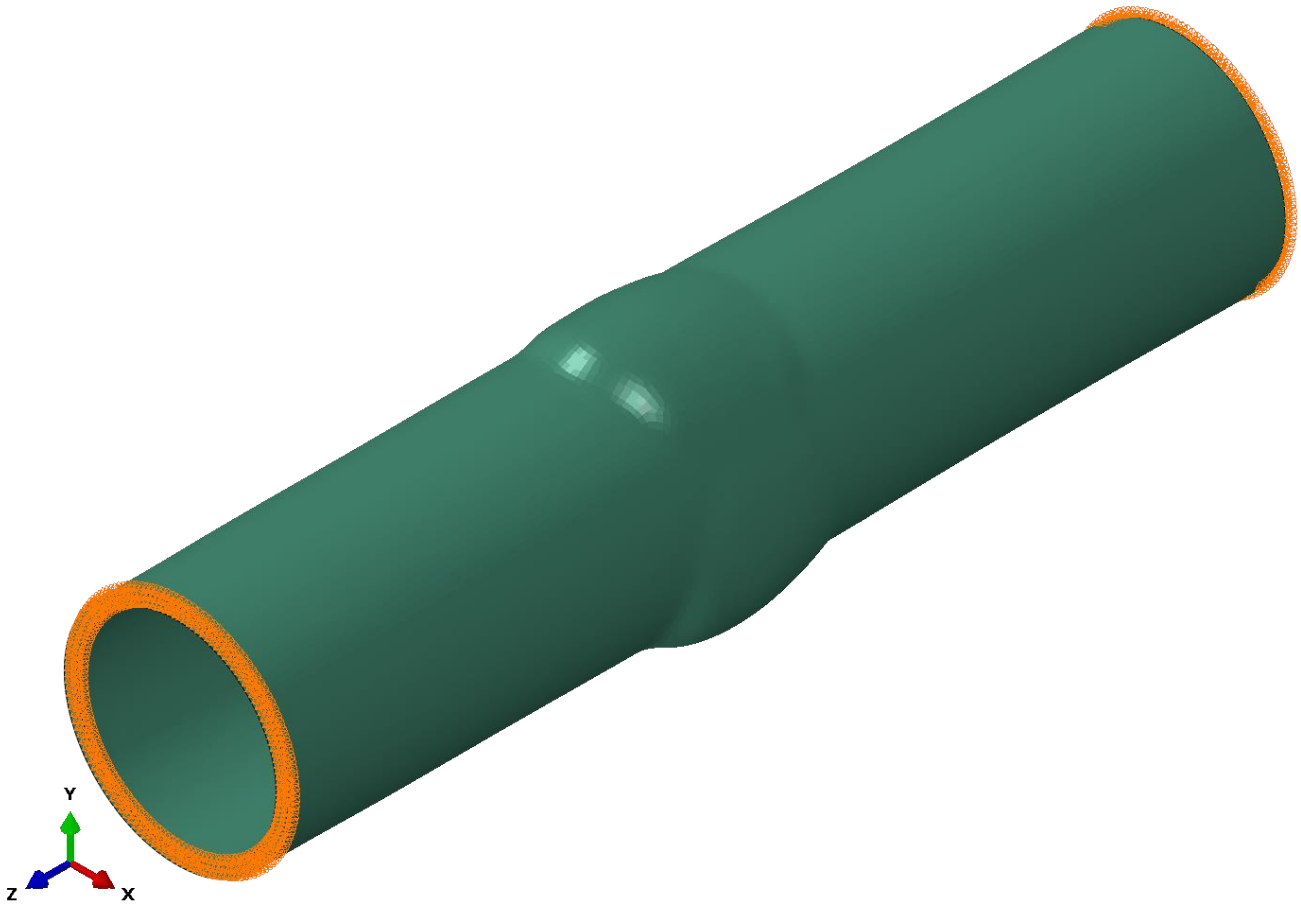

Figure 2-33: XPV model Conduit BCs

2.4.3 Leaflet Opening Behavior

The solver definitions, BCs, constraints, and contact definitions described in 2.4.2 were used in this model. As an addition to the contact initialization step solver definitions, mass scaling was applied such that the stable time increment was 5e-4 throughout the simulations. This was checked every 1000 increments. Furthermore, as the load case used a symmetrical model the following BCs were added in the first step. First, the nodes of half of the Leaflet and half of the Conduit that lies on the symmetry plane had a symmetry BC such that they were fixed in the circumferential direction. Secondly, the symmetry plane was fixed to all degrees of freedom using an RP. Lastly, the Pushrod was locked in all degrees of freedom using an RP. The BCs are shown in Figure 2-34.

A contact definition was added that describes the contact between the Pushrod and the Leaflets. This contact definition used a penalty contact formulation. A friction coefficient of 0.7 was defined by doing an inclining ramp test between a wet XPV sample and the 3D-printed material.

In the second step, the following solver definitions were applied. The step was defined as a dynamic explicit step with a time period of 15 seconds. The same mass scaling definition was used such that the stable time increment was 5e-4 throughout the simulations. This is checked every 1000 increments. Furthermore, a displacement BC condition was added to the Pushrod, moving it into the Leaflets for 12.5 mm until the valve was pushed open. This amount of displacement together with the time period ensures the Pushrod was moved at a speed of 50 mm/min to match the experiments. Finally, a viscous pressure of 1e-6 MPa was applied to the inside surface of the Leaflets (see Figure 2-35) to improve the numerical stability of the simulation.

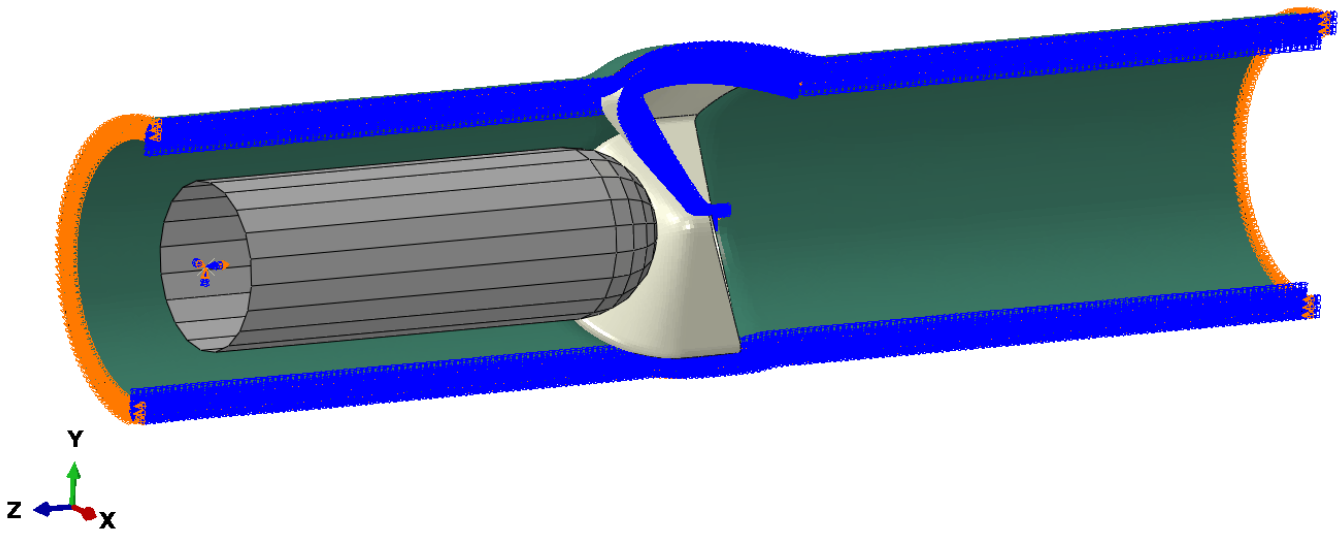

Figure 2-34: Leaflet opening boundary conditions, symmetry plane removed for clarity.

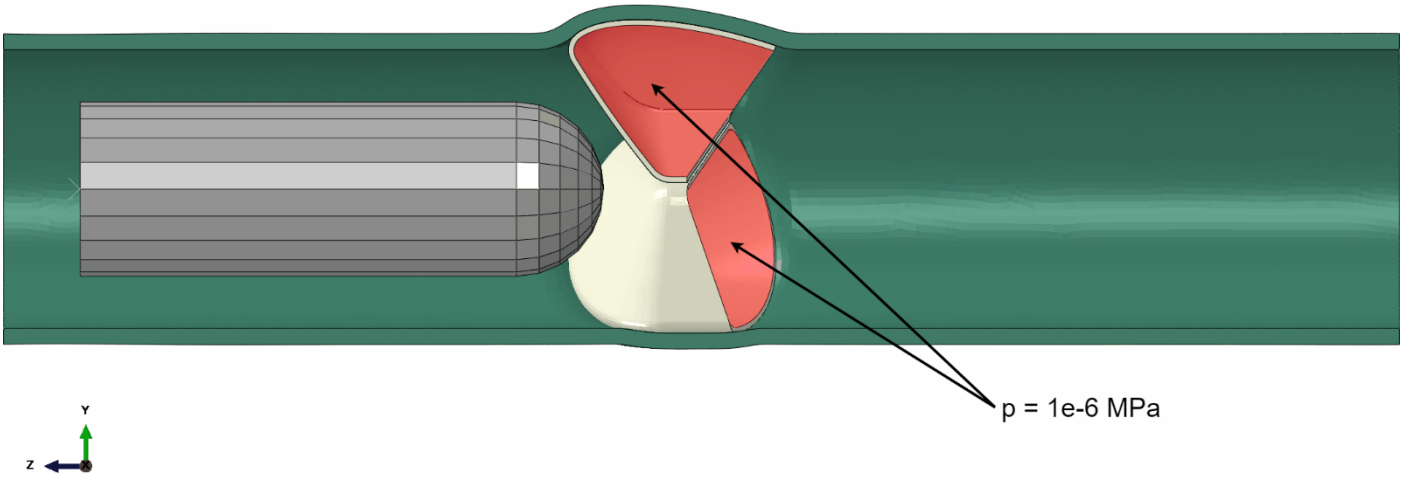

Figure 2-35: Leaflet opening viscous pressure surfaces, symmetry plane removed for clarity.

2.4.4 *Parallel Plate Compression*

The solver definitions BCs, constraints, and contact definitions described in 2.4.2 were used in this assembly. As an addition to the contact initialization step solver definitions, mass scaling was applied such that the stable time increment was 5e-5 throughout the simulations. This was checked every 1000 increments. Furthermore, as the load case used a symmetrical model, the following BCs were added in the first step. First, the nodes that lie on the symmetry plane had a symmetry BC such that they were fixed in the circumferential direction. Secondly, the symmetry plane was fixed in all degrees of freedom using an RP. Lastly, both the bottom parallel plate and the top parallel plate were fixed in all degrees of freedom. The BCs are shown in Figure 2-36.

A contact definition was added that describes the contact between the parallel plates and the Conduit. This contact definition used a penalty contact formulation. A friction coefficient of 0.69 was found by doing an inclining ramp test between a wet XPV sample and the aluminium top plate.

In the second step, the following solver definitions were applied. The step was defined as a dynamic explicit step with a time period of 2.34 seconds. The same mass scaling definition was used such that the stable time increment was 5e-4 throughout the simulations. This was checked every 1000 increments. Furthermore, a displacement BC condition was added to the top parallel plate, moving it into the XPV which caused it to compress. The compression was 20% for each XPV variant (XPV16, XPV18, and XPV20). The amount of compression and the time period ensured the top parallel plate moved down at a speed of 100 mm/min to match the experiments. Finally, a viscous pressure of 1e-6 MPa was applied instantaneously to the inside surface of the Conduit and the outside surface of the Leaflets (see Figure 2-37) to improve the numerical stability of the simulation.

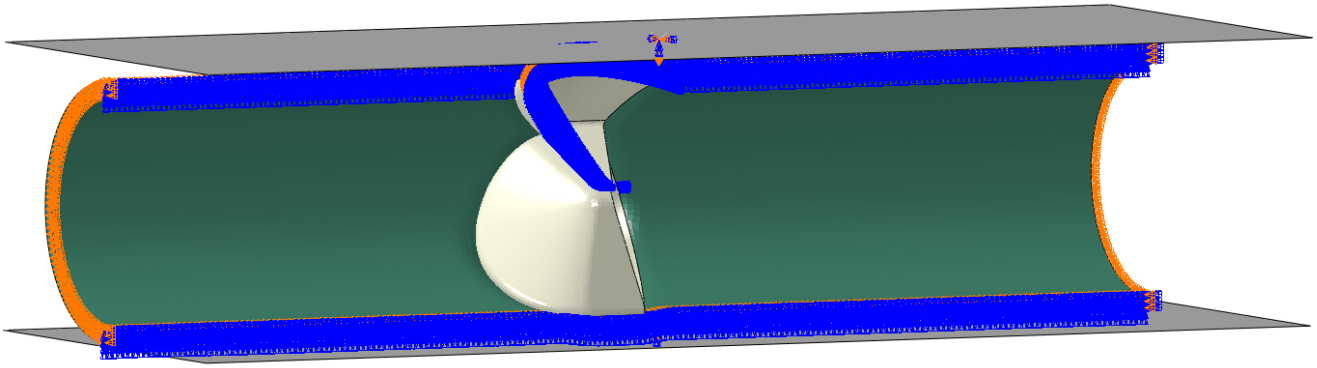

Figure 2-36: Parallel plate compression boundary conditions, symmetry plane removed for clarity.

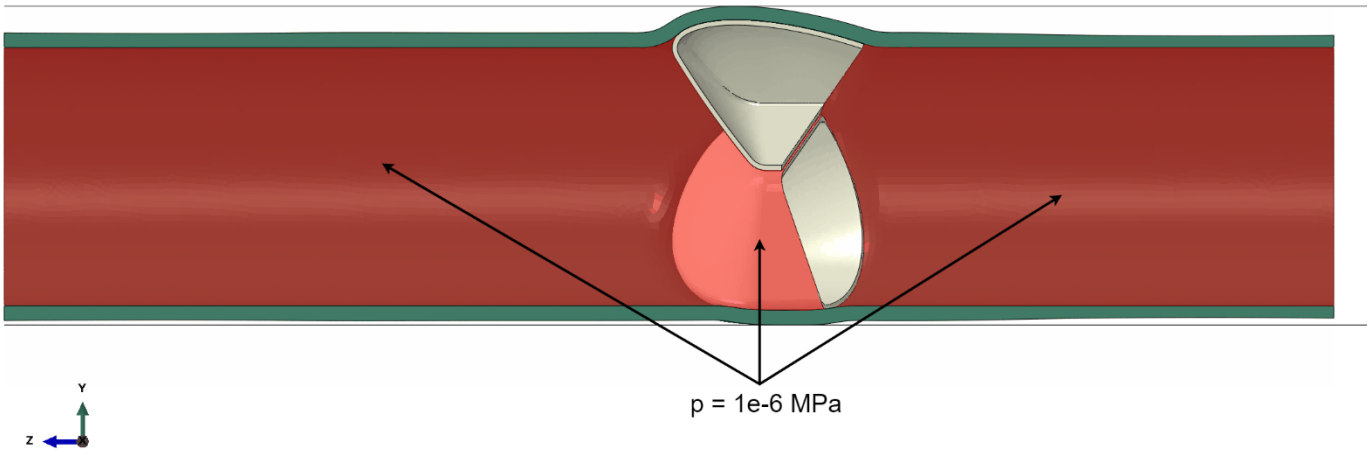

Figure 2-37: Parallel plate viscous pressure surfaces, symmetry plane removed for clarity.

2.5 Computational Model Data Generation Process

Now that all the components of the computational model are described, the simulation workflow will be described here. The first step of the model generation process was to create the desired Conduit using the FS, as shown in Figure 2-10. The FS received parameters for the Conduit geometry and the Leaflets geometry. Furthermore, the FS received definitions for the applied loads, boundary conditions (BCs), constraints, contact definitions, material definitions, mesh definitions, and solver definitions. The FS resulted in the formed Conduit geometry. The formed Conduit geometry and the Leaflets geometry defined before the FS were used with the material parameters to create the two load case models. The load case models also received their definitions for loads, BCs, contact definitions, constraints, contact, added geometry, and solver definitions. Furthermore, the Leaflet opening behavior model received parameters regarding the Pushrod misalignment. The output of the Leaflet opening behavior simulation was data on the Pushrod reaction force and displacement. The output of the parallel plate compression simulation was data on the top parallel plate reaction force and displacement. This data was used to compare the models to the experiments. The computational model process flowchart to generate the output data is shown in Figure 2-38. For parameter assignment and model generation with the model definitions, Python scripts were used. Furthermore, the output of the simulations was obtained by Python scripts as well. The model generation process was automated with an Isight model by 4RealSim™.

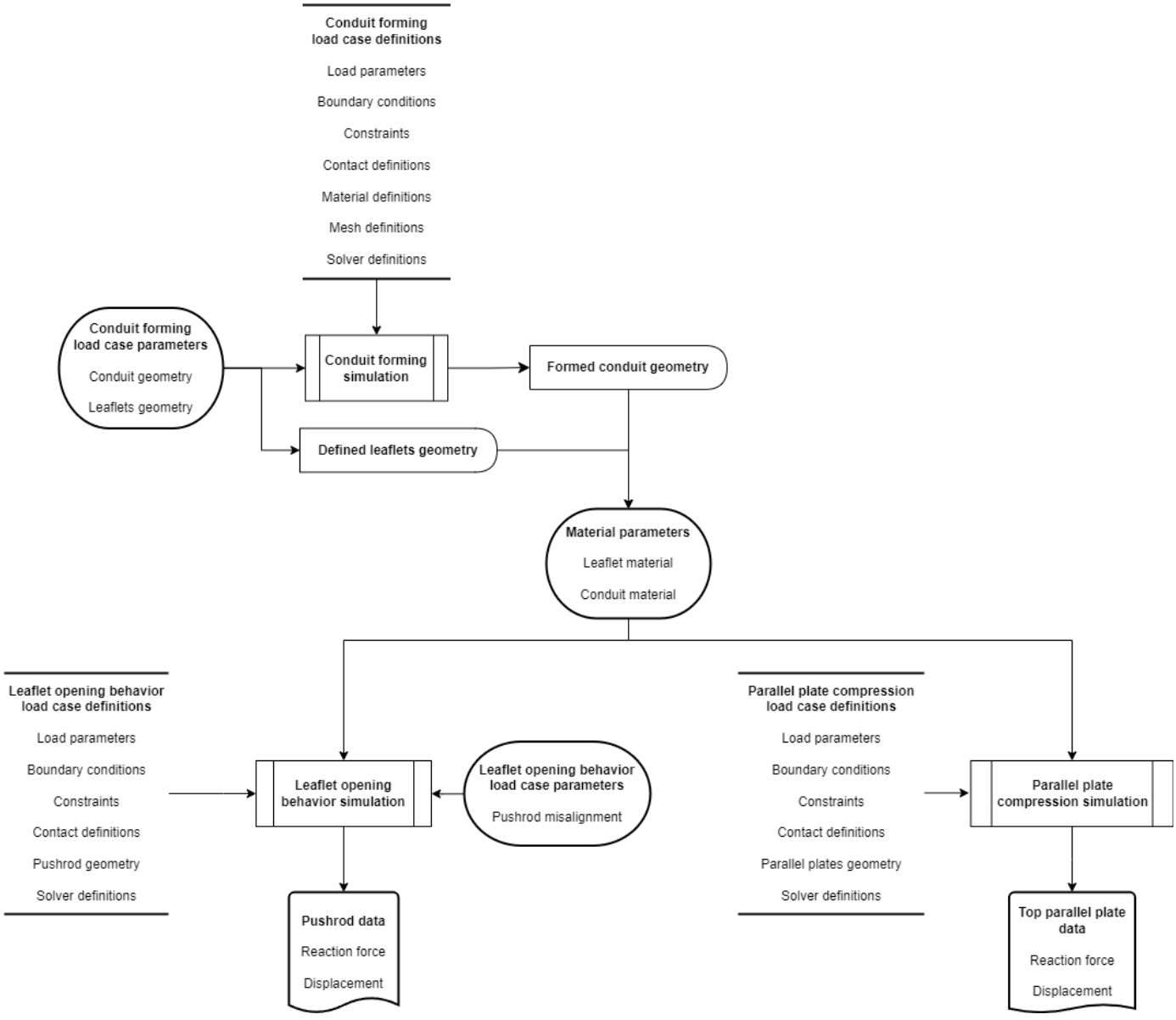

Figure 2-38: Model generation process

2.6 COMPUTATIONAL MODEL DATA GENERATION

Variations in the device geometry, material parameters, and experiment execution cause the output of the experiment to be different from the output of the computational model. Incorporating these possible variations in the model is called uncertainty quantification (UQ) (7). Incorporating uncertainty in the model with input parameters allows a sensitivity analysis to be performed. With sensitivity analysis, the influence of the input parameters on the output parameters is quantified. Furthermore, the output of the computational model will be a distribution instead of a single value that can be compared to the experiments (24). This sensitivity analysis and output distribution generation were performed by 4RealSim™ using Isight, and the method is described below.

The input variables were defined as distributions. The input variables with their distribution were based on prior measurements, experiments, preliminary simulations, or engineering judgment (24).

The input values that were used in the computational model were randomly chosen with a Monte Carlo simulation (25). In the Monte Carlo simulation, lower and upper bounds were defined for the random selection of input values. The upper and lower bounds were defined as two times the standard deviation (STD) from the mean for a Gaussian distribution.

Monte Carlo simulations require many sample points so that the mean of the output comes close to the expected value according to the Law of Large Numbers (26). Obtaining many sample points through FE simulations requires many computational resources and becomes unfeasible for complex FE models. Surrogate modeling or metamodeling provides a different approach to generating the required samples.

Metamodeling provides an approximation of the relationship between the input and the output. It is a mathematical model that can take the form of a polynomial. It is usually of a much smaller size and uses less computational resources than an FE simulation (24).

A metamodel (MM) was created by first performing multiple FE simulations with random input values bounded by the parameter's distribution. The range of the distributions was larger than the expected distribution. For instance, for a Gaussian distribution, the range was increased to three times the STD. Increasing the range ensured that the metamodel would interpolate the results rather than extrapolate. Each FE simulation created a design of experiment (DoE). After multiple DoE's were created, a metamodel could be generated by interpolating the parameter space between the DoE's through regression (24). This approach is visualized in Figure 2-39. The meta-model could then be used to create the large number of samples required for the Monte Carlo simulation (26).

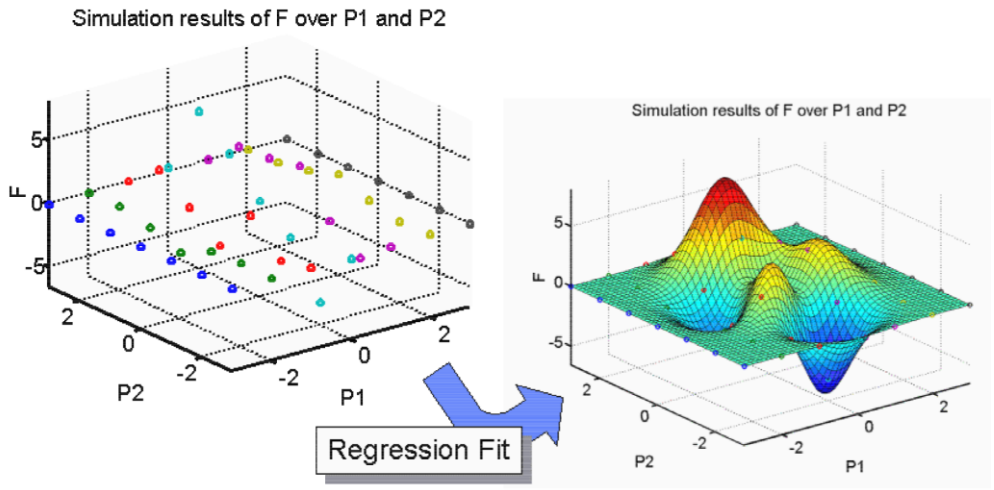

Figure 2-39: Interpolating the parameter space through regression using the DoE's as data points (24)

2.6.1 LEAFLET OPENING BEHAVIOR

Regarding the Conduit geometry parameters, for the Leaflet opening behavior model the parameters regarding the Conduit geometry were fixed except for the Conduit thickness distribution. The thickness distribution of the Conduit was assumed uniform; thus the 5 thickness parameters were identical. This was based on the preliminary simulations done. The distribution was a gaussian distribution with an STD that was the maximum STD out of the 5 thickness parameters.

Regarding the Leaflet geometry parameters, the thickness distribution on the main regions of the Leaflets was defined as uniform based on μCT measurements. Furthermore, the differences between the Leaflets were neglected as there were no significant differences found in the μCT measurements. Finally, no misalignment of the Leaflets was assumed in the XPV assembly.

In total 6 geometry parameters were considered in the creation of DoE's for the Leaflet opening behavior model data generation. Regarding the material parameters, a total of 16 material parameters were used, 8 for the Conduit material and 8 for the Leaflet material. Furthermore, two parameters were considered for the test setup, regarding the Pushrod misalignment. This brought the total number of input parameters used to create the DoEs to 24, which are listed in Table 2-10. The numerical values for the distributions used, mean and STD for these parameters are in Confidential Appendix A, Conduit Geometry Parameters Values, Confidential Appendix B, Leaflet Geometry Parameters Values, and Confidential Appendix C, Material Model Values.

Table 2-10: LC1, parameters used to create the DoEs.

Parameter	Unit	Description
Conduit_t1	mm	Conduit thickness
Leaflet_Belly_β_0	mm	Leaflet Belly thickness
Leaflet_Side_β_0	mm	Leaflet Side thickness
Leaflet_Top_β_0	mm	Leaflet Top thickness
Leaflet_TL	mm	Leaflet trim length
Leaflet_TA	deg	Leaflet trim angle
Mat_XP005_PR01_a11	-	Conduit material, undamaged anisotropy (fiber direction, fiber stiffness,
Mat_XP005_PR02_a22	-	fiber geometry)
Mat_XP005_PR03_mp	MPa	
Mat_XP005_PR04_gp	-	
Mat_XP005_PR05_dp	-	
Mat_XP005_PR06_mn	MPa	
Mat_XP005_PR07_gn	-	
Mat_XP005_PR08_dn	-	
Mat_XP034_PR01_a11	-	Leaflet material, undamaged anisotropy (fiber direction, fiber stiffness,
Mat_XP034_PR02_a22	-	fiber geometry)
Mat_XP034_PR03_mp	MPa	
Mat_XP034_PR04_gp	-	
Mat_XP034_PR05_dp	-	
Mat_XP034_PR06_mn	MPa	
Mat_XP034_PR07_gn	-	
Mat_XP034_PR08_dn	-	
Pushrod_y-offset	mm	Pushrod y-axis offset
Pushrod_x-rotation	deg	Pushrod x-axis rotation

The input variables for the DoE were defined as distributions. The parameters for the XPV geometry were defined with Gaussian distributions with a mean and STD. The values for the mean and STD were based on prior measurements. The material parameter distributions were based on experiments done by TU Graz (19). The distribution for the Pushrod position was chosen as uniform with upper and lower limits based on the design of the experimental setup. The numerical values with the distribution for the Pushrod position parameters are listed in Table 2-11. After the DoE simulations, more information about the Pushrod misalignment was available and the distribution was changed to a Gaussian distribution for the Monte Carlo simulations, as listed in Table 2-12. The Pushrod x-rotation was removed from the Monte Carlo simulations as this parameter was approximately zero for all sizes (see Appendix B, LC1 Misalignment Measurements).

Table 2-11: LC1, numerical values and distributions for the Pushrod position parameters, implemented in the creation of the DoEs.

Parameter	Unit	Distribution	Nominal	Upper bound	Lower bound
Pushrod_y-offset	mm	Uniform	0.0	-2.0	2.0
Pushrod_x-rotation	deg	Uniform	0.0	-1.5	1.5

Table 2-12: LC1, numerical values, and distributions for the Pushrod position parameters, implemented in the Monte Carlo simulations.

			XPV16		XPV18		XPV20	
Parameter	Unit	Distribution	Mean	STD	Mean	STD	Mean	STD
Pushrod_y-offset	mm	Gaussian	0.83	0.58	0.85	0.25	1.19	0.74

The output data of a simulation was a force-displacement curve of the reaction force of the Pushrod and its displacement. From this curve, the peak reaction force was used as an output parameter. Furthermore, the stiffness was calculated between 60% and 75% of the peak force. Thus, two output parameters were used in this load case. An example of a force-displacement plot of the Leaflet opening behavior simulation is shown in Figure 2-40.

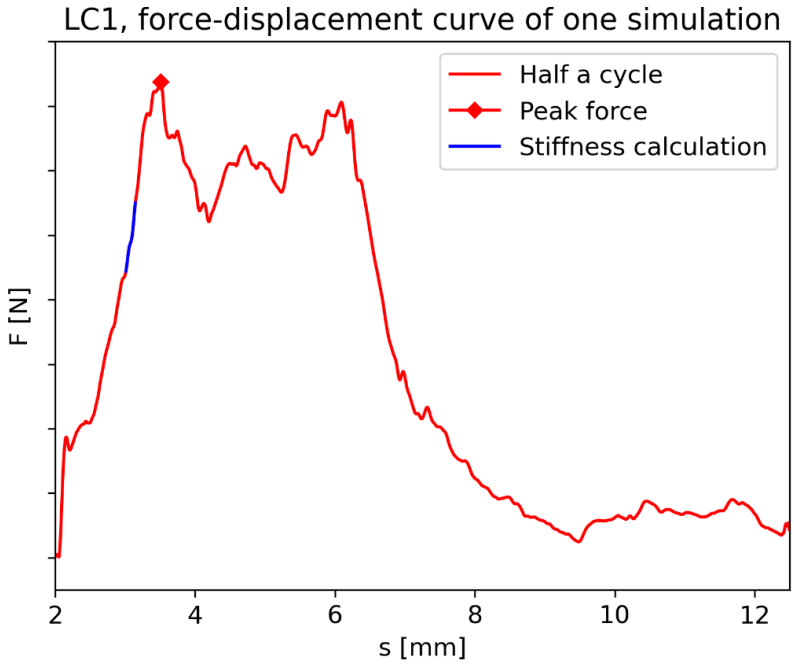

Figure 2-40: LC1, a force-displacement curve from one simulation. F is the force on the Pushrod in N and s is the displacement of the Pushrod in mm. The graph with the numerical values of the force is in Confidential Appendix E, Two Force-Displacement Curves of the Simulations.

2.6.2 PARALLEL PLATE COMPRESSION

Regarding the Conduit, all the Conduit parameters were used in the DoE simulations, except the trim angle parameters. This is because all the Conduits were straight for these experiments.

Regarding the Leaflet geometry parameters, the thickness distribution on the main regions of the Leaflets was defined as uniform based on μCT measurements. Furthermore, the differences between the Leaflets were neglected as there were no significant differences found in the μCT measurements. Finally, no misalignment of the Leaflets was assumed in the XPV assembly.

In total 12 geometry parameters were considered in the creation of DoE's for the Leaflet opening behavior model data generation. Regarding the material parameters, a total of 16 material parameters were used, 8 for the Conduit material and 8 for the Leaflet material. This brought the total number of input parameters used to create the DoEs to 28, which are listed in Table 2-13. The numerical values for the distributions used, mean and STD for these parameters are in Confidential Appendix A, Conduit geometry parameters values, Confidential Appendix B, Leaflet geometry parameters values, and Confidential Appendix C, Material model values.

Table 2-13: LC2, parameters used to create the DoEs.

Parameter	Unit	Description
Conduit_L	mm	Conduit length
Conduit_VS	mm	Conduit ventricle side to sinus
Conduit_t1	mm	Conduit thickness 1
Conduit_t2	mm	Conduit thickness 2
Conduit_t3	mm	Conduit thickness 3
Conduit_t4	mm	Conduit thickness 4
Conduit_t5	mm	Conduit thickness 5
Leaflet_Belly_β_0	mm	Leaflet Belly thickness
Leaflet_Side_β_0	mm	Leaflet Side thickness
Leaflet_Top_β_0	mm	Leaflet Top thickness
Leaflet_TL	mm	Leaflet trim length
Leaflet_TA	deg	Leaflet trim angle
Mat_XP005_PR01_a11	-	Conduit material, undamaged anisotropy (fiber direction, fiber stiffness,
Mat_XP005_PR02_a22	-	fiber geometry)
Mat_XP005_PR03_mp	MPa	
Mat_XP005_PR04_gp	-	
Mat_XP005_PR05_dp	-	
Mat_XP005_PR06_mn	MPa	
Mat_XP005_PR07_gn	-	
Mat_XP005_PR08_dn	-	
Mat_XP034_PR01_a11	-	Leaflet material, undamaged anisotropy (fiber direction, fiber stiffness,
Mat_XP034_PR02_a22	-	fiber geometry)
Mat_XP034_PR03_mp	MPa	
Mat_XP034_PR04_gp	-	
Mat_XP034_PR05_dp	-	
Mat_XP034_PR06_mn	MPa	
Mat_XP034_PR07_gn	-	
Mat_XP034_PR08_dn	-	

The input variables for the DoE were defined as distributions. The parameters for the XPV geometry were defined with Gaussian distributions with a mean and STD. The values for the mean and STD were based on prior measurements. The material parameter distributions were based on experiments done by TU Graz (19).

The output data of a simulation was a force-displacement curve of the reaction force of the top parallel plate and its displacement. From this curve, the reaction force at 3 mm displacement was used as an output parameter (F_p). Furthermore, the stiffness is calculated between 2.5- and 3.5-mm displacement. Thus, two output parameters were used in this load case. An example of a force-displacement plot of the Leaflet opening behavior simulation is shown in Figure 2-41.

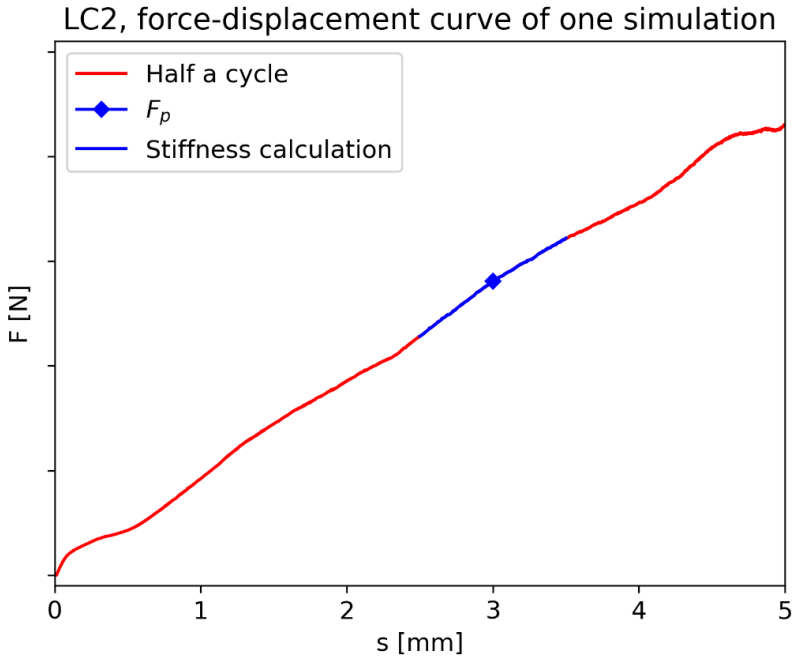

Figure 2-41: LC2, a sample force-displacement curve obtained from the parallel plate compression simulations. F is the force on the top parallel plate in N and s is the displacement of the top parallel plate in mm. The graph with the numerical values of the force is in Confidential Appendix E, Two Force-Displacement Curves of the Simulations.

2.6.3 Data Processing

With the 24 input parameters and 2 output parameters, 150 FE simulations were done for the three device sizes in the model of LC1. Furthermore, With the 28 input parameters and 2 output parameters, 150 FE simulations were done for the three device sizes in the model of LV2. This brings the total number of DoE FE simulations to 900.

From these DoE's an MM was created for the two models. The MM was a fourth-order polynomial fit based on a least square regression for both models. With the MM, a total of 10,000 data points were generated for the Monte Carlo simulation for each model. From the Monte Carlo simulations, a statistical analysis was performed for both models. The average values and variations were calculated for the output parameters for both models. Furthermore, the distribution of the outputs was created with probability distribution functions (PDFs) and cumulative distribution functions (CDFs) for both models. Finally, the sensitivity of the input parameters to the output parameters was extracted from Isight based on the Monte Carlo simulation for both models. This sensitivity is also called the probabilistic sensitivity and is calculated using a standardized least-squares first-order polynomial fit. Before the fitting is done the input data is scaled from -1 to 1 so comparing multiple sensitivity values can be done. The sensitivity values from the polynomial fit are normalized by dividing each sensitivity value by the sum of all the sensitivity values (16). The input parameters are listed in Table 2-10 for LC1 and Table 2-13 for LC2. The output parameters are the maximum peak force and the stiffness for LC1, and the F_p and the stiffness for LC2. The sensitivity analysis provided useful information about potential parameters used in the model that have insignificant influence on the output parameters and can be removed from the metamodel. Removing redundant parameters from the metamodel decreases the amount of FE simulations necessary. This makes the metamodel more efficient in computational resource usage (24).

3 Results and Discussion

3.1 Experiment Results

3.1.1 LC1, Leaflet Opening Behavior

Figure 3-1 shows the force-displacement curve of one XPV20 sample during LC1. The graph with the numerical values of the force is in Confidential Appendix D, Results and Discussion Graphs. In the figure, each cycle is shown with a different color to highlight the differences between each cycle. From the figure, the first cycle has the highest peak force. After the first cycle, the peak force becomes lower with each cycle. Furthermore, the decrease in peak force is the most notable from the first cycle to the second cycle. This could be explained by the Mullins softening effect present in the material [21]. The decrease in the peak force from the second cycle onwards could be explained by plastic deformation in the material. At higher displacement values, where the Pushrod has moved through the valve, a big jump in the reaction force can be observed. Here the measured reaction force changes from a positive value to a negative value. This happens when the Pushrod switches from being pushed into the valve to being pulled outside of the valve. The big jump can be explained by the friction between the Pushrod and the valve. The force-displacement curves of every sample for LC1 highlighting the first half cycle, stiffness calculation region, and peak force are shown in Appendix E, LC1 Force Displacement Curves of the Experiments.

Figure 3-2 shows the first half cycle during the experiment for all samples and all cycles. The graphs with the numerical values of the force are in Confidential Appendix D, Results and Discussion Graphs. In the figure, each sample has its color in the graphs, defined in Table 3-1. The variation in the axial position of the Leaflets in the Conduit is visible from the variation in displacement values of the peak force. The XPV16 has the least variation in this, as the peak force occurs between 14- and 17-mm displacement values. Regarding the XPV18, the Leaflets are positioned closer to the ventricle side of the Conduit, as the peak force occurs between 8- and 15-mm. The XPV20 shows the largest variation in the Leaflets' axial position in the Conduit, as here the peak force occurs between 8- and 18-mm displacement value. The variations in the Leaflets' axial position in the Conduit can be explained by variations in manufacturing. This variation can occur when the Leaflets are put into the mold for the Conduit for the electrospinning machine.

Figure 3-3 shows the cumulative distribution functions (CDFs) of the peak force values and stiffness values for all XPV sizes extracted from the force-displacement curves. The CDF plots show the probability of the peak force or the stiffness of having a value less than or equal to a specific value on the horizontal axis. Figure 3-4 shows the boxplots showing the medians and distributions of the peak reaction force values and the stiffness values for LC1 obtained from the experiments of all three sizes. The graphs with the numerical values of the peak force values and stiffness values are in Confidential Appendix D, Results and Discussion Graphs. Both the CDFs and the boxplots give information about the statistical distribution of the peak force values and the stiffness values from the experiments. From the distributions, the mean value of the peak force increases with larger device sizes. This indicates that larger Leaflets provide a higher resistance to being opened. The distribution of the peak force values of the XPV18 and the XPV20 looks similar, but the XPV16 has two samples that show a smaller peak force. This results in the XPV16 having a larger distribution in peak force values than the other two XPV sizes. Looking at the stiffness values, the mean value of the stiffness differs slightly across device sizes. The main difference can be observed in the distribution of the stiffness values. The XPV16 has a larger stiffness distribution than the XPV18 and the XPV20, with stiffness values lower and higher than the stiffness values found in the XPV18 and the XPV20. Comparing the stiffness value from the experiments with the stiffness value of the Pushrod (listed in Table 2-9), the Pushrod is approximately 1e4 times stiffer than the stiffness values measured in the experiments, thus the effect of the Pushrod stiffness can be neglected.

Thus, with the help of mechanical experiments, the difference in mechanical response for the XPV16, XPV18, and XPV20 have been quantified for the Leaflet opening behavior load case. The peak force increases when the device size increases while the stiffness doesn't change with device size. Furthermore, the XPV16 has the highest variance in peak force values and stiffness values.

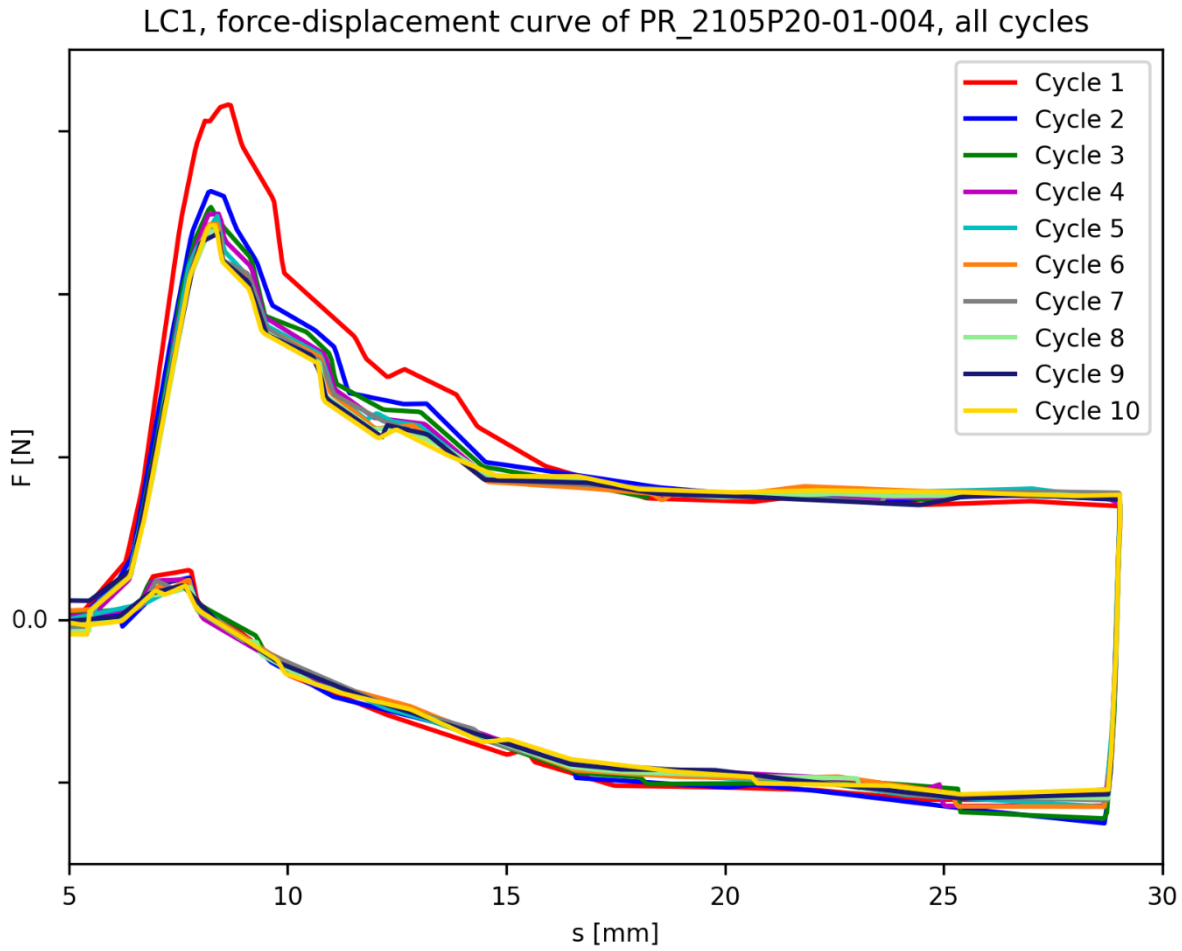

Figure 3-1: LC1, force displacement curve of an XPV20 sample, showing all cycles during one experiment. F is the force measured by the load cell in N and s is the displacement of the load cell in mm. The graph with the numerical values of the force is in Confidential Appendix D, Results and Discussion Graphs.

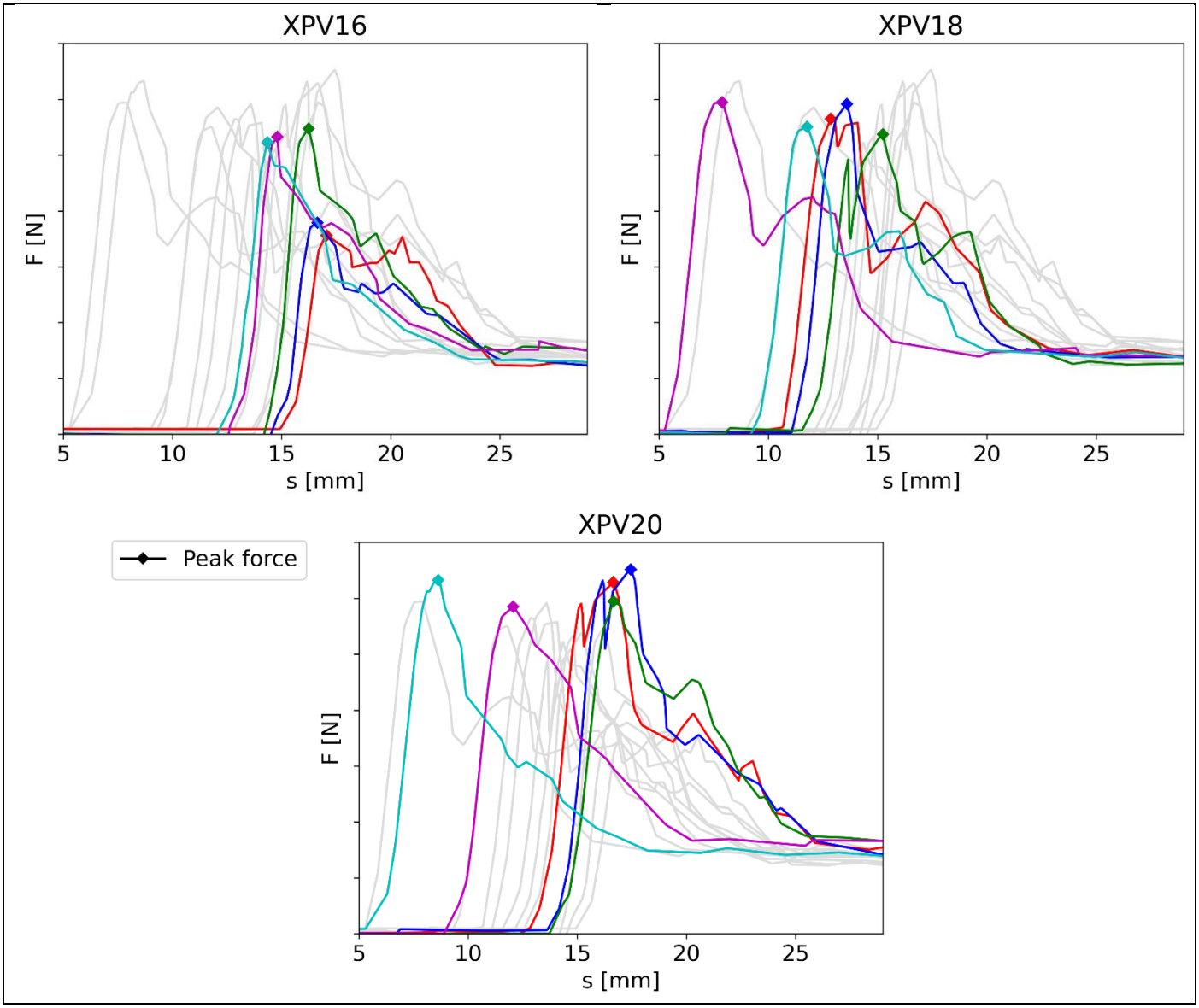

Figure 3-2: LC1, first half cycle of all samples of the XPV16 (top-left), XPV18 (top-right), and XPV20 (bottom) during the experiment. The different colors correspond to the samples tested as listed in Table 3-1. In each plot, the other XPV sizes are shown in gray for comparison. F is the force measured by the load cell in N and s is the displacement of the load cell in mm. The graphs with the numerical values of the force are in Confidential Appendix D, Results and Discussion Graphs.

Table 3-1: Colors corresponding to which sample of each XPV size in Figure 3-2.

Color	XPV16 sample	XPV18 sample	XPV20 sample
	PR_2008P16-01-028	PR_2106P18-01-002	PR_2010P20-01-007
	PR_2008P16-01-030	PR_2106P18-01-005	PR_2010P20-01-008
	PR_2008P16-01-035	PR_2106P18-01-006	PR_2010P20-01-010
	PR_2008P16-01-041	PR_2106P18-01-013	PR_2010P20-01-017
	PR_2008P16-01-045	PR_2106P18-01-014	PR_2105P20-01-004

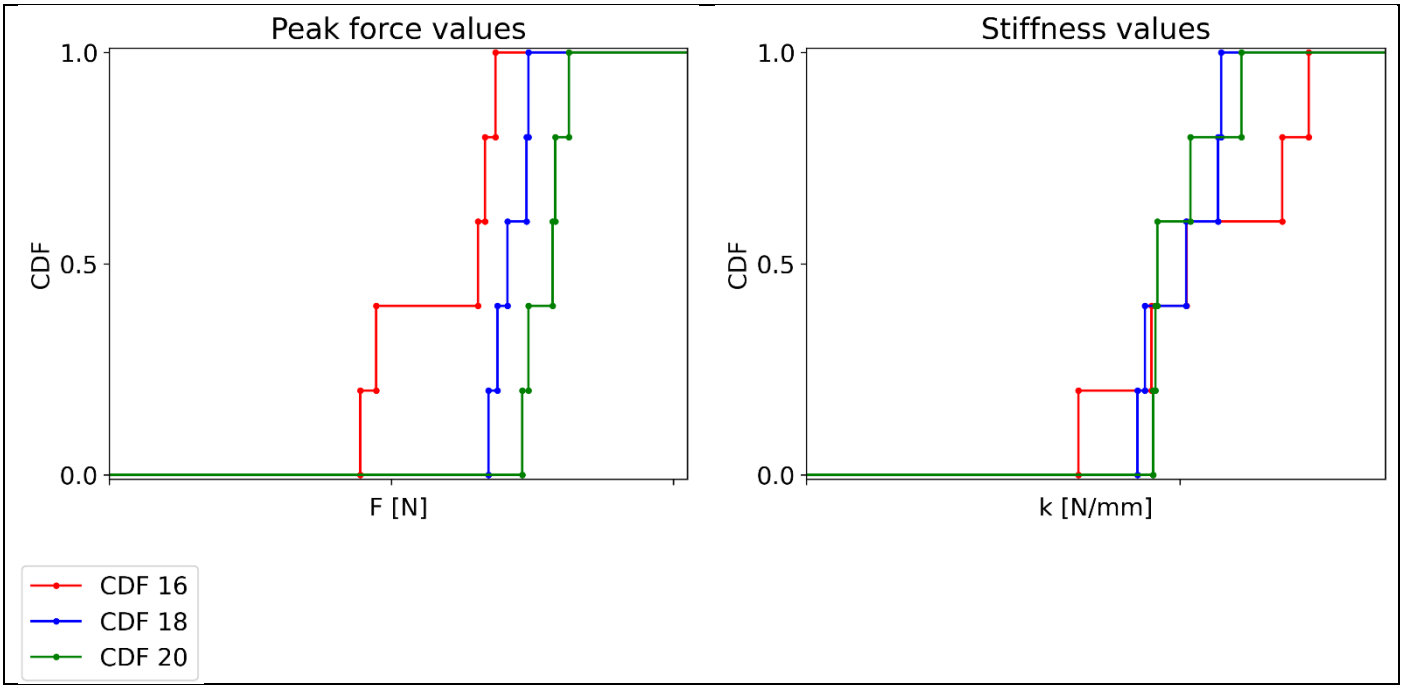

Figure 3-3: LC1, CDFs for peak force values (left) and stiffness values (right) for all XPV sizes of the experiments. The graphs with the numerical values of the peak force values and stiffness values are in Confidential Appendix D, Results and Discussion Graphs.

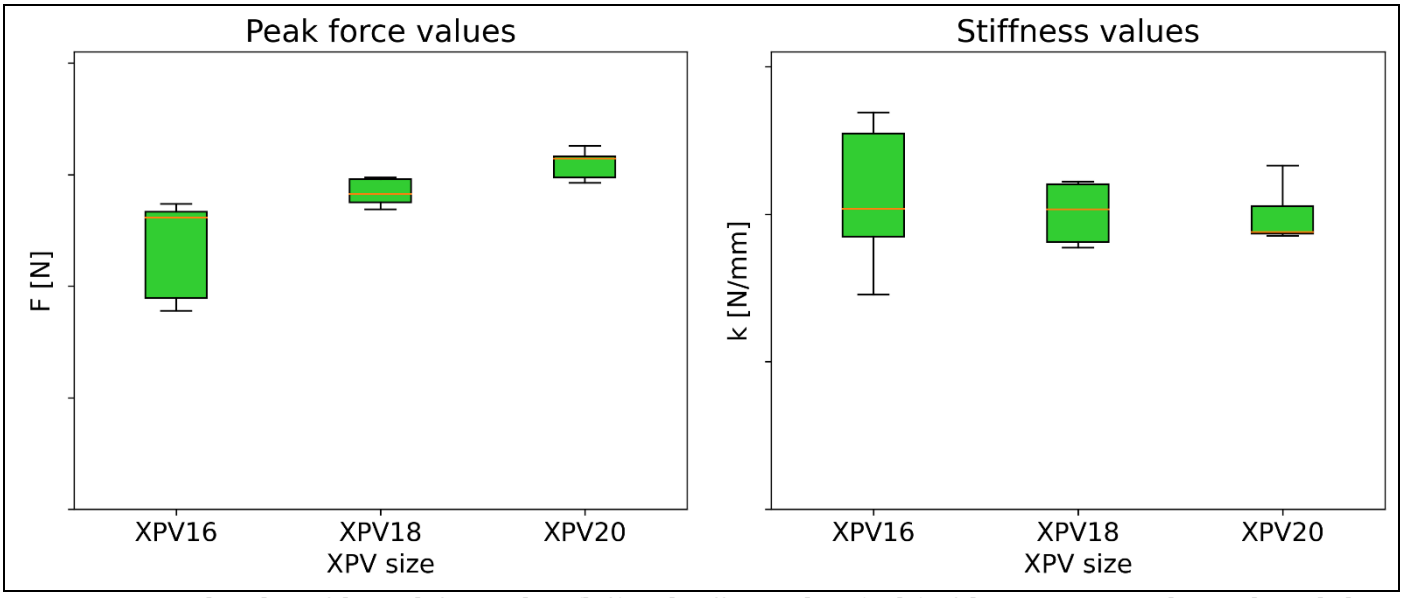

Figure 3-4: LC1, boxplots of the peak force values (left) and stiffness values (right) of the experiments. The graphs with the numerical values of the peak force values and stiffness values are in Confidential Appendix D, Results and Discussion Graphs.

3.1.2 LC2, Parallel Plate Compression

Figure 3-5 shows the force-displacement curve of one XPV20 sample during LC2. The graph with the numerical values of the force is in Confidential Appendix D, Results and Discussion Graphs. In the figure, each cycle is shown with a different color to highlight the differences between each cycle. Here the hysteresis due to viscoelasticity is visible, as the unloading is below the loading curve (20). Furthermore, plastic deformation is also visible as at zero reaction force, the displacement value increases with multiple cycles. Finally, the Mullins effect is visible as the second and third cycles are both significantly lower than the first cycle (21). This is also visible when the amount of compression increases. With increasing compression rates the difference in the first cycle and the two cycles afterwards is more notable, as can be seen from comparing cycle 7 to cycle 8 and 9. The force-displacement curves of every sample for LC1 highlighting the first half cycle, stiffness calculation region, and peak force are shown in Appendix F, LC2 Force Displacement Curves of the Experiments.

After testing a mistake was found in two tests for an XPV16 sample with serial number PP_2008P16-01-028. For the two tests done in the two different orientations 120 degrees and 240 degrees axially rotated from the starting position, the load cell failed to zero correctly. For this reason, these two tests are left out of further post-processing.

Figure 3-6 shows the first half cycle during the experiment for all samples and all cycles. The graphs with the numerical values of the force are in Confidential Appendix D, Results and Discussion Graphs. In the figure, each sample has its color in the graphs, defined in Table 3-2. From these plots, the XPV16 has the highest reaction force measured, while the XPV18 and the XPV20 are more similar. The XPV20 does have a larger range in the reaction force measured than the XPV16 and the XPV18. Furthermore, the reaction force shows small variations with the different orientations tested. Here, the reaction force trends further down for almost all samples with multiple orientations tested per sample. This could be caused by plastic deformation accumulating with each orientation tested.

Figure 3-7 shows the CDFs of the F_p values and stiffness values for all XPV sizes extracted from the force-displacement curves. The CDF plots show the probability of F_p or the stiffness of having a value less than or equal to a specific value on the horizontal axis. Figure 3-8 shows the boxplots showing the medians and distributions of the F_p values and the stiffness values for LC2 obtained from the experiments of all three sizes. The graphs with the numerical values of the F_p values and stiffness values are in Confidential Appendix D, Results and Discussion Graphs. Both the CDFs and the boxplots give information about the statistical distribution of the F_p values and the stiffness values from the experiments. From these plots, the XPV18 and the XPV20 have a similar mean F_p value with the XPV20, having a higher distribution for the F_p values. The XPV16 has the highest mean F_p value, with a small distribution. Furthermore, the stiffness values increase as the XPV size increases. The mean stiffness values between the XPV18 and the XPV20 differ slightly with the XPV18 having a higher mean stiffness value. The XPV16 has the highest mean stiffness value among the three sizes. The XPV20 has the largest distribution of stiffness values. At the higher CDF values, the curve overlaps with the XPV18 stiffness values. Thus, with this load case the reaction force and stiffness increase with smaller XPV diameters, although this increase is smaller at larger diameters. Comparing the stiffness value from the experiments with the stiffness value of the parallel plates (listed in Table 2-9), the parallel is approximately 1e8 times stiffer than the stiffness values measured in the experiments, thus the effect of the parallel plates' stiffness can be neglected.

Finally, from the boxplots, there are some outliers showing up for the F_p values and the stiffness values. For the F_p values the XPV18 has an outlier at the upper end of the F_p value distribution. This is experiment PP_2106P18-01-005 with the first orientation. The second and third orientations of experiment PP_2106P18-01-005 do fall in the whisker range of the boxplots and are not outliers. This outlier is mainly caused by the narrow F_p value distribution for the XPV18. The XPV20 also has an outlier in the lower end of the F_p value distribution. This is the experiment PP_2105P20-01-004 with the second orientation. The first and the third orientations do fall in the whisker range of the boxplots and are not outliers. When visually comparing the PP_2105P20-01-004 experiment to the other experiments, this experiment has lower F_p values than the other experiments. When looking at the serial number of the sample it is the only sample with a different starting number, indicating a different production batch. This data indicates that there is a variance between different production batches of the device. Finally, the XPV16 has an outlier in the lower end of the stiffness value distribution. This is the experiment PP_2008P16-01-045 with the third orientation.

Thus, with the help of mechanical experiments, the difference in mechanical response for the XPV16, XPV18, and XPV20 have been quantified for the parallel plate compression load case. The reaction force and the stiffness increase when the XPV size decreases from size 18 to size 16. Furthermore, the difference between the XPV18 and the XPV20 is smaller for both the reaction force and the stiffness. Finally, the XPV20 has the largest variance which could be caused by a sample from a different production batch.

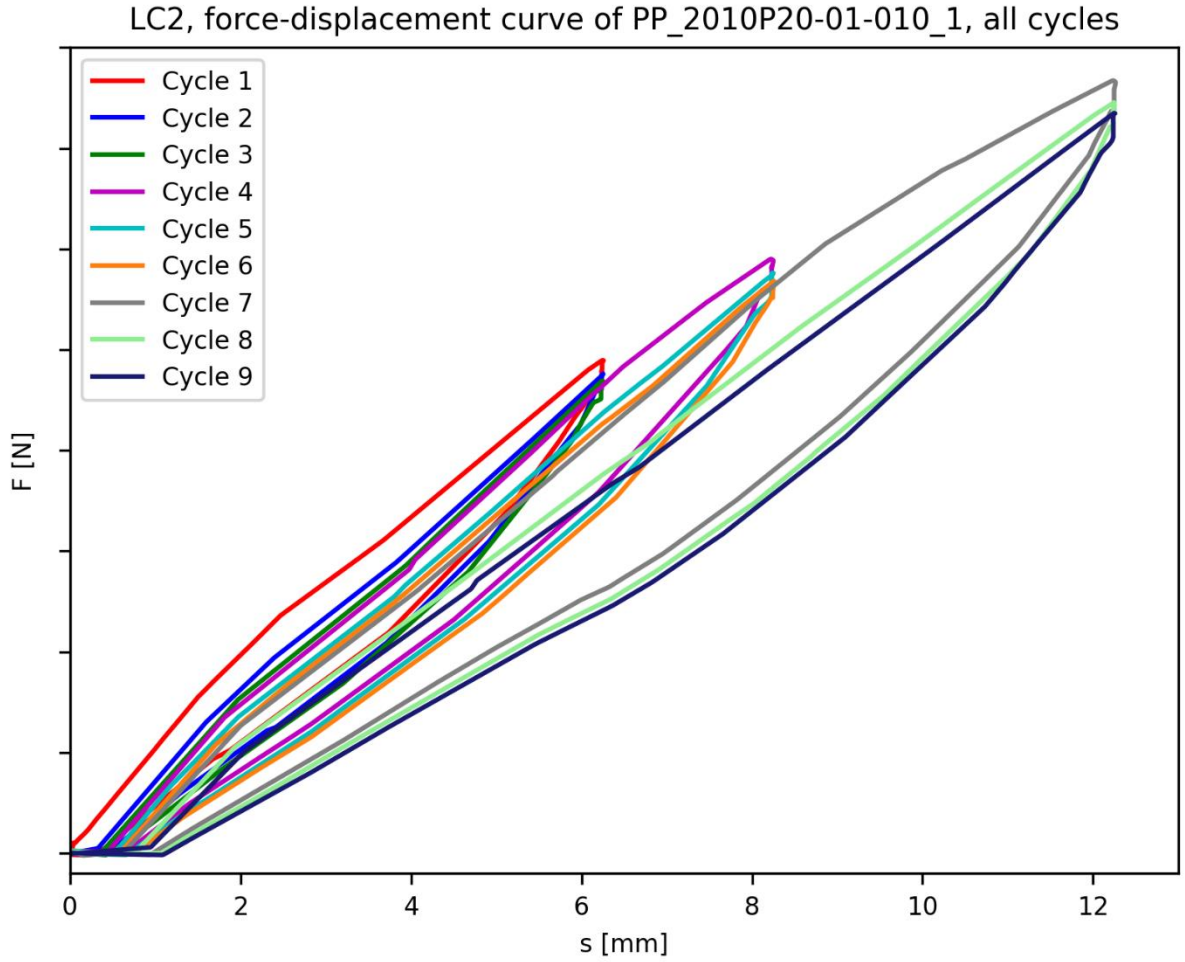

Figure 3-5: LC2, force displacement curve of an XPV20 sample, showing all cycles during one experiment. The graph with the numerical values of the force is in Confidential Appendix D, Results and Discussion Graphs.

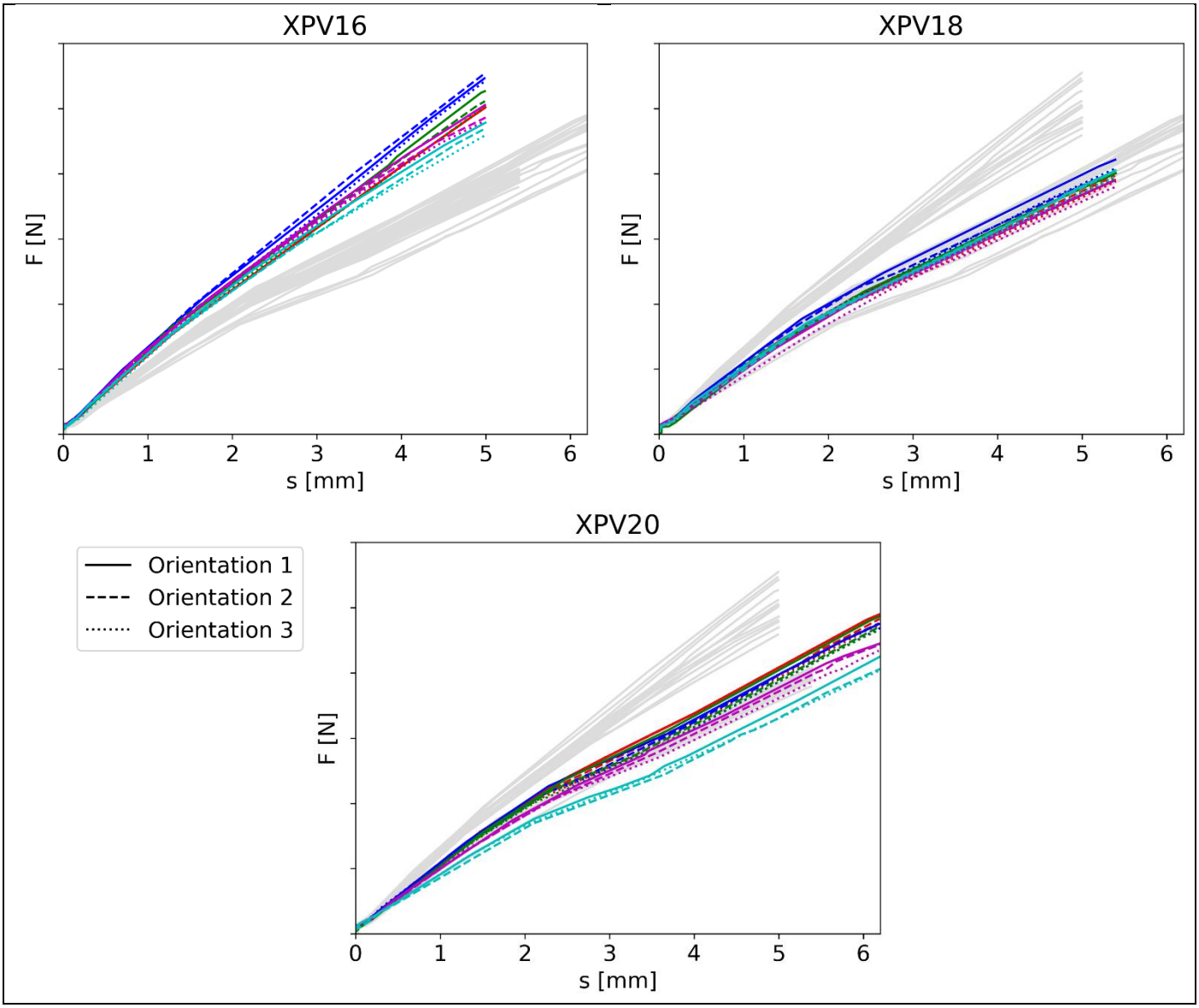

Figure 3-6: LC2, first half cycle of all samples of the XPV16 (top-left), XPV18 (top-right), and XPV20 (bottom) during the experiment. The different colors correspond to the samples tested as listed in Table 3-2. In each plot, the other XPV sizes are shown in gray for comparison. The graphs with the numerical values of the force are in Confidential Appendix D, Results and Discussion Graphs.

Table 3-2: Colors corresponding to which sample of each XPV size in Figure 3-6.

Color	XPV16 sample	XPV18 sample	XPV20 sample
	PP_2008P16-01-028	PP_2106P18-01-002	PP_2010P20-01-007
	PP_2008P16-01-030	PP_2106P18-01-005	PP_2010P20-01-008
	PP_2008P16-01-035	PP_2106P18-01-006	PP_2010P20-01-010
	PP_2008P16-01-041	PP_2106P18-01-013	PP_2010P20-01-017
	PP_2008P16-01-045	PP_2106P18-01-014	PP_2105P20-01-004

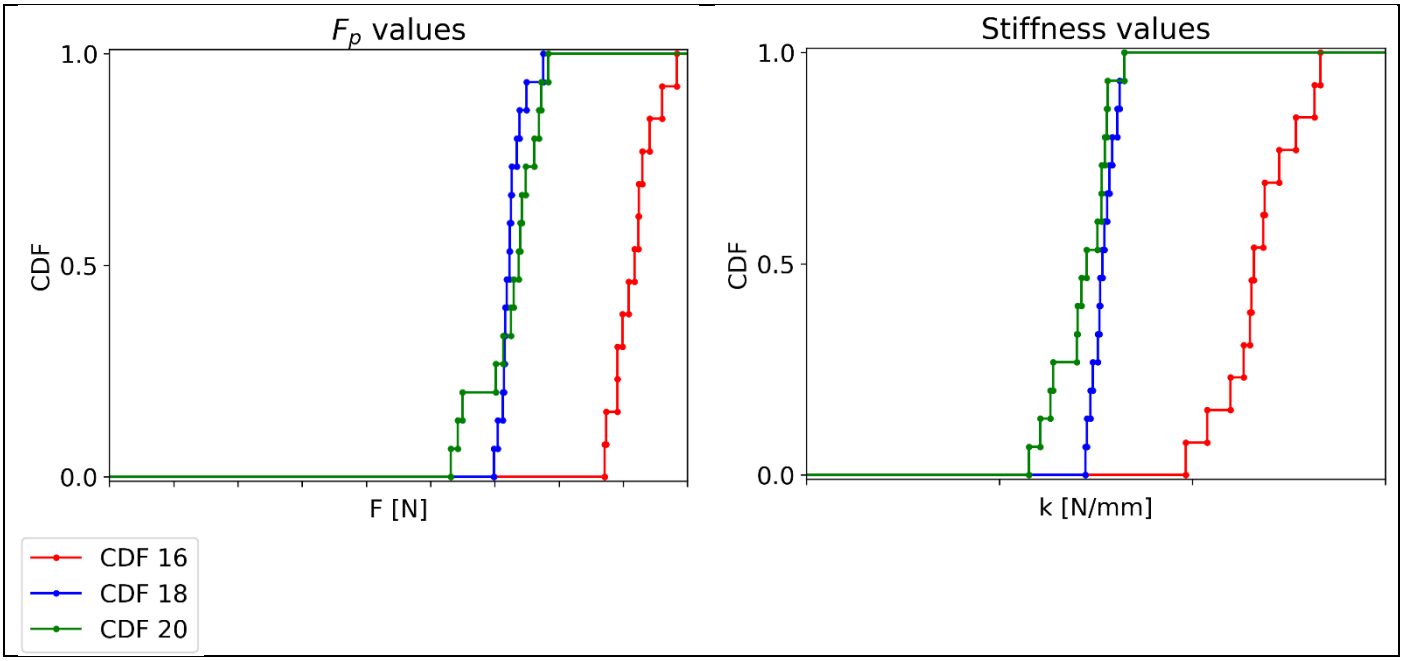

Figure 3-7: LC2, CDFs for F_p values (left) and stiffness values (right) for all XPV sizes of the experiments. The graphs with the numerical values of the F_p values and stiffness values are in Confidential Appendix D, Results and Discussion Graphs.

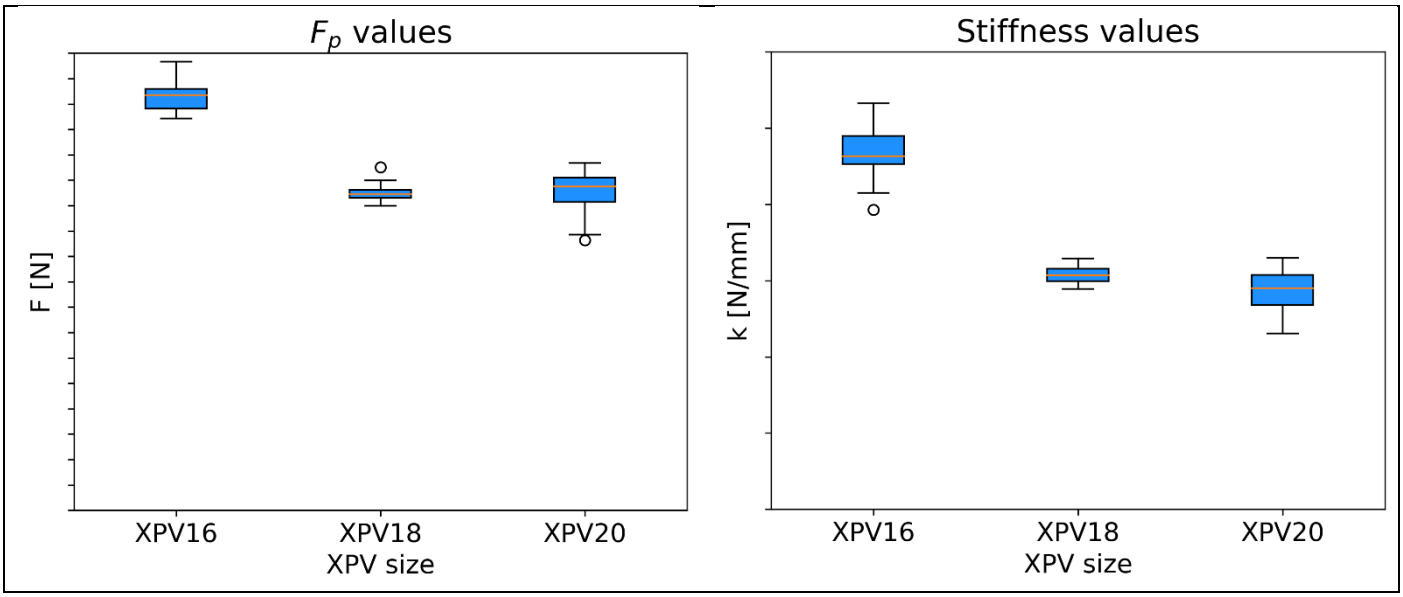

Figure 3-8: LC2, boxplots of F_p values (left) and stiffness values (right) of the experiments. The graphs with the numerical values of the F_p values and stiffness values are in Confidential Appendix D, Results and Discussion Graphs.

3.2 Simulation Results

3.2.1 LC1, Leaflet Opening Behavior

Figure 3-9 shows the boxplots showing the medians and distributions of the peak force values and the stiffness values for LC1 obtained from the simulations of all three sizes. Figure 3-10 shows the PDFs for LC1 obtained from the simulations of all three sizes. The PDFs show the probability of the peak force and the stiffness to take on a specific value. Figure 3-11 shows the CDFs of the peak force values and stiffness values for LC1 obtained from the simulations of all three sizes The graphs with the numerical values of the peak force values and stiffness values are in Confidential Appendix D, Results and Discussion Graphs. Figure 3-12 shows the input sensitivity analysis in the form of Pareto plots. The sensitivity analysis relates the influence of the input variance to the output variance, and this is shown in percentages in the plots.

From the PDFs, it can be observed that the distributions are mostly symmetrical around the mean value for all three sizes. Regarding the boxplots, they show a similar distribution for all three sizes in the case of the peak force values. In the case of stiffness distributions, however, there is a difference. Specifically, the variance for the XPV20 size is less than the XPV16 and XPV18. This suggests that larger XPV sizes have less variance in stiffness for this load case.

Moving to the mean peak force values, the XPV18 has a higher mean peak force value than the XPV16 and the XPV20. This can be explained by the sensitivity analysis outcome. For the peak force values, the XPV18 has a higher positive sensitivity to the stiffness in the Leaflet material fiber direction. Although this material stiffness is the same for all three XPV sizes, an increase in sensitivity means an increase in peak force values. Thus, the mean peak force values are in line with the sensitivity analysis performed.

Regarding the mean stiffness values, the higher mean stiffness value of the XPV20 indicates that larger XPV sizes are stiffer for this load case. Although, the mean stiffness value of the XPV16 is higher than the XPV18. This difference can be explained by the sensitivity analysis. The Pushrod y-offset only influences the XPV16 and not the other two XPV sizes. Furthermore, the XPV16 has a higher positive sensitivity to the stiffness in the Leaflet material fiber direction than the XPV18 and XPV20. This combined with the higher negative sensitivity to the Leaflet trim angle for the XPV18 causes the mean stiffness value of the XPV16 to be higher than the XPV18.

Looking into the sensitivity analysis in more detail, the Leaflet trimming parameters have the most effect on the peak force values for all XPV sizes. Here, the Leaflet trim angle has a negative sensitivity of 17%, 23%, and 16% for the XPV16, XPV18, and XPV20 respectively. The Leaflet trim length has a positive sensitivity of 13%, 11%, and 12% for the XPV16, XPV18, and XPV20 respectively. The stiffness in the Leaflet material fiber direction also has a significant effect on the peak force values, especially for the XPV18. Here the stiffness in the Leaflet material fiber direction has a positive sensitivity of 12%, 23%, and 11% for the XPV16, XPV18, and XPV20 respectively.

Regarding the sensitivity analysis for the stiffness values, the Leaflet trim angle has the most effect on the stiffness values for the XPV18. Here the Leaflet trim angle has a negative sensitivity of 9%, 21%, and 13% for the XPV16, XPV18, and XPV20 respectively. The stiffness in the Leaflet material fiber direction also has a significant effect on the stiffness values, especially for the XPV16. Here the stiffness in the Leaflet material fiber direction has a positive sensitivity of 12%, 7%, and 6% for the XPV16, XPV18, and XPV20 respectively. Finally, the Pushrod y-offset also has a significant effect on the stiffness values. Here, the Pushrod y-offset has a sensitivity of 10%, 7%, and 11% for the XPV16, XPV18, and XPV20 respectively. The Pushrod y-offset sensitivity for the XPV20 is negative, while the sensitivity for the XPV16 and XPV18 is positive.

With the help of the distributions and sensitivity analysis, capable through the FE simulations, meta modeling, and Monte Carlo simulations the mechanical response of the XPV16, XPV18, and XPV20 have been captured. According to the FE simulations, the XPV18 has a larger peak force than the XPV16 and the XPV20. The difference in peak force is smaller for the XPV16 and the XPV20. Furthermore, the XPV20 has a higher stiffness than the XPV16 and the XPV18. The difference in stiffness is smaller for the XPV16 and the XPV20.

Finally, variables have been identified that significantly influence the reaction force and the stiffness for the Leaflet opening behavior load case (LC1). Regarding the peak force values, the stiffness in the Leaflet material fiber direction, the Leaflet trim angle, and the Leaflet trim length have a significant influence, all having a sensitivity higher than 10% for all XPV sizes. Regarding the stiffness values, the stiffness in the Leaflet material fiber direction and the Pushrod y-offset have a significant influence on the XPV16 having a sensitivity of 10% or higher. Furthermore, the Leaflet trim angle significantly influences the stiffness values of the XPV18, having a sensitivity higher than 20%. Finally, the Leaflet trim angle and the Pushrod y-offset significantly influence the stiffness values of the XPV20, having a sensitivity higher than 10%.

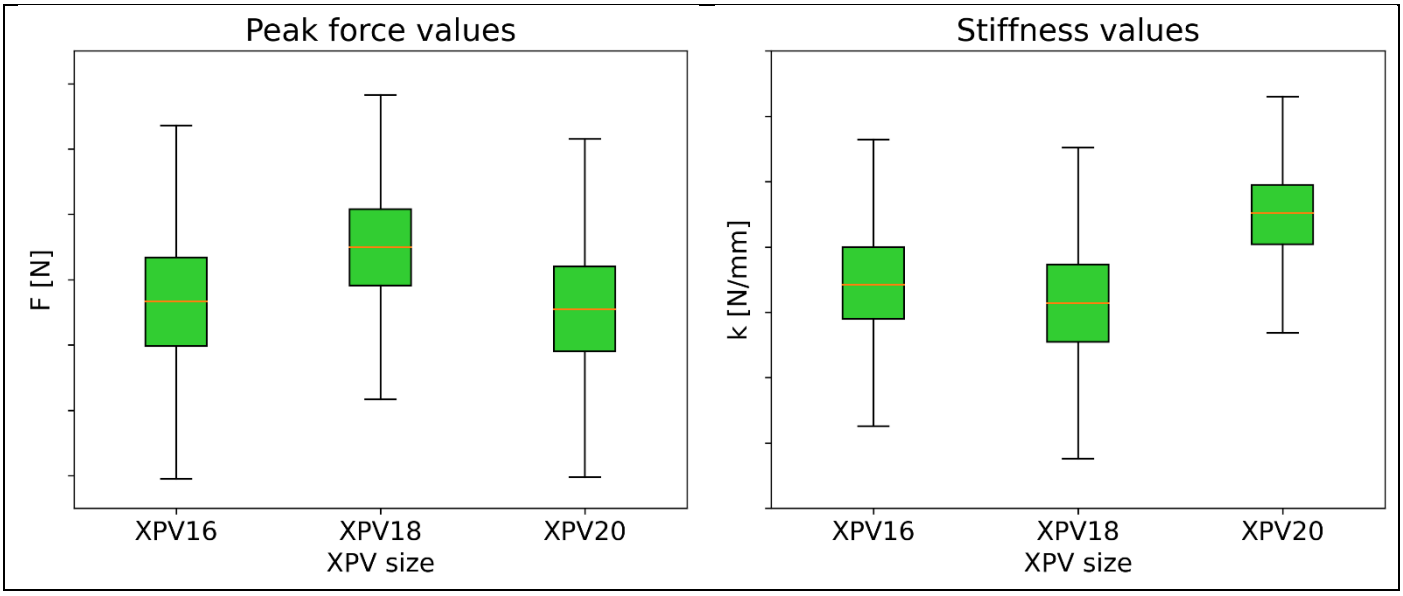

Figure 3-9: LC1, boxplots for peak force values (left) and stiffness values (right) for all XPV sizes of the simulations. The graphs with the numerical values of the peak force values and stiffness values are in Confidential Appendix D, Results and Discussion Graphs.

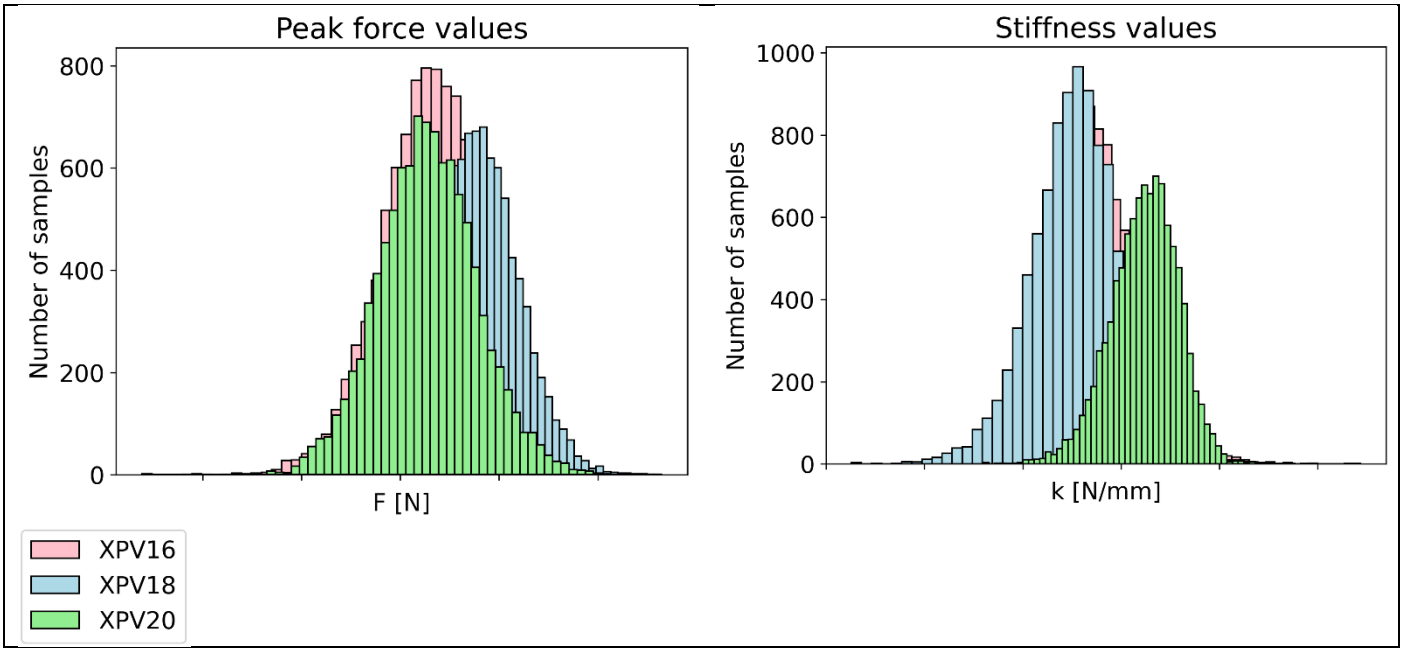

Figure 3-10: LC1, PDFs for peak force values (left) and stiffness values (right) for all XPV sizes for the simulations. The graphs with the numerical values of the peak force values and stiffness values are in Confidential Appendix D, Results and Discussion Graphs.

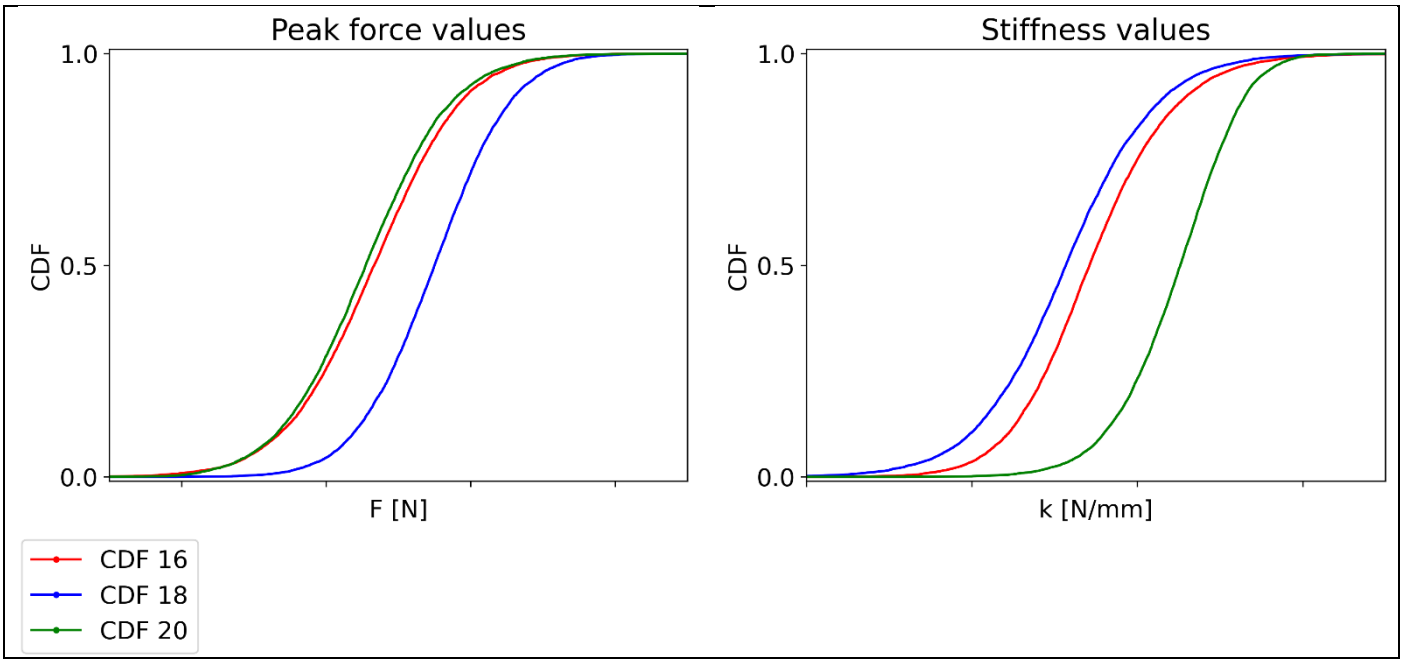

Figure 3-11: LC1, CDFs for peak force values (left) and stiffness values (right) for all XPV sizes of the simulations. The graphs with the numerical values of the peak force values and stiffness values are in Confidential Appendix D, Results and Discussion Graphs.

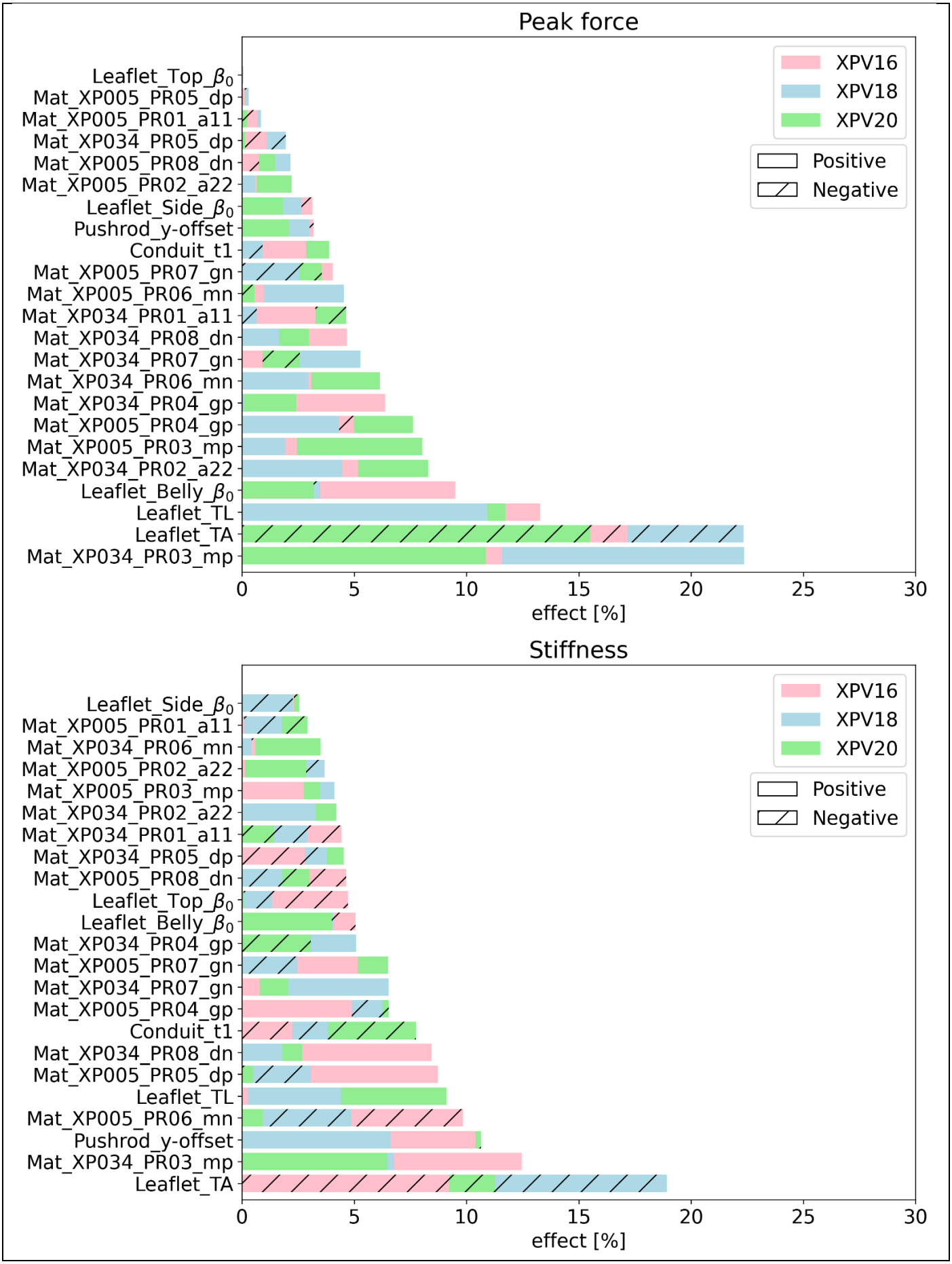

Figure 3-12: LC1, input parameters sensitivity analysis for the peak force (top) and stiffness (bottom) output values of all XPV sizes. The dashed bars mean the parameters have a negative effect on the output.

3.2.2 LC2, PARALLEL PLATE COMPRESSION

Figure 3-13 shows the boxplots showing the medians and distributions of the F_p values and the stiffness values for LC2 obtained from the simulations of all three sizes. Figure 3-14 shows the PDFs showing the probability the F_p and the stiffness take on a specific value for LC2 obtained from the simulations of all three sizes. Figure 3-15 shows the CDFs of the F_p values and stiffness values for LC1 obtained from the simulations of all three sizes. The graphs with the numerical values of the F_p values and stiffness values are in Confidential Appendix D, Results and Discussion Graphs. Figure 3-16 shows the input sensitivity analysis in the form of Pareto plots. The sensitivity analysis relates the influence of the input variance to the output variance, and this is shown in the plots in percentages.

From the PDFs, it can be observed that the distributions are mostly symmetrical around the mean value for all three sizes. Regarding the boxplots, they show a similar distribution for all three sizes in the case of the F_p values and stiffness values. However, the mean F_p value for the XPV20 is smaller than the mean F_p value of the other two sizes. When looking at the sensitivity analysis, the output parameters are mostly influenced by the undamaged anisotropy material parameters. As these parameters don't change across the device sizes, the output values don't change because of this. The observed change in the mean peak force value for the XPV20 thus suggests that the F_p value decreases when the XPV diameter decreases. However, the change in mean F_p value from the XPV16 to the XPV18 is very small, indicating that only with larger diameters this change in F_p is notable.

Looking into the sensitivity analysis in more detail, the material parameters for undamaged anisotropy have the most effect on the F_p values for all XPV sizes. For the F_p values, the stiffness in the Conduit material fiber direction has a positive sensitivity of 28%, 29%, and 25% for the XPV16, XPV18, and XPV20 respectively. Furthermore, the measure of Conduit material fiber direction along the circumferential direction has a positive sensitivity of 13% for the XPV16 and XPV18, and 11% for the XPV20. Finally, the stiffness in the Leaflet material fiber direction has a positive sensitivity of 10% for the XPV16 and XPV20 and 9% for the XPV18.

Regarding the sensitivity analysis for the stiffness values, the same material parameters for undamaged anisotropy have the most effect on the stiffness values of all XPV sizes. The stiffness in the Conduit material fiber direction has a positive sensitivity of 24%, 25%, and 21% for the XPV16, XPV18, and XPV20 respectively. Furthermore, the measure of Conduit material fiber direction along the circumferential direction has a positive sensitivity of 13%, 12%, and 11% for the XPV16, XPV18, and XPV20 respectively. Finally, the stiffness in the Leaflet material fiber direction has a positive sensitivity of 7%, 12%, and 11% for the XPV16, XPV18, and XPV20 respectively.

With the help of the distributions and sensitivity analysis, capable through the FE simulations, meta modeling, and Monte Carlo simulations the mechanical response of the XPV16, XPV18, and XPV20 have been captured. According to the FE simulations, the XPV20 has a smaller F_p than the XPV16 and the XPV18. The difference in F_p is smaller for the XPV16 and the XPV18. Furthermore, the stiffness is similar for the XPV16, XPV18 and XPV20.

Finally, variables have been identified that significantly influence the reaction force and the stiffness for the parallel plate compression load case (LC2). Regarding the F_p values, the stiffness in the Conduit material fiber direction and the measure of Conduit material fiber direction along the circumferential direction have a significant influence, all having a sensitivity higher than 10% for all XPV sizes. Furthermore, the stiffness in the Leaflet material fiber direction significantly influences the F_p values of the XPV16 and XPV20, having a sensitivity of 10%. Regarding the stiffness values, the stiffness in the Conduit material fiber direction and the measure of Conduit material fiber direction along the circumferential direction have a significant influence, all having a sensitivity higher than 10% for all XPV sizes. Furthermore, the stiffness in the Leaflet material fiber direction significantly influences the stiffness values of the XPV18 and XPV20, having a sensitivity higher than 10%.

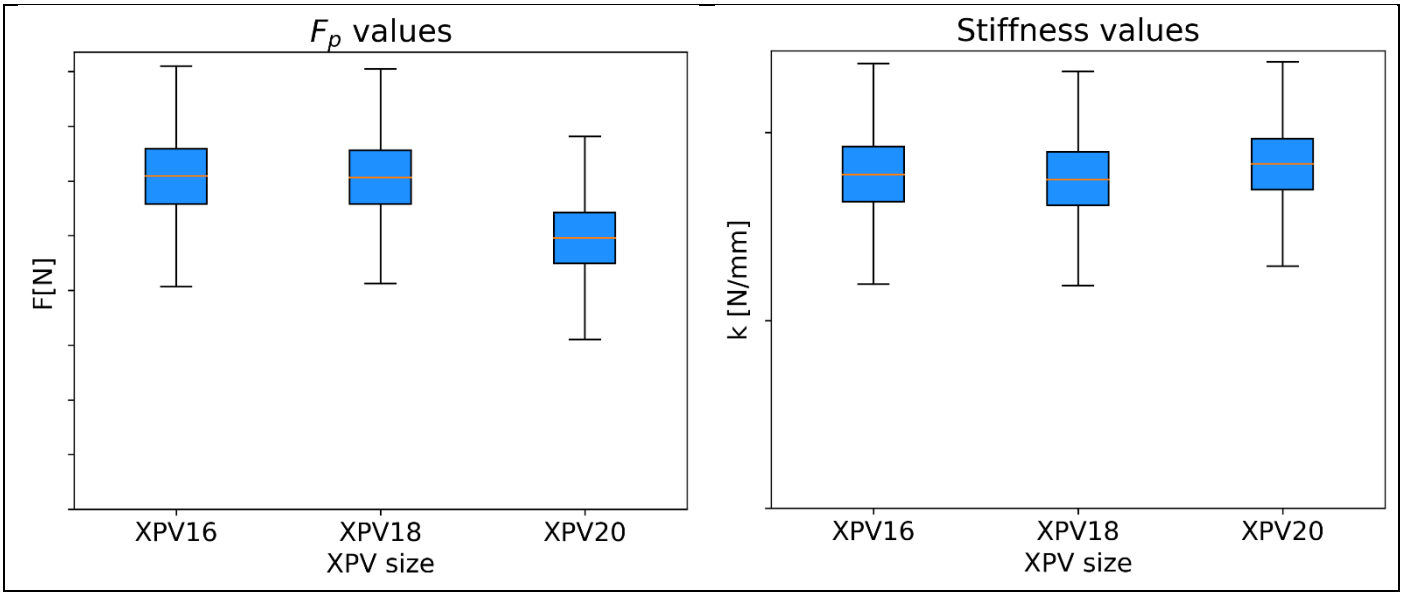

Figure 3-13: LC2, boxplots for F_p values (left) and stiffness values (right) for all XPV sizes of the simulations. The graphs with the numerical values of the F_p values and stiffness values are in Confidential Appendix D, Results and Discussion Graphs.

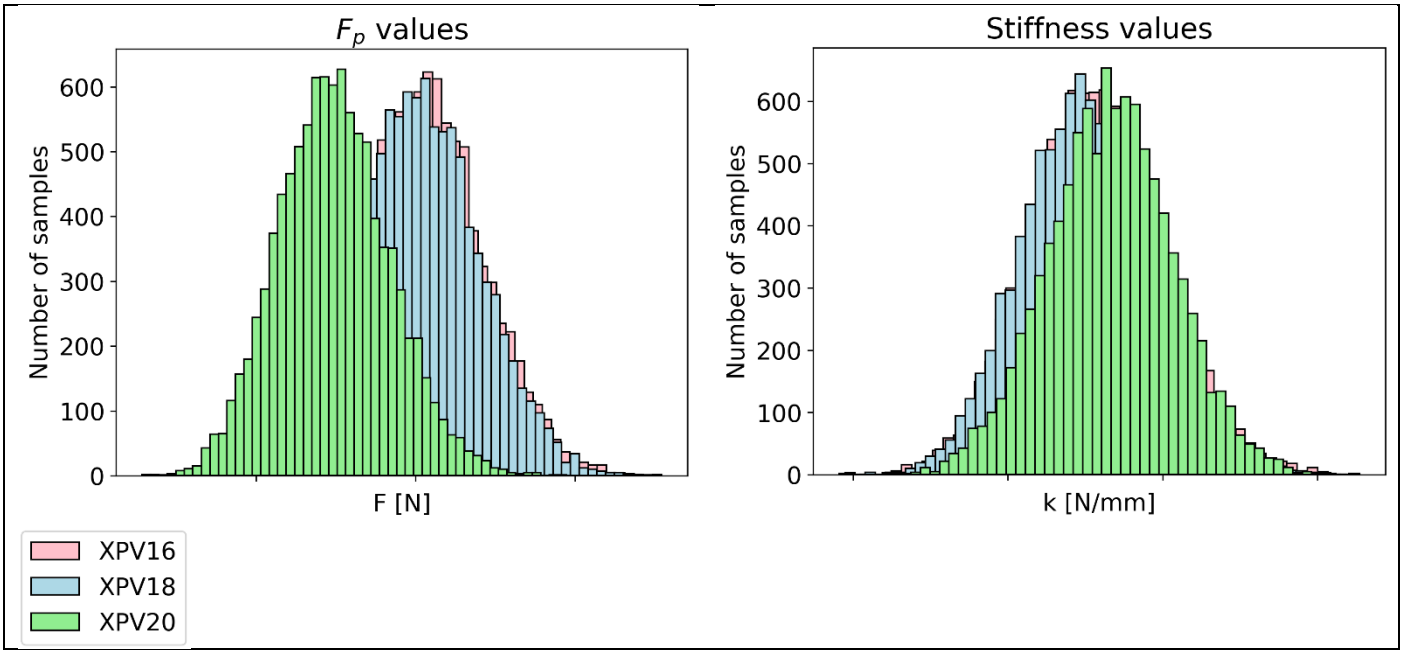

Figure 3-14: LC2, PDFs for F_p values (left) and stiffness values (right) for all XPV sizes for the simulations. The graphs with the numerical values of the F_p values and stiffness values are in Confidential Appendix D, Results and Discussion Graphs.

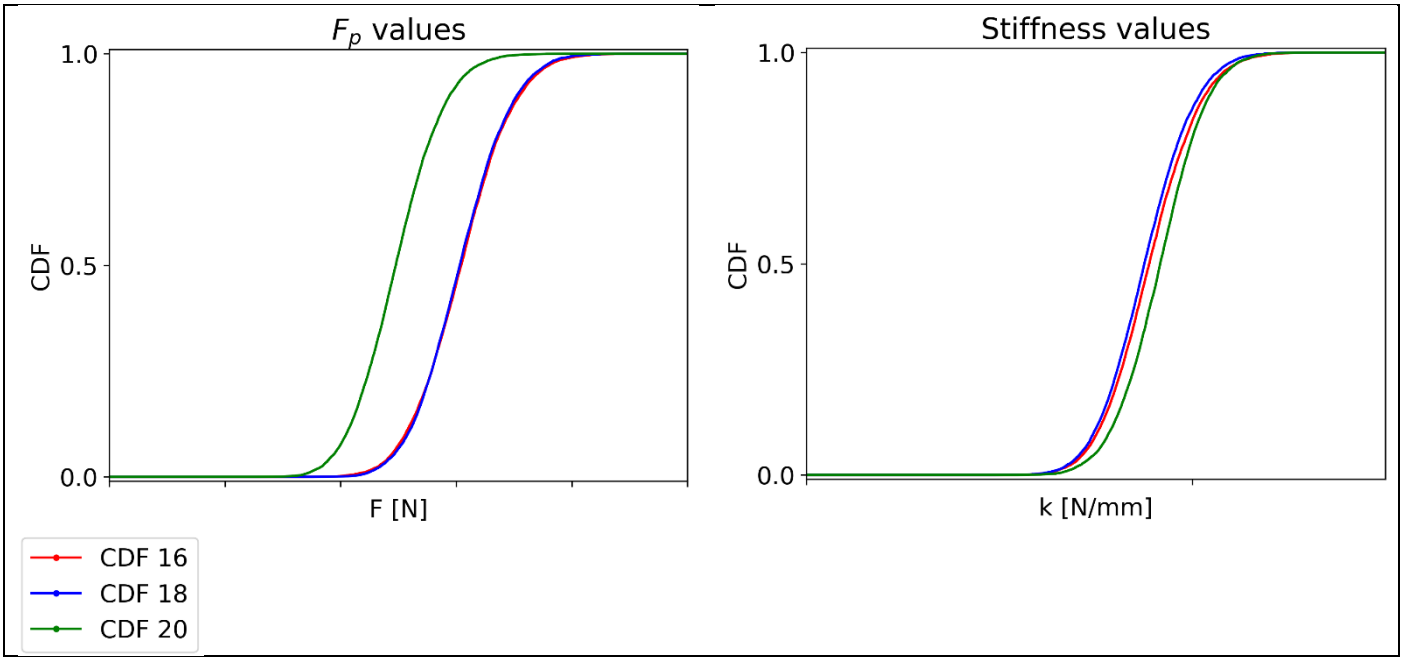

Figure 3-15: LC2, CDFs for F_p values (left) and stiffness values (right) for all XPV sizes of the simulations. The graphs with the numerical values of the F_p values and stiffness values are in Confidential Appendix D, Results and Discussion Graphs.

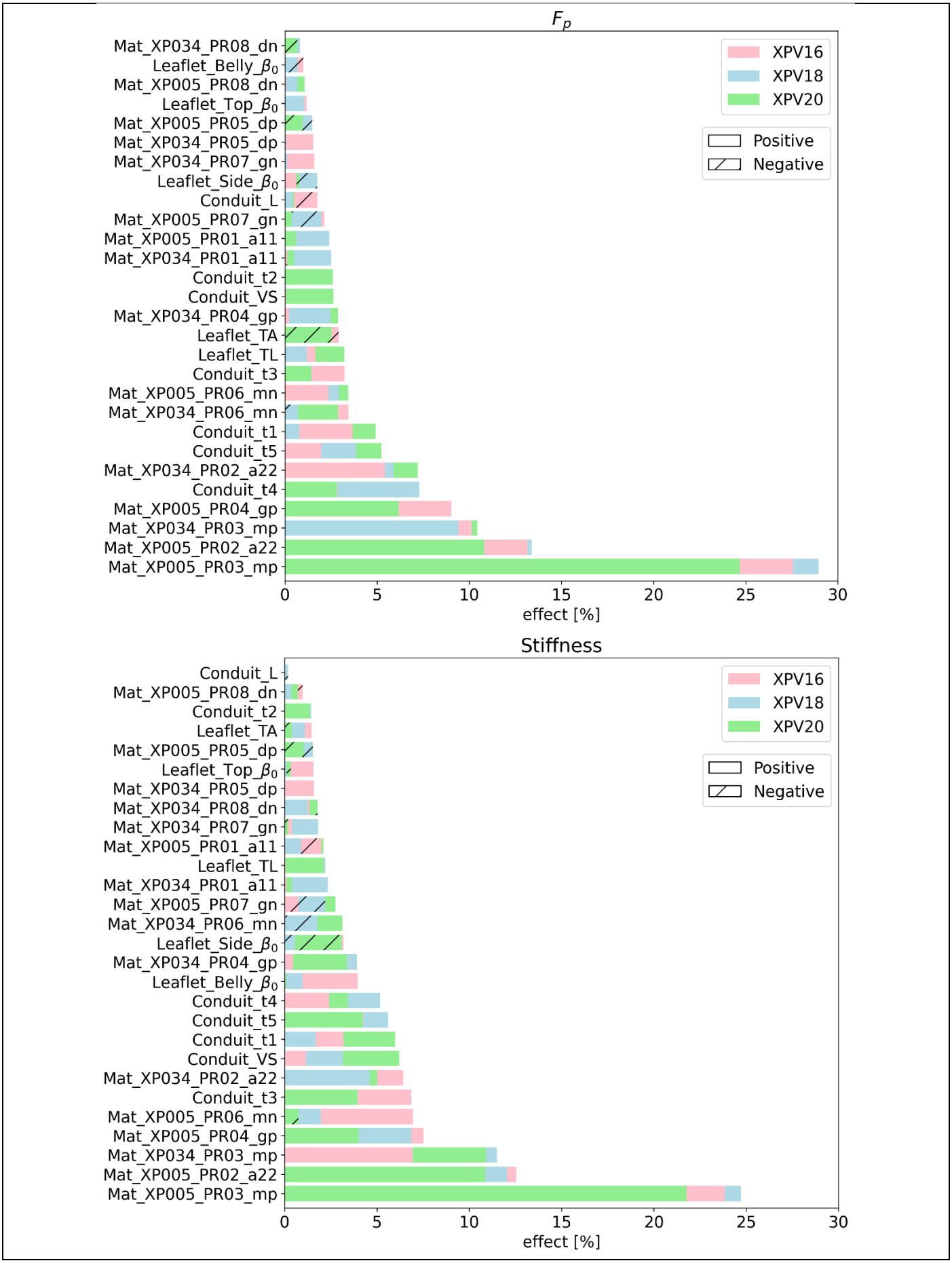

Figure 3-16: LC2, input parameters sensitivity analysis on the F_p (top) and stiffness (bottom) output values of all XPV sizes. The dashed bars mean the parameters have a negative effect on the output.

3.3 Model Assessment

3.3.1 Validation Metric

Now that both the simulations and the experiments have been performed, the capability of the FE model to predict the outcome of the experiments will be assessed by comparing the simulation results with the experiment results, this is also called model validation. The goal of validation is to quantify the correctness of the computational model by comparing the output of the simulations with reality. This comparison is done by developing a validation comparator or validation experiment, which provides comparative data for validating the computational model. According to the ASME V&V, 40-2018 standard 'Assessing Credibility of Computational Modeling Through Verification and Validation: Application to Medical Devices', two validation metrics are used to establish model credibility. The first metric is the difference between the simulation and the comparator outputs. The second metric is the uncertainty quantification in this comparison (7).

The first validation metric can be defined by looking at the performance metrics used to evaluate in vitro tests of prosthetic heart valves. These metrics are the effective orifice area (EOA) and the amount of paravalvular regurgitation according to the ISO 5840-1 'Cardiovascular implants – Cardiac valve prostheses – General requirements' (14). Other possible metrics for measuring valve performance include geometric orifice area (GOA), opening velocity (OV), slow closing velocity (CVs), rapid closing velocity (CVr), maximum von Mises stress during systole (VMSsys), maximum von Mises stress during diastole (VMSdia), regurgitant orifice area (ROA), coaptation surface area (CSA), maximum von Mises stress of Leaflet 1 during diastole (VMS1), maximum von Mises stress of Leaflet 2 during diastole (VMS2) and maximum von Mises stress of Leaflet 3 during diastole (VMS3) (27). The EOA and CSA are schematically shown in Figure 3-17.

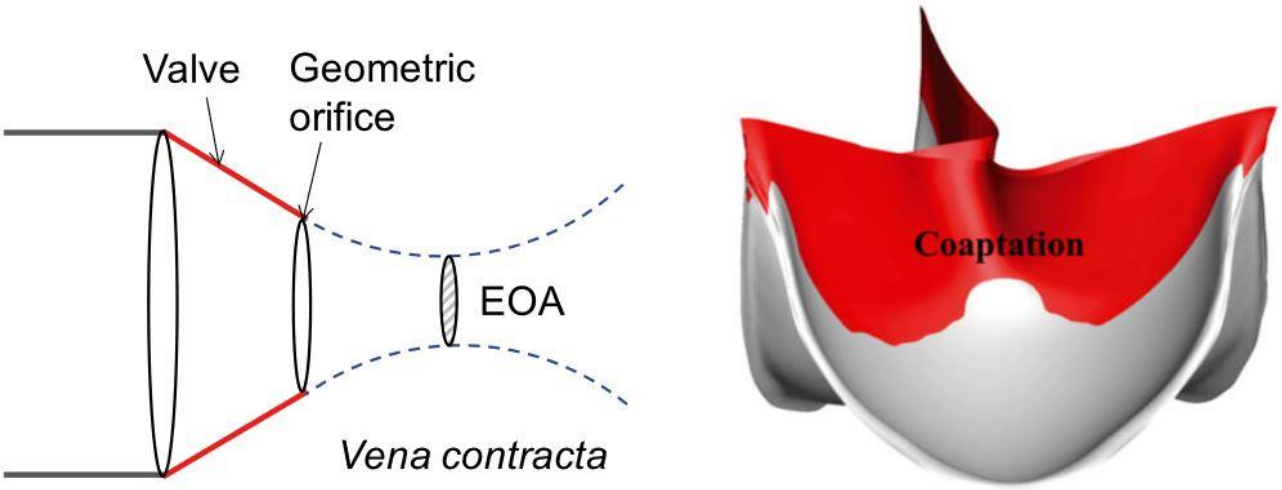

Figure 3-17: The EOA (left) is a metric describing the flow through the valve during systole. A small EOA means something is blocking the opening of the valve. The CSA (right) is a metric describing the seal of the valve during diastole. A small CSA means some leakage occurs (13).

Multiple studies have performed different validation strategies to validate their computational model. Often the validation is done by comparing the simulation results with a performed in vitro test. For these comparisons, different metrics have been used.

Computational models of a porcine aortic prosthetic heart valve and a bovine aortic prosthetic heart valve have been validated by comparing the simulation results to in vitro experiments from two pulse duplicators used to evaluate prosthetic heart valves. The flow rate, upstream pressure, downward pressure, and Leaflet kinematics were measured in the experiment. The metrics used were the mean stroke volume, maximum pressure difference during forward flow, GOA, valve opening time, valve closing time, valve open area fluttering frequencies, and symmetry behavior. Also, the flow patterns in the simulations and the experiments were qualitatively compared (8).

Another study validated their model by putting the modeled valve in a pulse duplicator machine. Using the machine, a cardiac output of 4.5 l/min was simulated. Three deformation metrics were used to quantitatively validate the simulation results. The metrics were the distances between the center of the valve and the point of the tip of the edges of the Leaflets, measured at six-time points in the simulation and the experiment. Furthermore, the GOA was taken at peak systole as another comparative metric (9).

Another study validated their model by measuring the deformation of two bovine pericardium heart valves during three quasi-static paravalvular closing pressures. The deformation was measured by tracking 60 black dots of a diameter between 0.2 and 0.4 mm applied on each Leaflet of the valve with two borescopes. From the measurements, the strain was calculated and compared with the simulation (10).

Another study validated their model by comparing the flow profiles of an in vitro experiment with a pulse duplicator replicating a heart cycle. The flow profiles were measured with a 2D particle image velocimetry (PIV) and captured at specific instants during the systolic cycle. The results of the flow profiles were used to qualitatively compare the simulation with the experiment. Furthermore, the evolution of the velocity with respect to time across the whole domain, the valve EOA, and the downstream velocities across the root diameters at the aortic side were used for quantitative comparison. For the velocity metrics, the standard deviation of the experiments was used in the assessment (11).

Although the above-described methods of validation prove that computational models can be developed to show good agreement with the experiments, the computational models described here are not validated to predict the outcome of an experiment. These computational simulations were done to accurately simulate the in vitro test by using the measured output from the in vitro test as an input for the computational model. Therefore, the computational model has been validated for one specific case and no conclusion can be drawn about the accuracy of the computational model in other cases, such as when the in vitro test is performed slightly differently.

Computational predictive modeling is possible as proven by a study that compared the outcomes of a computational model of TAVI performance with post-TAVI in vivo measurements. The TAV position in the computational model was based on pre-procedural planning. Thus, simulations didn't use post-TAVI data to drive the simulations. The in vivo measurements were done with CT and transesophageal echocardiography (TEE) of nine patients with stenotic bicuspid aortic valves. The models were all developed with the pre-TAVI patient-specific geometry of the patient in question. The eccentricity, expansion, and paravalvular leakage were used as comparator metrics. The paravalvular leakage was measured over one heart cycle. The comparison with the simulation and the in vivo measurements was done with a t-test. Results from the study showed that the simulations were in good agreement with the CT and TEE measurements done. Thus, showing the possible predictive capabilities of computational device modeling (12).

Thus, multiple studies have been done that compared the result of a simulation to an in vitro test or in vivo data using a multitude of metrics. Although none have incorporated thorough uncertainty quantification analyses where the uncertainty of the computational model and the comparator are investigated. Uncertainty quantification can provide insight into how sensitive the computational model and the experiment are to specific uncertainties [7].

In this study, uncertainty quantification has been incorporated by developing a meta-model to perform a Monte Carlo simulation. This created a distribution of computational outputs from distributions of multiple inputs. Furthermore, experiments have been done for multiple samples per size, creating a distribution of results per size and experiment. The CDFs of the output parameters of the simulations and the experiments were calculated. The metric that was chosen to compare the simulation CDFs to the experiment CDFs is a metric from ASME V&V 10 'Standard for Verification and Validation in Computational Solid Mechanics' called the area metric, see Formula 3.1. The area metric is defined as the area between the simulation CDF and the experimental CDF, normalized by the absolute mean of the experimental outputs. In the ideal case, the simulations are identical to the experiments, the CDFs overlap, and the area metric is zero. The area metric is the probabilistic relative error of the simulation CDF compared to the experiment CDF (28). Using the area metric, the accuracy of the model is defined as the inverse of the area metric.

$$M = \frac{\int_{-\infty}^{\infty} |F_{X,comp}(x) - F_{X,exp}(x)| dx}{|\bar{x}_{exp}|} \qquad (3.1)$$

3.3.2 LC1, LEAFLET OPENING BEHAVIOR

In Figure 3-18 the boxplots of the experiments and the simulations are shown to compare the distributions. Furthermore, the CDFs of the experiments and the simulations have been combined for the peak force values and the stiffness values for all XPV sizes. The area between the experiments CDF and simulations CDF has been used to calculate the area metric for all cases. The different CDFs for both the experiments and the simulations, highlighting the area between the CDFs, and showing the value of the area metric for this load case are shown in Figure 3-19. The graphs with the numerical values of the peak force values and stiffness values are in Confidential Appendix D, Results and Discussion Graphs. From the area metric, the relative error was obtained to compare the distribution of the simulation results to the distribution of the experiment results. Furthermore, the accuracy of the FE model has been calculated by taking the inverse of the area metric, which is listed in Table 3-3. From here, the XPV16 shows the best agreement regarding the peak force with the smallest relative error of 24.3%. The XPV18 and XPV20 are not far from the XPV16 with a 5% and a 2.6% higher relative error for the XPV18 and the XPV20 respectively. Regarding the relative error for the stiffness, the XPV20 has the smallest relative error of 31.7%. The XPV16 is not far from this with a 3% higher relative error. The XPV18 has a significantly higher relative error with an increase of 18% compared to the XPV20.

Table 3-3: LC1, peak force values, and stiffness values relative error comparing the simulations with the experiment using the area metric parameter from Formula 3.1.

	Relative error based on the area metric		FE model accuracy	
Device size	Peak force	Stiffness	Peak force	Stiffness
XPV16	24.3%	34.7%	75.7%	65.3%
XPV18	29.3%	49.7%	70.7%	50.3%
XPV20	26.9%	31.7%	73.1%	68.3%

The area metric gives an impression of the overall accuracy of the model, including the uncertainty quantification that has been implemented for both the simulations and the experiments. Comparing the means of the CDFs gives an impression on the accuracy of the model excluding parts of the distribution of the results. This gives insight into the accuracy of the UQ and specifically, the bounds defined for the Monte Carlo simulation. This is listed in Table 3-4. Here, the relative error is smaller for all cases and follows the same trend across the three device sizes. The XPV16 has the best agreement regarding the peak force with a relative error of 13.4%. The increase in relative error for the XPV18 and XPV20 is higher however, with a 9.6% and a 13.9% higher relative error for the XPV18 and XPV20 respectively.

Regarding the relative error for the stiffness, the XPV20 has the smallest relative error of 23.9%. Here the increase in relative error is also larger than the increase in relative error based on the area metric. The XPV16 is not far from this with a 3% higher relative error. The increase in relative error is 6.5% and 19.2% for the XPV16 and the XPV18 respectively.

Table 3-4: LC1, peak force values and stiffness values relative error comparing the simulations with the experiments using the mean values of both distributions.

	Relative error based on the mean values	
Device size	Peak force	Stiffness
XPV16	13.4%	30.4%
XPV18	23.0%	43.1%
XPV20	27.3%	23.9%

The relative error based on the area metric is larger than the relative error based on the mean values. This indicates that the distribution of the simulations is larger than the distribution of the experiments. This is also clear from the boxplots as the boxplots from the simulations show a wider distribution than the boxplots from the experiments. This can have two causes, either the simulations overestimate the uncertainty in the experiments, or the experiments don't cover the full range of XPV device variations.

If the simulations overestimate the distributions of the experiments, it is likely due to the distributions applied to the materials. These distributions are derived from test data done with different samples. The distributions for the geometrical parameters and the Pushrod position parameters are more likely to be in the right bounds. This is because the distributions for the geometrical parameters are derived from μCT data from the tested samples. Furthermore, the distributions for the Pushrod position are derived from video measurements done after the tests. Thus, both the geometrical parameters and the Pushrod position parameters are derived from data that have a direct link to the experiments. However, the material parameters are derived from a different dataset, which can cause the difference in distributions seen in the boxplots. The applied distributions for the material parameters are likely larger than the differences in material properties between the samples from the experiments. A better estimate of the material distribution, which is calibrated to the expected material distribution of the samples in the experiments, can reduce the relative error based on the area metric.

If the experiments don't cover the full range of the XPV device variations, this can be caused by the samples from the experiments being from the same production batch. From Table 3-1, the first 8 numbers for the XPV16, XPV18, and XPV20 are the same for all samples indicating they are indeed from the same production batch, except one XPV20 sample. This XPV20 sample from another production batch does not show significantly different results from the other samples. However, one sample from another production batch doesn't provide sufficient data to rule out there are no differences between production batches. Thus, testing with samples from different production batches should be done to investigate the variation between production batches. When more testing is done with more product batches a better approximation of the total range of device variations can be made which improves the comparative quality of the experiments.

Both arguments described above will improve the quality of the model and the experiment by modifying the distribution of both. However, this doesn't explain the difference in mean values observed for the peak force values and the stiffness values. The relative error based on the mean values indicates a systematic difference between the experiments and the simulations. This can be improved by a better estimation of the input parameters that have a high sensitivity for the peak force values and the stiffness values (see Figure 3-12). Thus, the relative error for the peak force values can be reduced by a better estimation of the stiffness in the Leaflet material fiber direction, Leaflet trim angle, and Leaflet trim length. Furthermore, the relative error for the stiffness values can be reduced by a better estimation of the Leaflet trim angle, the stiffness in the Leaflet material fiber direction, and the Pushrod y-offset.

Thus, with the area metric the accuracy of the predictive FE model simulating the mechanical responses observed in the mechanical tests has been quantified for this load case. The predictive FE model can simulate the reaction force response seen in LC1 for the XPV16, XPV18, and XPV20 including UQ with an accuracy of 75.7%, 70.7%, and 73.1% respectively. Furthermore, the predictive FE model can simulate the stiffness response seen in LC1 for the XPV16, XPV18, and XPV20 including UQ with an accuracy of 65.3%, 50.3%, and 68.3% respectively.

Finally, possible future directions have been given that can improve the accuracy of the predictive FE model. These include improving the estimation of the stiffness in the Leaflet material fiber direction, Leaflet trim angle, Leaflet trim length, and the Pushrod y-offset, and conducting more experiments with samples from different production batches.

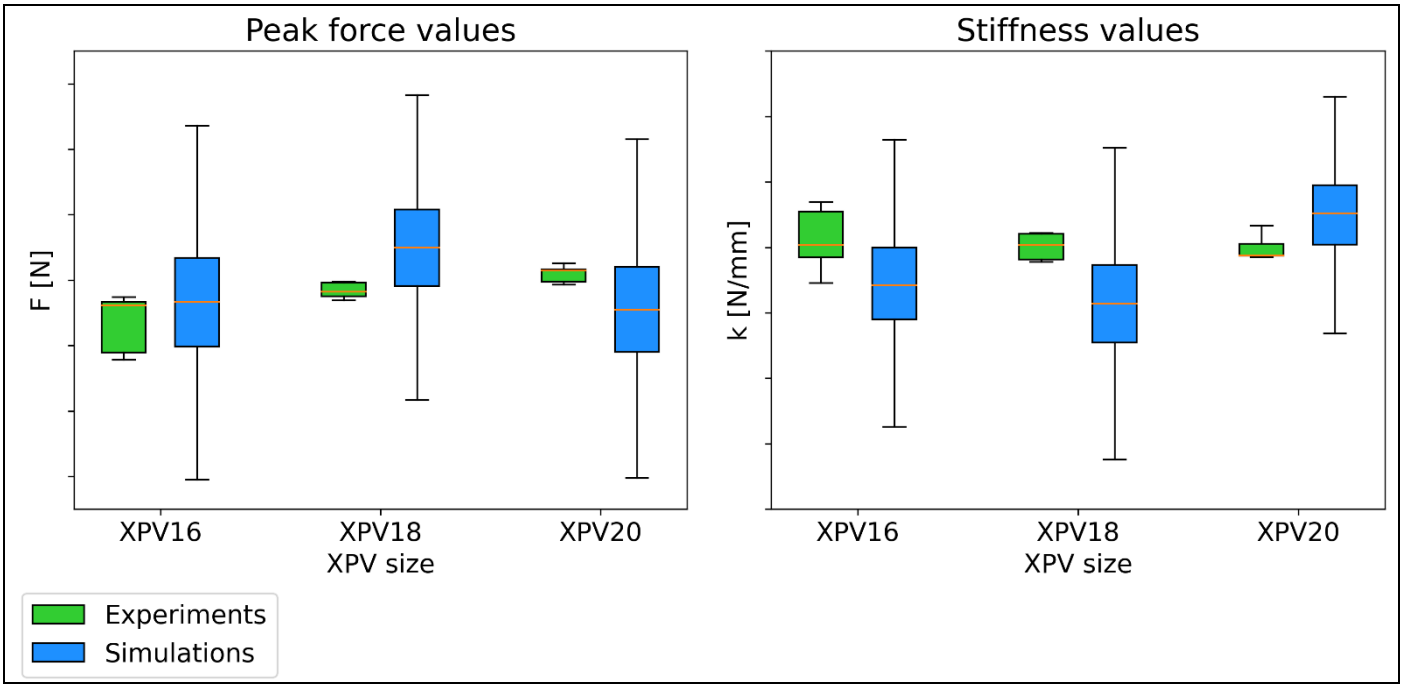

Figure 3-18: LC1, boxplots of the peak force values (left) and stiffness values (right) of the experiments and the simulations. The graphs with the numerical values of the peak force values and stiffness values are in Confidential Appendix D, Results and Discussion Graphs.

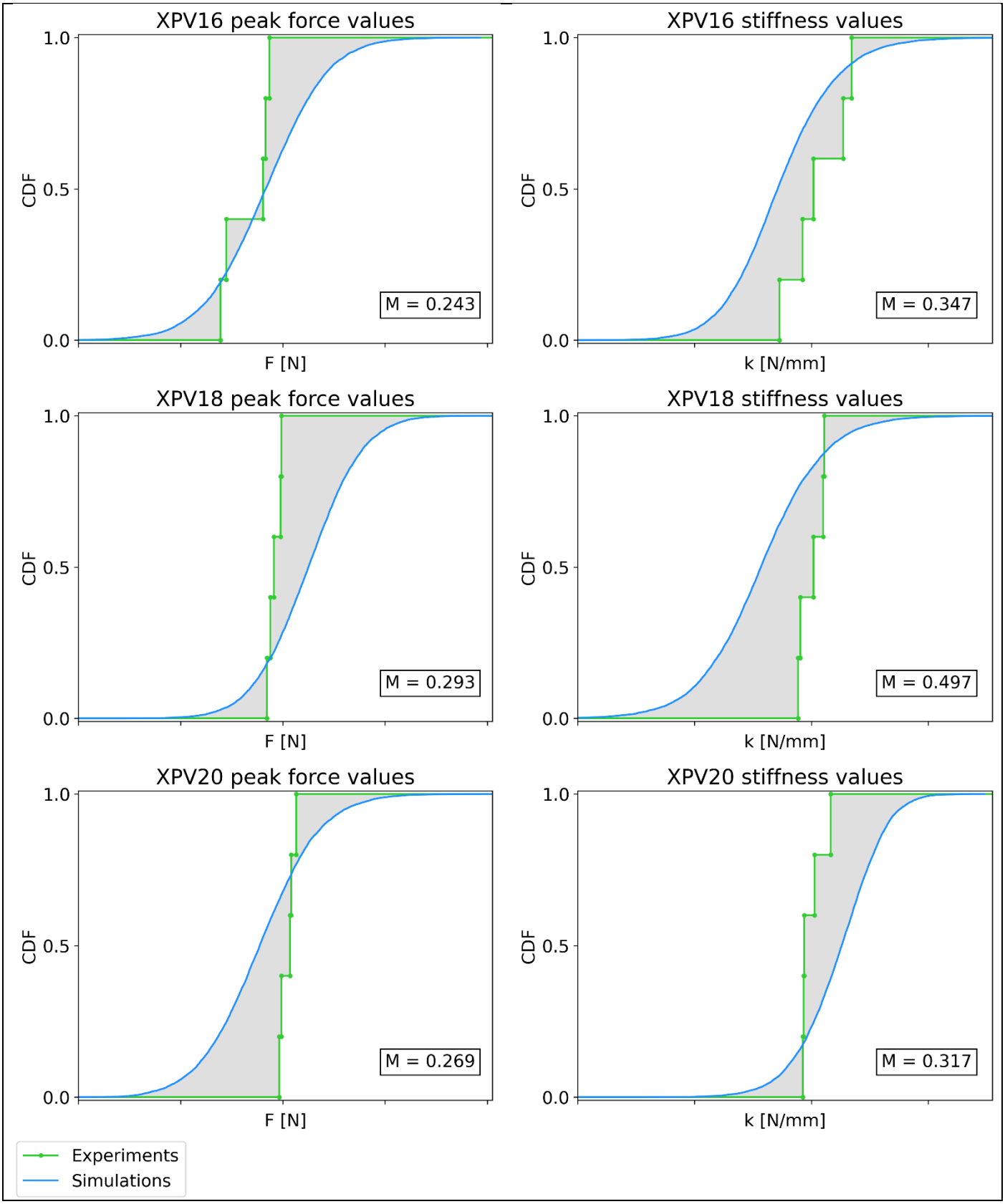

Figure 3-19: LC1, CDFs for peak force values (left) and stiffness values (right) for all XPV sizes of the experiments and the simulations. The value of the area metric 'M' is also displayed for each case. The area of the area metric is displayed in gray. The graphs with the numerical values of the peak force values and stiffness values are in Confidential Appendix D, Results and Discussion Graphs.

3.3.3 LC2, PARALLEL PLATE COMPRESSION

In Figure 3-20 the boxplots of the experiments and the simulations are shown to compare the distributions. Furthermore, the CDFs of the experiments and the simulations have been combined for the F_p values and the stiffness values for all XPV sizes. The area between the experiments CDF and simulations CDF has been used to calculate the area metric for all cases. The different CDFs for both the experiments and the simulations, highlighting the area between the CDFs, and showing the value of the area metric for this load case are shown in Figure 3-21. The graphs with the numerical values of the F_p values and stiffness values are in Confidential Appendix D, Results and Discussion Graphs. From the area metric, the relative error was obtained to compare the distribution of the simulation results to the distribution of the experiment results. Furthermore, the accuracy of the FE model has been calculated by taking the inverse of the area metric, which is listed in Table 3-5. Overall, the simulations are less in agreement than with LC1. Regarding the F_p relative errors, the XPV18 has the best agreement for this load case with a relative error of 51.4%. The other two sizes have a higher relative error, with an increase of 11.3% and 8.7% for the XPV16 and the XPV20 respectively. Regarding the stiffness relative error, the XPV20 has the best agreement for this load case with a relative error of 36.0%. The other two sizes have a higher relative error, with an increase of 25.9% and 6.9% for the XPV16 and the XPV18 respectively. Thus, the simulations of the XPV16 have the least agreement with the experiments based on the relative error based on the area metric. Furthermore, the simulations for all three XPV sizes estimate the F_p values and the stiffness values lower than the experiments. The CDFs of the experiments and the simulations don't cross for all cases. This means that the relative error based on the area metric is the same as the relative error based on the mean values (28).

Table 3-5: LC2, F_p values, and stiffness values relative error comparing the simulations with the experiment using the area metric parameter from Formula 3.1.

	Relative error based on the area metric		FE model accuracy	
Device size	F_p	Stiffness	F_p	Stiffness
XPV16	62.7%	61.9%	37.3%	38.1%
XPV18	51.4%	42.9%	48.6%	57.1%
XPV20	60.1%	36.0%	39.9%	64.0%

Based on the relative error based on the area metric, and the distributions shown in Figure 3-20 and Figure 3-21, there is a systematic difference between the simulations and the experiments. Looking at the input parameters that have a high sensitivity for the F_p values and the stiffness values (see Figure 3-16). Both are influenced mostly by the stiffness in the Conduit material fiber direction and the measure of Conduit material fiber direction along the circumferential direction for all XPV sizes. Also, the stiffness in the Leaflet material fiber direction influences the F_p values for the XPV16 and the XPV20, and the stiffness values for the XPV18 and XPV20 Thus, the relative error can be reduced by a better estimation of the stiffness in the Conduit material fiber direction, the measure of Conduit material fiber direction along the circumferential direction and the stiffness in the Leaflet material fiber direction. Likely, a better estimation of the stiffness in the Conduit material fiber direction will decrease the relative error the most out of the three parameters discussed based on the sensitivity analysis.

Thus, with the area metric the accuracy of the predictive FE model simulating the mechanical responses observed in the mechanical tests has been quantified for this load case. The predictive FE model can simulate the reaction force response seen in LC2 for the XPV16, XPV18, and XPV20 including UQ with an accuracy of 37.3%, 48.6%, and 39.9% respectively. Furthermore, the predictive FE model can simulate the stiffness response seen in LC2 for the XPV16, XPV18, and XPV20 including UQ with an accuracy of 38.1%, 57.1%, and 64.0% respectively.

Finally, possible future directions have been given that can improve the accuracy of the predictive FE model. These include improving the estimation of input parameters for the stiffness in the Conduit material fiber direction, the measure of Conduit material fiber direction along the circumferential direction, and the stiffness in the Leaflet material fiber direction. Here, a better estimation of the stiffness in the Conduit material fiber direction will have the largest impact in improving the accuracy of the predictive FE model based on the sensitivity analysis.

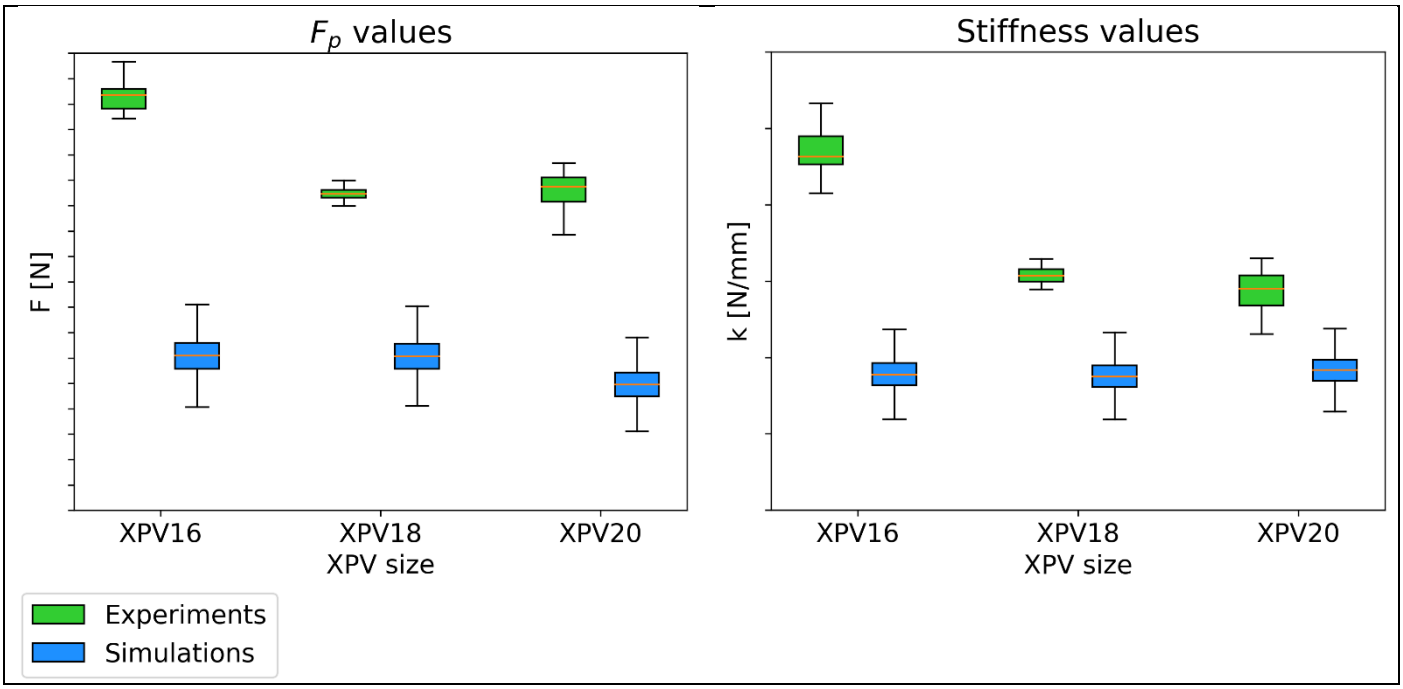

Figure 3-20: LC1, boxplots of the F_p values (left) and stiffness values (right) of the experiments and the simulations. The graphs with the numerical values of the F_p values and stiffness values are in Confidential Appendix D, Results and Discussion Graphs.

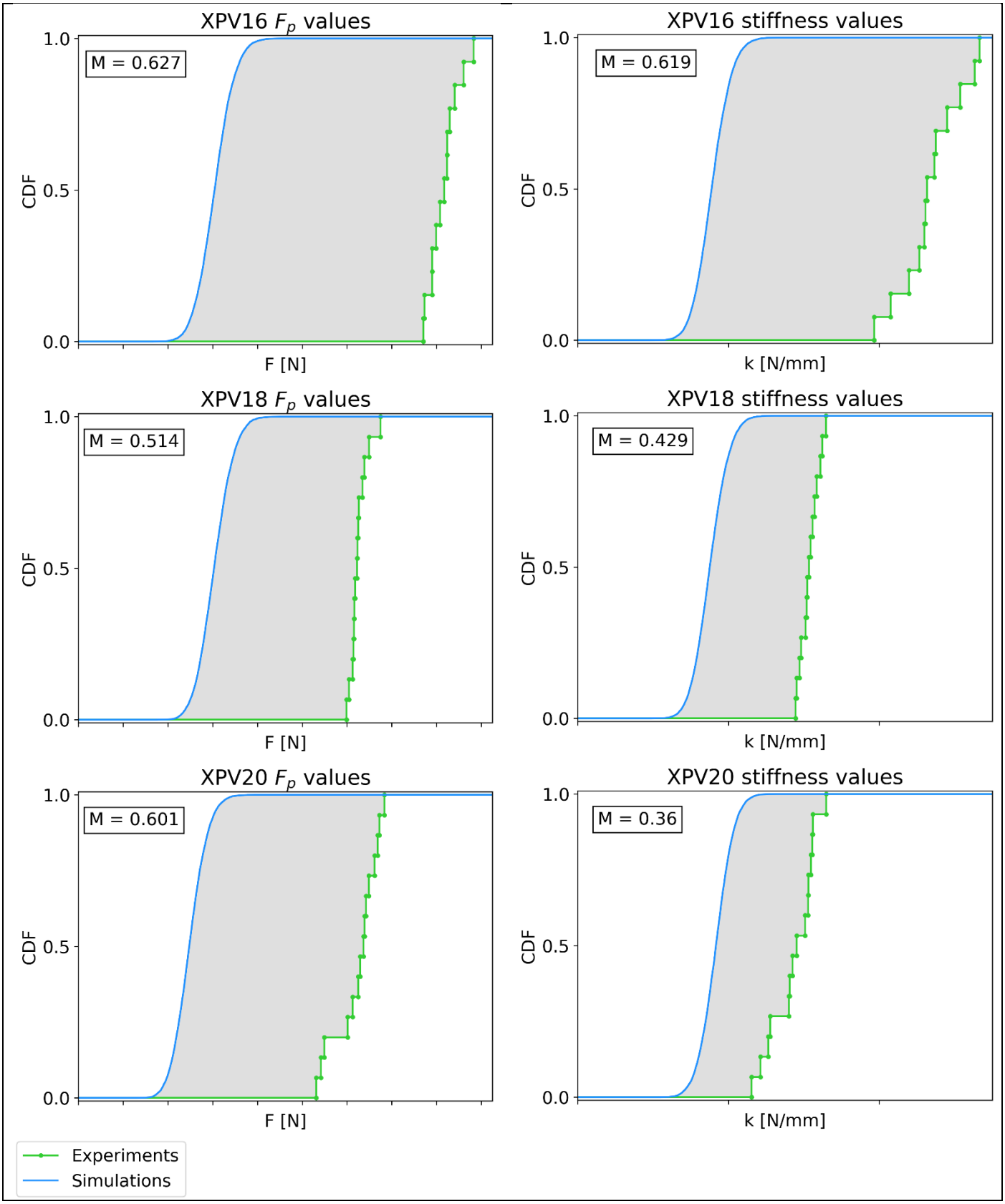

Figure 3-21: LC2, CDFs for F_p values (left) and stiffness values (right) for all XPV sizes of the experiments and the simulations. The value of the area metric 'M' is also displayed for each case. The area of the area metric is displayed in gray. The graphs with the numerical values of the F_p values and stiffness values are in Confidential Appendix D, Results and Discussion Graphs.

3.4 Implications on the Research Questions

3.4.1 The Mechanical Response of the XPV16, XPV18 and XPV20

Here the following research question will be discussed:

How does the mechanical response of the Xeltis™ pulmonary heart valve conduit sizes 16, 18, and 20 mm differ under two ISO 5840-1 specified mechanical loading conditions??

Two load cases were designed based on ISO 5840-1 'Cardiovascular implants – Cardiac valve prostheses – General requirements' (14). LC1 was designed to replicate the opening and closing behavior of the valve. LC2 was designed as this load case is used to validate the structural integrity of the device. A load protocol has been written and executed for LC1 and LC2. During the experiments, video measurements have been done to quantify uncertainties. From the mechanical experiments done for LC1 and LC2, force-displacement curves have been made for each test sample. These force-displacement curves show the variation in each load cycle and each sample. From the force-displacement curves output parameters have been defined and extracted. These include the peak force values and stiffness values for LC1. It also includes the F_p values and stiffness values for LC2. These values were used to perform a statistical analysis to quantify the difference in the mechanical response of the XPV16, XPV18, and XPV20 under the two mechanical load cases.

Regarding LC1, the peak force increases when the device size increases while the stiffness doesn't change with device size. Furthermore, the XPV16 has the highest variance in peak force values and stiffness values. Regarding LC2, F_p values and stiffness values increase when the XPV size decreases from size 18 to size 16. Furthermore, the difference between the XPV18 and the XPV20 is smaller for both F_p values and stiffness values. Finally, the XPV20 has the largest variance which could be caused by a sample from a different production batch.

3.4.2 Capturing the Mechanical Response of the XPV with a Computational FE model

Here the following research question will be discussed:

To what extent can finite element analysis capture the mechanical responses of Xeltis™ pulmonary heart valve conduits of varying sizes (16, 18, 20 mm)?

A computational FE model was developed to replicate the experiments. The FE model was created using multiple input parameters. These include geometry parameters, material parameters, and load case specific parameters (e.g., Pushrod position). Values of these parameters have been obtained by µCT measurements done on all samples by 4RealSim™, measurements with a caliper, and video measurements of the experiments for the geometry parameters and load case specific parameters. Furthermore, a parameter fitting study was done by TU-Graz (19) based on material experiments done by Leartiker™ (17). From these measurements, a distribution of input parameters was created to allow the propagation of uncertainties found in the experiments. Furthermore, output parameters were defined in the simulations, which were the same output parameters of the experiments. These include the peak force values and stiffness values for LC1. It also includes the F_p values and stiffness values for LC2. With the developed FE model, 900 FE simulations were performed of the first half cycle for each load case, 450 FE simulations for LC1, and 450 FE simulations for LC2. The values of the input parameters were randomly selected and would fall within previously defined distributions. Each FE simulation creates a DoE that was used to create an MM. From all DoEs the output parameters were extracted and with the MM a total of 20,000 data points were generated for the output parameters, 10,000 data points for LC1, and 100,000 data points for LC2. With these data points a Monte Carlo simulation was performed creating distributions of possible values for the output parameters.

Regarding LC1, according to the FE simulations, the XPV18 has a larger peak force than the XPV16 and the XPV20. The difference in peak force is smaller for the XPV16 and the XPV20. Furthermore, the XPV20 has a higher stiffness than the XPV16 and the XPV18. The difference in stiffness is smaller for the XPV16 and the XPV20. The FE model can capture the increase in peak force from the XPV16 to the XPV18, but the XPV20 does not follow the trend seen in the mechanical experiments for the reaction force. Furthermore, the FE model can capture the mechanical response seen for the stiffness of the XPV16 and the XPV18, as the stiffness changes slightly from the XPV16 to the XPV18 for both the simulations and the mechanical experiments. However, the FE model doesn't capture the stiffness response for the XPV20, as the stiffness increases significantly in the simulations as opposed to only a small change in the mechanical experiments. Thus, the FE model can capture the mechanical response of the XPV16 and XPV18 for LC1. However, for the XPV20 there are significant differences seen in the mechanical response in the simulations compared to the experiments for LC1.

Regarding L2, according to the FE simulations, the XPV20 has a smaller F_p than the XPV16 and the XPV18. The difference in F_p is smaller for the XPV16 and the XPV18. The FE model can capture the F_p and the stiffness for the XPV18 to the XPV20, as for both the simulations and the experiments they don't change a lot with a change in device size. However, the FE model doesn't capture the increase in F_p and stiffness for the XPV16 seen in the mechanical experiments. Thus, the FE model can capture the mechanical response of the XPV18 and XPV20 for LC2. However, for the XPV16 there are significant differences seen in the mechanical response in the simulations compared to the experiments for LC2.

3.4.3 The Variables with the Highest Influence on the Mechanical Response of the XPV

Here the following research question will be discussed:

What variables most significantly influence the reaction force and stiffness of the Xeltis™ pulmonary heart valve conduit sizes 16, 18, and 20 mm according to finite element models?

A sensitivity analysis was performed to quantify the sensitivity of the input parameters on the output parameters. variables have been identified that significantly influence the reaction force and the stiffness for both LC1 and LC2.

Regarding the peak force values in LC1, the stiffness in the Leaflet material fiber direction, the Leaflet trim angle, and the Leaflet trim length have a significant influence, all having a sensitivity higher than 10% for all XPV sizes. Regarding the F_p values in LC2, the stiffness in the Conduit material fiber direction and the measure of Conduit material fiber direction along the circumferential direction have a significant influence, all having a sensitivity higher than 10% for all XPV sizes. Furthermore, the stiffness in the Leaflet material fiber direction significantly influences the F_p values of the XPV16 and XPV20, having a sensitivity of 10%. Thus, the reaction force is influenced mostly by the fiber stiffness of the component that is subjected to the load. As in the Leaflet for LC1 and the Conduit for LC2. Furthermore, the reaction force is also influenced by the direction of the fibers. If the fibers are in the same direction as the load, the reaction force increases. This is most notable with the Conduit as it deforms in the circumferential direction. With the Leaflet this is less notable because it doesn't deform in a single material direction. For the Leaflet, the amount of material has more influence on the reaction force as can be seen by the high sensitivity of the Leaflet trimming parameters.

Regarding the stiffness values in LC1, the stiffness in the Leaflet material fiber direction and the Pushrod y-offset have a significant influence on the XPV16 having a sensitivity of 10% or higher. Furthermore, the Leaflet trim angle significantly influences the stiffness values of the XPV18, having a sensitivity higher than 20%. Finally, the Leaflet trim angle and the Pushrod y-offset significantly influence the stiffness values of the XPV20, having a sensitivity higher than 10%. Regarding the stiffness values in LC2, the stiffness in the Conduit material fiber direction and the measure of Conduit material fiber direction along the circumferential direction have a significant influence, all having a sensitivity higher than 10% for all XPV sizes. Furthermore, the stiffness in the Leaflet material fiber direction significantly influences the stiffness values of the XPV18 and XPV20, having a sensitivity higher than 10%. Thus, the stiffness is also influenced mostly by the fiber stiffness of the component that is subjected to the load. As in the Leaflet for LC1 and the Conduit for LC2. For LC1, the fiber stiffness of the Leaflet has a higher influence on the XPV16 than the XPV18 and XPV20. For the XPV18 and the XPV20, the amount of material in the Leaflet has a higher influence as indicated by the high sensitivity of the Leaflet trimming parameters. This indicates that for larger XPV sizes the material properties of the Leaflet have a smaller influence and the Leaflet geometry has a higher influence on the stiffness of the Leaflet opening.

3.4.4 The Accuracy of the Predictive Finite Element Model

Here the following research question will be discussed:

How accurately can a predictive finite element model simulate the mechanical responses observed in experimental tests on Xeltis™ pulmonary heart valve conduits of varying sizes (16, 18, 20 mm)?

The distributions of output values from the simulations were compared to the distribution of output values from the experiments for the XPV16, XPV18, and XPV20 with the area metric to quantify the accuracy of the FE model. The predictive FE model can simulate the reaction force response seen in LC1 for the XPV16, XPV18, and XPV20 including UQ with an accuracy of 75.7%, 70.7%, and 73.1% respectively. Furthermore, the predictive FE model can simulate the stiffness response seen in LC1 for the XPV16, XPV18, and XPV20 including UQ with an accuracy of 65.3%, 50.3%, and 68.3% respectively. Furthermore, the predictive FE model can simulate the reaction force response seen in LC2 for the XPV16, XPV18, and XPV20 including UQ with an accuracy of 37.3%, 48.6%, and 39.9% respectively. Furthermore, the predictive FE model can simulate the stiffness response seen in LC2 for the XPV16, XPV18, and XPV20 including UQ with an accuracy of 38.1%, 57.1%, and 64.0% respectively.

Thus, the FE model can simulate the reaction force response observed in LC1 38.4%, 22.1 and 33.2 more accurately than the reaction force response observed in LC2 for the XPV16, XPV18, and XPV20 respectively. Furthermore, the FE model can simulate the stiffness response observed in LC1 27.2% more accurately than the stiffness response observed in LC2 for the XPV16. However, the FE model can simulate the stiffness response observed in LC2 at 6.8% and 4.3% more accurately than the stiffness response observed in LC1 for the XPV18 and XPV20 respectively.

3.4.5 THE DIFFERENCE IN MECHANICAL RESPONSE BASED ON EXPERIMENTS AND A FINITE ELEMENT MODEL

With the answers to the above questions the main research question can be answered, which is:

What is the difference in the mechanical response of the Xeltis™ pulmonary heart valve conduit size 16, 18, and 20 mm based on mechanical experiments and a predictive finite element model?

With two mechanical experiments replicating in-vivo physiological loading standardized in ISO 5840-1 'Cardiovascular implants – Cardiac valve prostheses – General requirements' (14) and a predictive FE model using UQ the difference in the mechanical response of the XPV16, XPV18, and XPV20 have been quantified by using the reaction force and the stiffness as comparative parameters. Furthermore, important variables in the experiment have been identified using the FE model and the accuracy of the FE model has been quantified.

Regarding LC1, the reaction force increases when the device size increases while the stiffness doesn't change with device size. The FE model can capture the mechanical response of the XPV16 and XPV18 for LC1. However, for the XPV20 there are significant differences seen in the mechanical response in the simulations compared to the experiments for LC1. As for the accuracy of the predictive FE model, the predictive FE model can simulate the mechanical response of the stiffness with an accuracy of at least 70.7% for the reaction force and at least 50.3% for the stiffness. Here, the FE model of the XPV16 has the highest accuracy for the reaction force response, while the XPV20 has the highest accuracy for the stiffness response.

Regarding LC2, the reaction force and stiffness increase when the XPV size decreases from size 18 to size 16. Furthermore, the difference between the XPV18 and the XPV20 is smaller for both the reaction force and the stiffness. The FE model can capture the mechanical response of the XPV18 and XPV20 for LC2. However, for the XPV16 there are significant differences seen in the mechanical response in the simulations compared to the experiments for LC2. As for the accuracy of the predictive FE model, the predictive FE model can simulate the mechanical response of the stiffness with an accuracy of at least 37.3% for the reaction force and at least 38.1% for the stiffness. Here, the FE model of the XPV18 has the highest accuracy for the reaction force response, while the XPV20 has the highest accuracy for the stiffness response.

As for the important variables influencing the mechanical response, the reaction force is influenced mostly by the fiber stiffness of the component that is subjected to the load. As in the Leaflet for LC1 and the Conduit for LC2. Furthermore, the reaction force is also influenced by the direction of the fibers. If the fibers are in the same direction as the load, the reaction force increases. This is most notable with the Conduit as it deforms in the circumferential direction in LC2. With the Leaflet this is less notable because it doesn't deform in a single material direction for LC1. For the Leaflet, the amount of material has more influence on the reaction force as can be seen by the high sensitivity of the Leaflet trimming parameters. As for the stiffness, it is influenced mostly by the fiber stiffness of the component that is subjected to the load. As in the Leaflet for LC1 and the Conduit for LC2. For LC1, the fiber stiffness of the Leaflet has a higher influence on the XPV16 than the XPV18 and XPV20. For the XPV18 and the XPV20, the amount of material in the Leaflet has a higher influence as indicated by the high sensitivity of the Leaflet trimming parameters. This indicates that for larger XPV sizes the material properties of the Leaflet have a smaller influence and the Leaflet geometry has a higher influence on the stiffness of the Leaflet opening.

The FE model can simulate the reaction force response observed in LC1 38.4%, 22.1%, and 33.2% more accurately than the reaction force response observed in LC2 for the XPV16, XPV18, and XPV20 respectively. Furthermore, the FE model can simulate the stiffness response observed in LC1 27.2% more accurately than the stiffness response observed in LC2 for the XPV16. However, the FE model can simulate the stiffness response observed in LC2 at 6.8% and 4.3% more accurately than the stiffness response observed in LC1 for the XPV18 and XPV20 respectively.

3.5 Limitations and Future Directions

The FE model was created using symmetrical geometry to improve simulation run time. This might have a negative effect on the accuracy of the FE model. Specifically, the anisotropy in the material model introduces some asymmetrical properties. Although the effect of using a symmetrical model has been checked in one case, the full effect of using asymmetrical models has not been investigated. Furthermore, not all parameters that are defined for the geometry and the material model were used for the UQ and sensitivity analysis. Multiple parameters were left out because they were expected to have a low sensitivity for the load cases considered or were expected to not deviate from their mean values based on engineering judgment. Nevertheless, these parameters should be re-evaluated in future simulations and experiments.

The experiments were done with wet samples in a dry environment. No fluid dynamics were considered in the FE model, thus the effect of the samples being wet has not been investigated. Furthermore, the material model was calibrated with material tests done in a saline wet environment at a temperature of 37 °C (17). These environmental conditions were not replicated for these tests to simplify the test setup. The effect of this simplification on the agreement of the simulations to the experiments is unknown.

For each load case, future directions have been given that can improve the accuracy of the predictive FE model. Regarding the simulations, a better estimate of some input parameters could improve the accuracy of the predictive FE model. For LC1, these include a better estimation of the Leaflet trim angle, Leaflet trim length, the stiffness in the Leaflet material fiber direction, and the Pushrod y-offset. For LC2, these include a better estimation of the stiffness in the Conduit material fiber direction, the measure of Conduit material fiber direction along the circumferential direction, and the stiffness in the Leaflet material fiber direction. Regarding the experiments, samples from different production batches could improve the approximation of the total range of device variations, which improves the comparative quality of the experiments.

The experiments were done in vitro without being submerged in a fluid corresponding to human blood. A possible future direction would be to improve the accuracy of the in vitro experiment by using a fluid in combination with a load case simulating the in vivo hemodynamic conditions standardized in ISO 5840-1 ‘Cardiovascular implants – Cardiac valve prostheses – General requirements’ (14). Furthermore, when fluid dynamics have been applied to the experiments the simulations need to consider fluid dynamics as well. In this case a fluid-structure interaction (FSI) model provides the most accurate results for simulating the fluid dynamics of blood and the mechanics of the XPV device (29).

Another possible future direction would be to create a patient-specific computational model with the XPV device. This patient-specific model could be used to simulate and predict the in vivo hemodynamic conditions of a specific patient with the XPV device. This personalized simulation approach could be used to virtually plan the surgical procedure of the XPV device. Furthermore, designs of the XPV could be tested in a patient-specific environment to find the optimal XPV design for the patient (12). Finally, with a patient-specific FE model, the long-term lifetime of the XPV device can be investigated when the ETR process is incorporated into the computational model.

Regarding the MM and the Monte Carlo simulations performed using advanced data-driven techniques based on machine learning can improve simulation run time while providing accurate results is a possible next step for accurate patient-specific simulations providing predictive capabilities (30).

4 CONCLUSION

The goal of the study was to investigate the difference in the mechanical response of the XPV16, XPV18, and XPV20 using mechanical experiments and a predictive finite element model. With two mechanical experiments replicating in-vivo physiological loading standardized in ISO 5840-1 'Cardiovascular implants – Cardiac valve prostheses – General requirements' (14) and a predictive FE model using UQ the difference in the mechanical response of the XPV16, XPV18, and XPV20 have been quantified by using the reaction force and the stiffness as comparative parameters. Furthermore, important variables in the experiment have been identified using the FE model and the accuracy of the FE model has been quantified.

Regarding LC1, the reaction force increases when the device size increases while the stiffness doesn't change with device size. The FE model can capture the mechanical response of the XPV16 and XPV18 for LC1. However, for the XPV20 there are significant differences seen in the mechanical response in the simulations compared to the experiments for LC1. As for the accuracy of the predictive FE model, the predictive FE model can simulate the mechanical response of the stiffness with an accuracy of at least 70.7% for the reaction force and at least 50.3% for the stiffness.

Regarding LC2, the reaction force and stiffness increase when the XPV size decreases from size 18 to size 16. Furthermore, the difference between the XPV18 and the XPV20 is smaller for both the reaction force and the stiffness. The FE model can capture the mechanical response of the XPV18 and XPV20 for LC2. However, for the XPV16 there are significant differences seen in the mechanical response in the simulations compared to the experiments for LC2. As for the accuracy of the predictive FE model, the predictive FE model can simulate the mechanical response of the stiffness with an accuracy of at least 37.3% for the reaction force and at least 38.1% for the stiffness.

As for the important variables influencing the mechanical response, the reaction force and the stiffness are influenced mostly by the fiber stiffness of the component that is subjected to the load. As in the Leaflet for LC1 and the Conduit for LC2. Furthermore, the reaction force and stiffness are also influenced by the direction of the fibers. If the fibers are in the same direction as the load, the reaction force and stiffness increase. Although specifically for the Leaflet the amount of material has more influence on the reaction force and stiffness for larger XPV sizes for LC1. This indicates that for larger XPV sizes the material properties of the Leaflet have a smaller influence and the Leaflet geometry has a higher influence on the stiffness of the Leaflet opening.

The FE model can simulate the reaction force response observed in LC1 at least 22.1% more accurately than the reaction force response in LC2. Furthermore, the FE model can simulate the stiffness response observed in LC1 27.2% more accurately than the stiffness response observed in LC2 for the XPV16. However, for the other two sizes, the FE model of LC2 is at least 4.3% more accurate in simulating the stiffness response.

Improvements are possible for a better agreement between the simulation and the experiment. These include performing more experiments with different samples from different production batches, and better estimation of input parameters with a high sensitivity to the output parameters. Furthermore, in vitro experiments replicating in vivo, hemodynamic conditions could be a future step towards a computational FE model that can be used for the development of new XPV designs. Predictive patient-specific FE modeling can push that one step further. With predictive patient-specific FE modeling the surgical procedure of the XPV device could be planned virtually for a specific patient.

Finally, this study shows the benefit of predictive computational FE models and provides a step in the direction of predictive computational modeling that will help shorten the development time of new pulmonary heart valve devices. As the devices in this study are designed for pediatrics, this will help improve the quality of life of pediatrics suffering from congenital heart disease.

BIBLIOGRAPHY

1. Ptak, J. F. (2011, February). *A cardiac chronology (beginning): 27 heart Anatomies, 14th century-1897*. JF Ptak Science Books. https://longstreet.typepad.com/thesciencebookstore/2011/02/heart.html
2. Alkashkari, W., Albugami, S., Abbadi, M., Niyazi, A., Alsubei, A., & Hijazi, Z. M. (2020). Transcatheter pulmonary valve replacement in pediatric patients. *Expert Review of Medical Devices*, *17*(6), 541–554. https://doi.org/10.1080/17434440.2020.1775578
3. Iaizzo, P. A., Bianco, R. W., Hill, A. J., & St. Louis, J. D. (Eds.). (2013). *Heart Valves: From Design to Clinical Implantation*. Springer US. https://doi.org/10.1007/978-1-4614-6144-9
4. Kwon, M. H., & Baird, C. W. (2023). Surgical Valve Choices for Pulmonary Valve Replacement. *Seminars in Thoracic and Cardiovascular Surgery*, *35*(1), 94–104. https://doi.org/10.1053/j.semtcvs.2022.01.006
5. Morales, D. L., Herrington, C., Bacha, E. A., Morell, V. O., Prodán, Z., Mroczek, T., Sivalingam, S., Cox, M., Bennink, G., & Asch, F. M. (2021). A Novel Restorative Pulmonary Valve Conduit: Early Outcomes of Two Clinical Trials. *Frontiers in Cardiovascular Medicine*, *7*. https://www.frontiersin.org/articles/10.3389/fcvm.2020.583360
6. Mes, T., Serrero, A., Bauer, H. S., Cox, M. A. J., Bosman, A. W., Dankers, P. Y. W., & Meijer, E. W. (2022). Supramolecular polymer materials bring restorative heart valve therapy to patients. *Materials Today*, *52*, 175–187. https://doi.org/10.1016/j.mattod.2021.12.003
7. Viceconti, M., Pappalardo, F., Rodriguez, B., Horner, M., Bischoff, J., & Musuamba Tshinanu, F. (2021). In silico trials: Verification, validation and uncertainty quantification of predictive models used in the regulatory evaluation of biomedical products. *Methods*, *185*, 120–127. https://doi.org/10.1016/j.ymeth.2020.01.011
8. Lee, J. H., Rygg, A. D., Kolahdouz, E. M., Rossi, S., Retta, S. M., Duraiswamy, N., Scotten, L. N., Craven, B. A., & Griffith, B. E. (2020). Fluid–Structure Interaction Models of Bioprosthetic Heart Valve Dynamics in an Experimental Pulse Duplicator. *Annals of Biomedical Engineering*, *48*(5), 1475–1490. https://doi.org/10.1007/s10439-020-02466-4
9. Gharaie, S. H., Mosadegh, B., & Morsi, Y. (2018). In Vitro Validation of a Numerical Simulation of Leaflet Kinematics in a Polymeric Aortic Valve Under Physiological Conditions. *Cardiovascular Engineering and Technology*, *9*(1), 42–52. https://doi.org/10.1007/s13239-018-0340-7
10. Sun, W., Abad, A., & Sacks, M. S. (2005). Simulated Bioprosthetic Heart Valve Deformation under Quasi-Static Loading. *Journal of Biomechanical Engineering*, *127*(6), 905–914. https://doi.org/10.1115/1.2049337
11. Tango, A. M., Salmonsmith, J., Ducci, A., & Burriesci, G. (2018). Validation and Extension of a Fluid-Structure Interaction Model of the Healthy Aortic Valve. *Cardiovascular Engineering and Technology*, *9*(4), 739–751. https://doi.org/10.1007/s13239-018-00391-1
12. Pasta, S., Cannata, S., Gentile, G., Di Giuseppe, M., Cosentino, F., Pasta, F., Agnese, V., Bellavia, D., Raffa, G. M., Pilato, M., & Gandolfo, C. (2020). Simulation study of transcatheter heart valve implantation in patients with stenotic bicuspid aortic valve. *Medical & Biological Engineering & Computing*, *58*(4), 815–829. https://doi.org/10.1007/s11517-020-02138-4
13. Xu, F., Morganti, S., Zakerzadeh, R., Kamensky, D., Auricchio, F., Reali, A., Hughes, T. J. R., Sacks, M. S., & Hsu, M.-C. (2018). A framework for designing patient-specific bioprosthetic heart valves using immersogeometric fluid–structure interaction analysis. *International Journal for Numerical Methods in Biomedical Engineering*, *34*(4), e2938. https://doi.org/10.1002/cnm.2938
14. ISO 5840-1: Cardiovascular implants — Cardiac valve prostheses — Part 1 - General requirements, 2021

15. Open Source Physics. (2023). *Tracker*. Tracker Video Analysis and Modeling Tool for Physics Education. Retrieved January 19, 2023, from https://physlets.org/tracker/

16. Abaqus Analysis Guide, Dassault-Systemes, 2021, online-documentation

17. Isasi, M. (2022). SimInSitu-WP01-9-V1 Scaffold Characterization Report [Unpublished]

18. Rolf-Pissarczyk, M., Terzano, M. & Wollner, M. P. (2021). SimInSitu-WP02-5-V1 Scaffold UMAT-VUMAT Modelling and Verification Report. https://doi.org/10.3030/101017523

19. Rolf-Pissarczyk, M., Terzano, M. & Wollner, M. P. (2023). SimInSitu-WP02-2-V2 Scaffold UMAT-VUMAT Modelling and V&V Report [Unpublished]

20. Banks, H., Hu, S., & Kenz, Z. (2011). A Brief Review of Elasticity and Viscoelasticity. *Advances in Applied Mathematics and Mechanics*, *3*. https://doi.org/10.4208/aamm.10-m1030

21. Diani, J., Fayolle, B., & Gilormini, P. (2009). A review on the Mullins effect. *European Polymer Journal*, *45*(3), 601–612. https://doi.org/10.1016/j.eurpolymj.2008.11.017

22. Formlabs. (2016, September 4). *Material resin general purpose resins - formlabs*. Formlabs media. https://formlabs-media.formlabs.com/datasheets/1801089-TDS-ENUS-0P.pdf

23. Thames Stockholders. (2023). *Thames 1050A H14 - Thames Stock*. Thames Stockholders 1050A H14. https://www.thamesstock.com/assets/pdf/aluminium/1050a-aluminium-datasheet.pdf

24. Doebling, S. W., Hemez, F. M., Schultze, J. F., & Cundy, A. L. (2002). A Metamodel-Based Approach to Model Validation for Nonlinear Finite Element Simulations. *Los Angeles*.

25. Raychaudhuri, S. (2008). Introduction to Monte Carlo simulation. *2008 Winter Simulation Conference*, 91–100. https://doi.org/10.1109/WSC.2008.4736059

26. Graham, C., & Talay, D. (2013). Strong Law of Large Numbers and Monte Carlo Methods. In C. Graham & D. Talay (Eds.), *Stochastic Simulation and Monte Carlo Methods: Mathematical Foundations of Stochastic Simulation* (pp. 13–35). Springer. https://doi.org/10.1007/978-3-642-39363-1_2

27. Jafar, R., Labrosse, M. R., Weaver, J. D., Retta, S. M., Wu, C., & Duraiswamy, N. (2019). A Computational Study on Deformed Bioprosthetic Valve Geometries: Clinically Relevant Valve Performance Metrics. *Journal of Biomechanical Engineering*, *142*(1). https://doi.org/10.1115/1.4044235

28. ASME V&V Committee. An Illustration of the Concept of Verification and Validation in Computational Solid Mechanics. ASME, New York, USA, 2012.

29. Luraghi, G., Migliavacca, F., & Rodriguez Matas, J. F. (2018). Study on the Accuracy of Structural and FSI Heart Valves Simulations. *Cardiovascular Engineering and Technology*, *9*(4), 723–738. https://doi.org/10.1007/s13239-018-00373-3

30. Esmailie, F., Razavi, A., Yeats, B., Sivakumar, S. K., Chen, H., Samaee, M., Shah, I. A., Veneziani, A., Yadav, P., Thourani, V. H., & Dasi, L. P. (2022). Biomechanics of Transcatheter Aortic Valve Replacement Complications and Computational Predictive Modeling. *Structural Heart*, *6*(2), 100032. https://doi.org/10.1016/j.shj.2022.100032

31. Yoganathan, A. P., Fogel, M., Gamble, S., Morton, M., Schmidt, P., Secunda, J., Vidmar, S., & Nido, P. del. (2013, June 24). A new paradigm for obtaining marketing approval for pediatric-sized prosthetic heart valves. The Journal of Thoracic and Cardiovascular Surgery. Retrieved January 18, 2023, from https://www.jtcvs.org/article/S0022-5223(13)00480-7/fulltext

APPENDIX A, LEAFLET OPENING BEHAVIOR EXPERIMENTAL SETUP

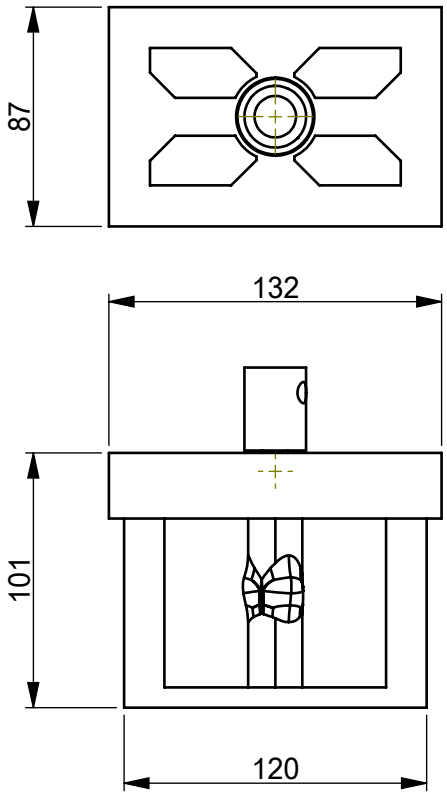

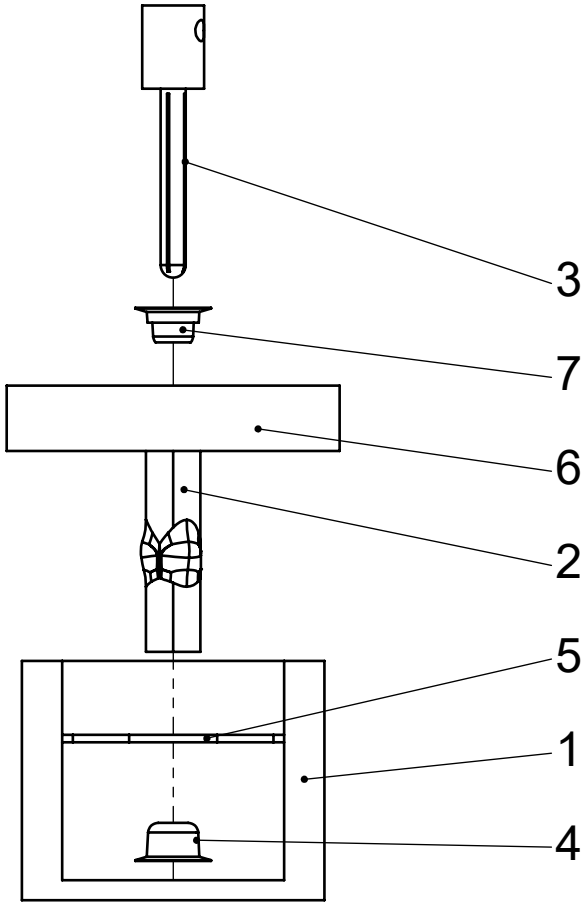

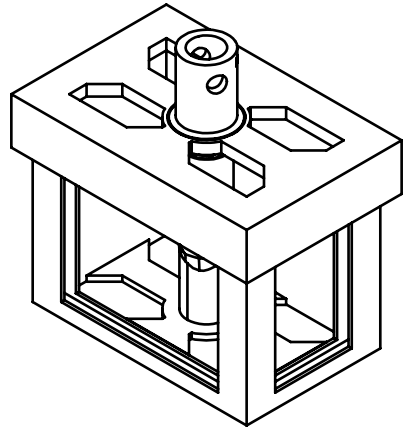

Item No.	Qty.	Name
7	1	LC1_Top_Fixture
6	1	LC1_Lid
5	1	LC1_Allignment_Plate
4	1	LC1_Bottom_Fixture
3	1	LC1_Pushrod
2	1	Sample
1	1	LC1_Box

TU Delft
Delft University of Technology

name
LC1_Test_Setup1

D:\Users\Rick\Documents\thesis\SolidWorks\

units	scale	quantity	date	remark
mm	1:3	1	8/22/2023	N.A.

material: See BoM
mass: gr
author: Rick van Tunen 4975189
group: N.A.
format: A4
drawing no.: 001

APPENDIX B, LC1 MISALIGNMENT MEASUREMENTS

All the tests have been recorded by two cameras, to capture the test in two perpendicular perspectives. By measuring the misalignment from these two recordings for each test a misalignment in three dimensions could be calculated. The measurement software used was Tracker (15), an open-source video analysis program. This program has been used to define vectors and points in the video as can be seen in Figure B 1. With this information, the radial misalignment, together with the angular misalignment was calculated. The misalignment directions and angles are visualized in Figure B 1.

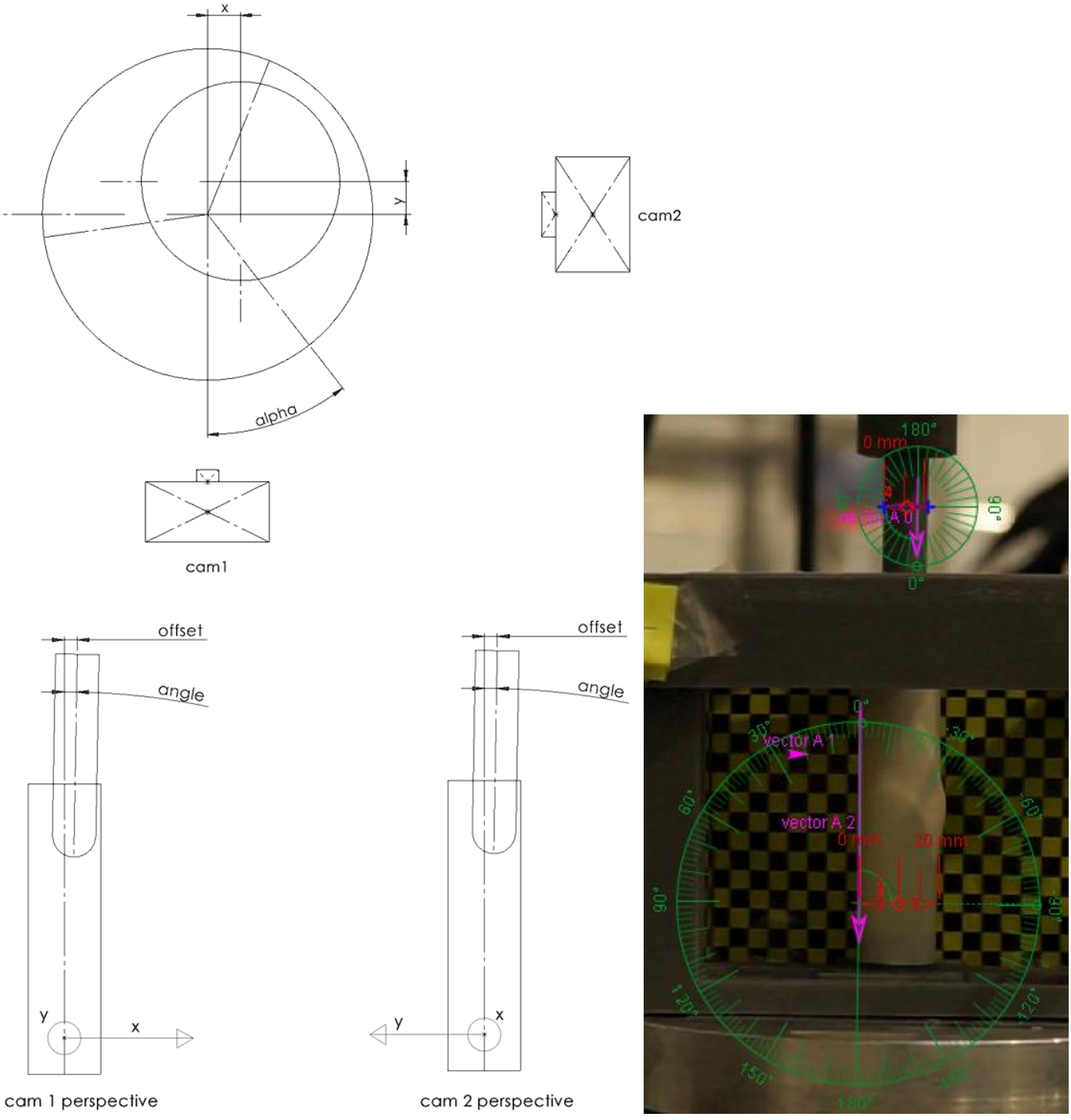

Figure B 1: Misalignment directions and measurements from two perspectives (left) and misalignment measurements in the Tracker software right.

The measured values were converted to values that correspond to misalignment values as defined in the computational model as shown in Figure 2-25, these values are listed in Table B 1. The misalignment value for all samples is below 2 mm radial misalignment and 1.5 degrees angular misalignment. These were the limits implemented in the DoE simulations. Thus, the misalignment values are between the computational model bounds. The Monte Carlo implemented the mean and STD from Table B 1 for the three sizes, which is an interpolation of the DoE. This ensured a good distribution for the misalignment values used in the model.

Table B 1: Misalignment values to be put in the model. Directions are defined from the coordinate system shown in Figure 2 22.

model input					
XPV16	**cam 1 perspective**		**cam 2 perspective**		
sample	**pushrod offset x [mm]**	**pushrod angle y [deg]**	**pushrod offset y [mm]**	**pushrod angle x [deg]**	**pushrod total offset [mm]**
PR-2008P16-01-041	1.42	0.34	0.80	0.26	1.63
PR-2008P16-01-030	-0.15	0.21	0.22	0.26	0.27
PR-2008P16-01-035	-0.80	0.48	0.22	0.12	0.82
PR-2008P16-01-045	-0.48	0.19	-0.37	0.07	0.61
mean	**-3.86E-04**	**0.30**	**0.22**	**0.18**	**0.83**
STD	**0.99**	**0.13**	**0.48**	**0.10**	**0.58**
XPV18	**cam 1 perspective**		**cam 2 perspective**		
sample	**pushrod offset x [mm]**	**pushrod angle y [deg]**	**pushrod offset y [mm]**	**pushrod angle x [deg]**	**pushrod total offset [mm]**
PR-2106P18-01-006	-0.07	0.00	0.66	0.02	0.67
PR-2106P18-01-002	-0.60	0.18	-0.47	0.43	0.76
PR-2106P18-01-005	-0.44	0.34	-0.64	0.21	0.78
PR-2106P18-01-013	-0.57	0.38	-0.28	0.28	0.63
PR-2106P18-01-014	1.20	0.00	0.02	0.28	1.20
mean	**-0.10**	**0.23**	**-0.34**	**0.30**	**0.85**
STD	**0.87**	**0.17**	**0.28**	**0.09**	**0.25**
XPV20	**cam 1 perspective**		**cam 2 perspective**		
sample	**pushrod offset x [mm]**	**pushrod angle y [deg]**	**pushrod offset y [mm]**	**pushrod angle x [deg]**	**pushrod total offset [mm]**
PR-2010P20-01-017	-0.29	0.06	1.35	0.05	1.38
PR-2010P20-01-007	1.02	0.12	1.27	0.18	1.63
PR-2010P20-01-008	-0.17	0.05	-0.46	0.19	0.49
PR-2010P20-01-010	0.92	0.01	1.76	0.08	1.99
PR-2105P20-01-004	0.56	0.31	-0.31	0.09	0.64
mean	**0.58**	**0.12**	**0.57**	**0.14**	**1.19**
STD	**0.54**	**0.13**	**1.12**	**0.06**	**0.74**

Appendix C, XPV FE Model Pressure Load Case Test

This load case was done to test the XPV FE model's capability to simulate a cardiac pressure cycle where the valve opens and closes. Pressures were derived from pressure data for an average adult during normotensive activity extracted from ISO 5840-1 'Cardiovascular implants – Cardiac valve prostheses – General requirements' (14). The pressure cycle was implemented with two pressure curves, one pressure curve on the right ventricle side of the device and one on the pulmonary artery side. The pressure curves were created by scaling a normalized heart cycle curve, extracted from ISO 5840-1 'Cardiovascular implants – Cardiac valve prostheses – General requirements' (14) to a maximum pulmonary artery pressure of 25 mmHg. The pressure curves are shown in Figure C 1. The mean artery pressure (MAP) of the pressure cycle was compared to a MAP for an in-vitro pulsatile flow test recommended by ISO 5840-1 'Cardiovascular implants – Cardiac valve prostheses – General requirements' (14) for pediatrics heart valves. Here it stated that a MAP of 20 mmHg should be considered for a pulsatile flow test. Because younger patients have a lower cardiac output (31), it was decided that the MAP of the adult pressure cycle should not be higher than a MAP of 20 mmHg to be considered a realistic normalized load case for the FE model.

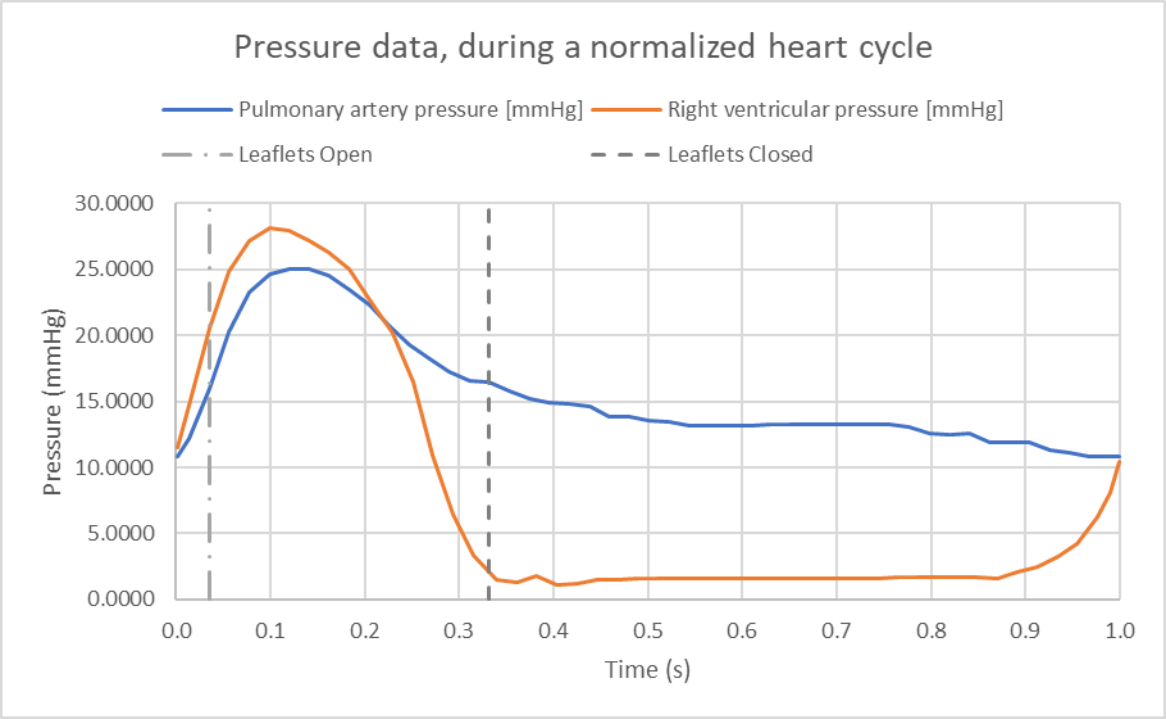

Figure C 1: Pressure data of the pulmonary artery and the right ventricle during a single normalized heart cycle. The leaflets open and leaflets closed time points correspond to the max and min peak pressure difference, modified from (14).

Step-2 pre-load

After the first step, which is described in 2.4.2, the second step was simulated. The second step was a pre-load step of 0.1 seconds where the pressure was increased to the starting pressure of the heart cycle with a smooth step amplitude of 10.8 mmHg. The pressure was uniformly distributed across the surfaces on both sides of the XPV, this is shown in Figure C 2. The BCs, constraints, and contact definitions described in 2.4.2 were used in this model. With a modification of the contact definitions. Here the contact was considered frictionless. Furthermore, mass scaling was applied such that the stable time increment was 1e-6 throughout the simulations. This was checked every 1000 increments. Finally, a viscous pressure of 1e-6 MPa was applied to the outside surface of the Conduit and outside surfaces of the Leaflets (see Figure C 3) to improve the numerical stability of the simulation.

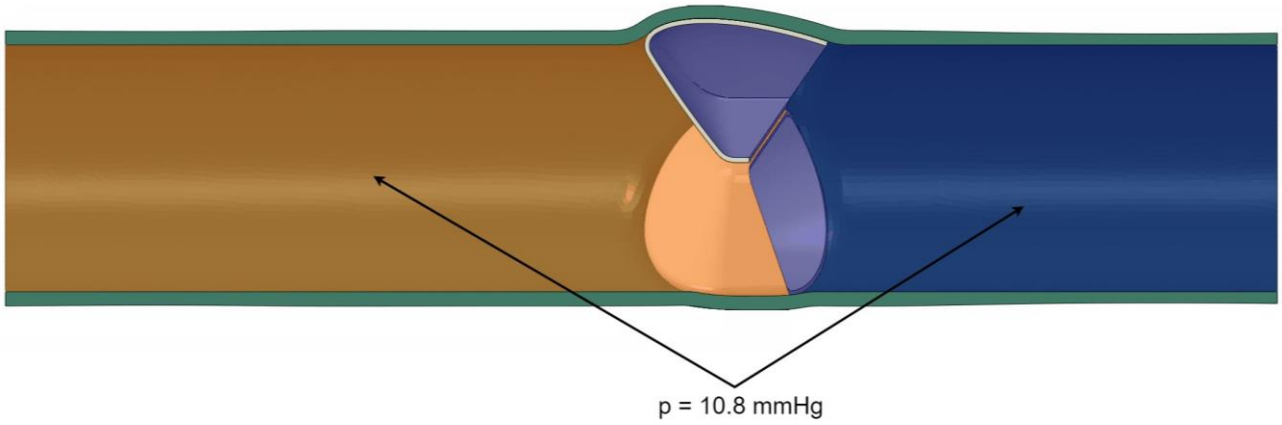

Figure C 2: Pre-load pressure BC the ventricle side of the XPV in orange and the pulmonary artery side in blue.

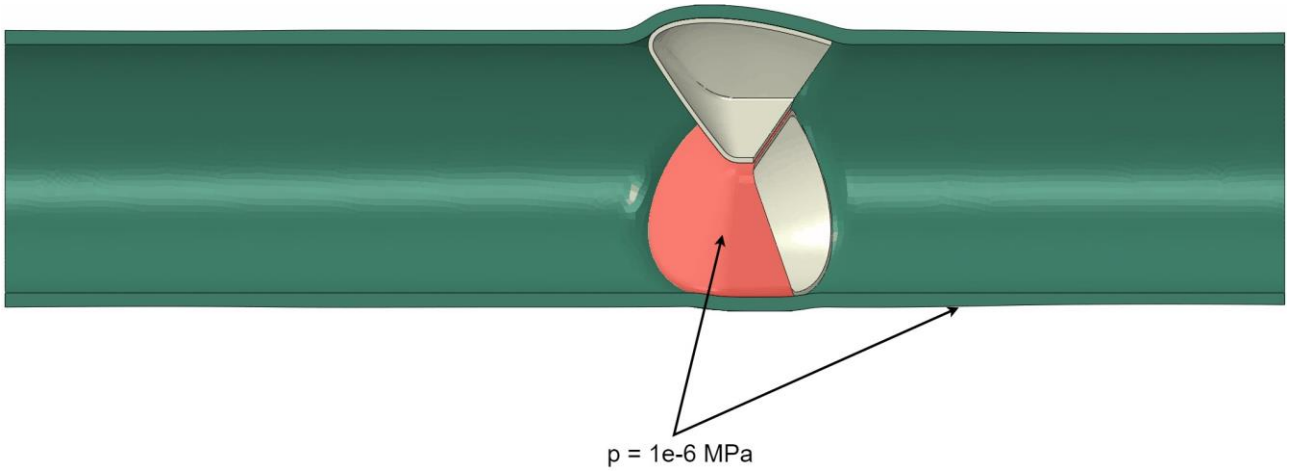

Figure C 3: Viscous pressure added to the outside surface of the Leaflets and the outside surface of the Conduit.

STEP-3 LEAFLET OPENING AND CLOSING

In this step, the heart cycle shown in Figure C 1 was applied to the model. The heart cycle was defined with two pressure cycles, one pressure cycle on the pulmonary side and one cycle on the ventricle side as shown in Figure C 4 for a duration of one second. Besides the heart cycle pressures applied to the model and time settings, definitions for the solver, BCs, constraints, and contact are identical to the previous step.

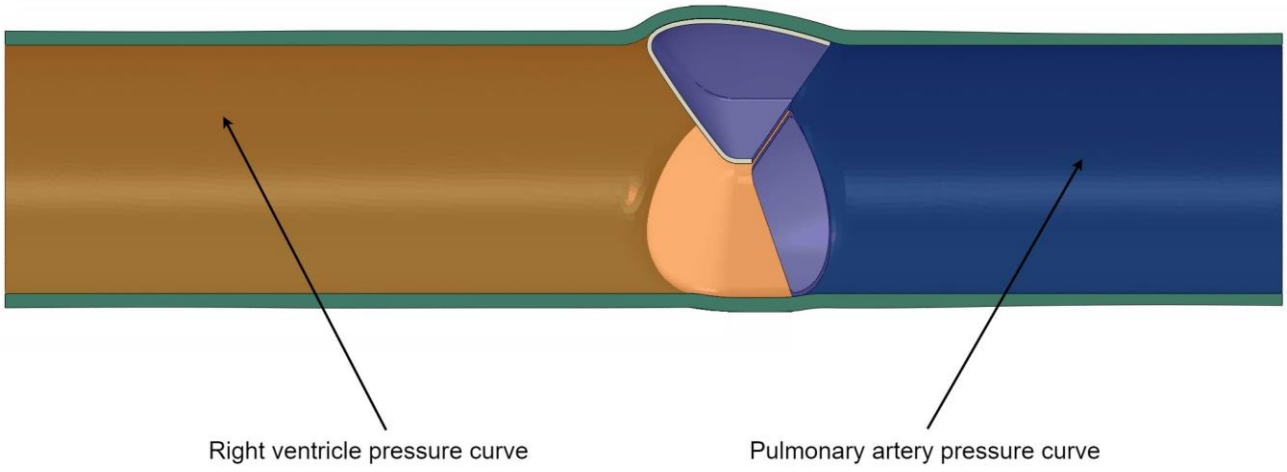

Figure C 4: Pressures applied for the opening and closing of the valve. The pressure curves are shown in Figure C 1

Simulation Results

Figure C 5 shows the opening and closing of the valve during the cardiac cycle of all three XPV sizes. Here, the valve can be seen opening symmetrically and closing properly. Thus, the XPV FE model simulates the opening and closing behavior of the valve when assessing the simulation results qualitatively for all three XPV sizes.

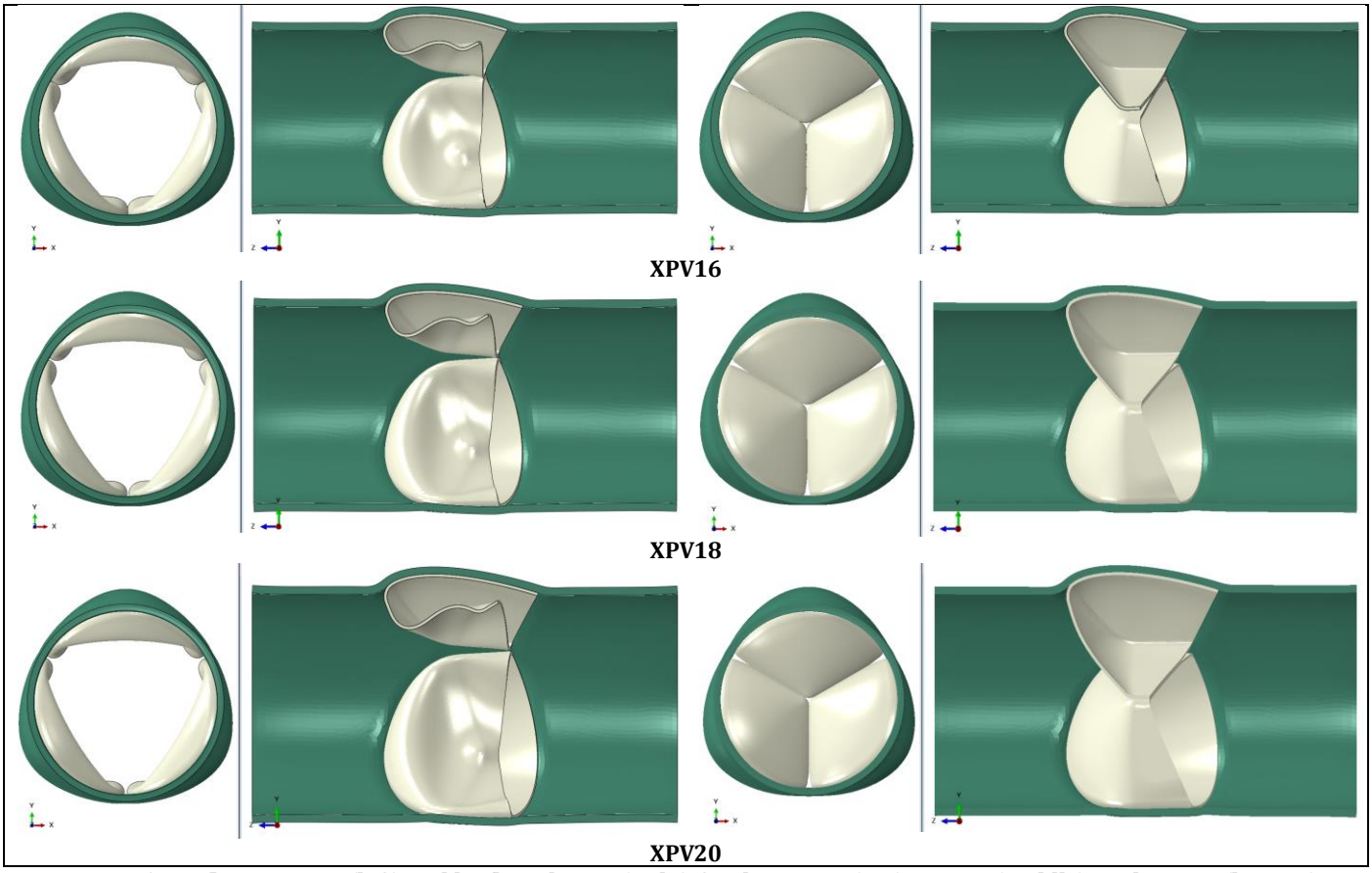

Figure C 5: Leaflets opening (left) and leaflets closing (right) for the XPV16 (top), XPV18 (middle), and XPV20 (bottom).

APPENDIX D, MATERIAL PARAMETERS DESCRIPTION

FORMULAS

Here the formulas used in the material model are listed. The highlighted parameters are the input parameters to the material model. All the other parameters are the internal parameters used in the material model. The internal parameters used in the material model are further described in Table D 1 and the input parameters are described in Table D 2. These formulas and their parameters are from (18, 19)

UNDAMAGED HYPERELASTIC RESPONSE

The undamaged hyperelastic response was described with the isochoric free energy density function (Formula D.1) and the volumetric free energy density function (Formula D.2). Parameters used in these functions are further specified in Formulas D.3 to D.9.

$$\psi_{iso}^{0,\infty} = \sum_{k=\{\parallel,\perp\}} \frac{\mu_k}{2}\left\{\frac{1}{(\gamma_k+1)}\left[(\bar{K}_{1k})^{\gamma_k+1}-1\right]+\frac{1}{(\delta_k+1)}\left[(\bar{K}_{-1k})^{\delta_k+1}-1\right]\right\} \tag{D.1}$$

$$\psi_{vol}^{0,\infty} = \frac{1}{D}(J-1)^2 \tag{D.2}$$

$$D = \frac{6(1-2\upsilon)}{(\mu_\parallel+\mu_\perp)(1+\upsilon)} \tag{D.3}$$

$$\bar{K}_{1k} = \mathbf{H}_k : \bar{\mathrm{C}} \tag{D.4}$$

$$\bar{K}_{-1k} = \mathbf{H}_k : \bar{\mathrm{C}}^{-1} \tag{D.5}$$

$$J = \det \mathbf{F} \tag{D.6}$$

$$\mathbf{H}_\parallel = \sum_{k=1}^{3} H_{kk}\, \boldsymbol{E}_k \otimes \boldsymbol{E}_k \tag{D.7}$$

$$\mathbf{H}_\perp = \frac{1}{2}(\mathbf{I}-\mathbf{H}_\parallel) \tag{D.8}$$

$$H_{33} = 1 - H_{11} - H_{22} \tag{D.9}$$

MULLINS EFFECT

The Mullins effect was described with the isochoric free energy density function (Formula D.10). The new parameter used in this function is further specified in Formula D.11.

$$\psi_{iso}^{m,\infty}\left(\psi_{iso}^{0,\infty},\psi_{iso}^{max}\right) = \left[\eta_{m0} + (1-\eta_{m0})\left(\chi^{\alpha_m} - \frac{\alpha_m}{\alpha_m+2}\chi^{\alpha_m+1}\right)\right]\psi_{iso}^{0,\infty} \tag{D.10}$$

$$\chi = \frac{\psi_{iso}^{0,\infty}}{\psi_{iso}^{max}} \tag{D.11}$$

PERMANENT SET

Here the residual stress was implemented with a Clausius-Duhem inequality. The reduced dissipation function is specified in Formula D.12.

$$D_{red\_r} = \eta_{r0}\alpha_r\left[\frac{1}{\alpha_r+2} + \frac{\alpha_r+1}{2\psi_{iso}^{max}}\sum_{k=1}^{N_{cyc}}\bar{\mathbf{S}}_k^{max} : \int_{\tau_{cyc,k}} \chi^{\alpha_r}(1-\chi)\dot{\bar{\mathrm{C}}}\, d\tau\right]\psi_{iso}^{max} \geq 0 \tag{D.12}$$

VISCOELASTICITY

The viscoelasticity was implemented with a Clausius-Duhem inequality as well. The reduced dissipation function is specified in Formula D.13. Parameters used in this function are further specified in Formulas D.14. The material model uses a maximum of three viscous Maxwell elements to simulate viscoelasticity. It should be noted that μ'_k is not the stiffness of the spring in a Maxwell element but follows the proportional relation in Formula D.15. The larger μ'_k, the smaller the viscous stress contribution.

$$D_{red\_v} = -\frac{1}{2\mu'_k}\mathbf{Q}_k : \dot{\bar{\mathbf{S}}}^{0,\infty} \geq 0 \tag{D.13}$$

$$\mathbf{Q}_k|_{n+1} = e^{-\left(\frac{\Delta t}{2\tau_k}\right)}\left[e^{-\left(\frac{\Delta t}{2\tau_k}\right)}\mathbf{Q}_k|_n - \bar{\mathbf{S}}^{0,\infty}|_n\right] + e^{-\left(\frac{\Delta t}{2\tau_k}\right)}\bar{\mathbf{S}}^{0,\infty}|_{n+1} \tag{D.14}$$

$$\mu'_k \propto \frac{\text{ground stiffness} \times \text{ground stiffness}}{\text{stiffness of the } k\text{th Maxwell element}} \tag{D.15}$$

SOLVER SPECIFIC

Finally, with the material model the stable time increment used in the Abaqus Explicit solver is calculated with the Formulas D.16 to D.19.

$$\Delta t \approx \frac{L_{min}}{c_d} \tag{D.16}$$

$$c_d = \sqrt{\frac{\lambda_0 + 2\mu_0}{\rho}} \tag{D.17}$$

$$\mu_0 = \frac{1}{2}(\mu_{\parallel} + \mu_{\perp}) \tag{D.18}$$

$$\lambda_0 = \frac{2}{D} - \frac{2}{3\mu_0} \tag{D.19}$$

Table D 1: Material model parameters description

Parameters describing material property	Description
Undamaged hyperelastic response	
$\psi_{iso}^{0,\infty}$	Isochoric free energy density function describing the undamaged hyperelastic response
$\psi_{vol}^{0,\infty}$	Volumetric free energy density function describing the undamaged hyperelastic response
D	Inverse of the bulk modulus
J	Local volume scale factor
$\overline{K}_{1k}$ and $\overline{K}_{-1k}$	Isochoric invariants
$\overline{\mathrm{C}}$	Isochoric right Cauchy-Green tensor
$\mathbf{F}$	The deformation gradient
υ	Poisson ratio
$\mathbf{H}_{\parallel}$	Coaxial structure tensor
$\mathbf{H}_{\perp}$	Perpendicular structure tensor
$\boldsymbol{E}_k$	Orthogonal eigenvectors basis
$\mathbf{I}$	Identity tensor
H_{33}	Measure of fiber orientation along the radial direction
Mullins effect	
ψ_{iso}^{max}	Maximally attained undamaged isochoric free energy density
$\psi_{iso}^{m,\infty}$	Isochoric free energy density function including the Mullins effect
χ	Ratio between the undamaged isochoric free energy density function and the maximally attained undamaged isochoric free energy density
Permanent set	
D_{red_r}	Reduced dissipation according to the Clausius-Duhem inequality for the residual stress
$\bar{\mathbf{S}}_k^{max}$	Undamaged isochoric stress state at the instance of maximum attained undamaged isochoric free energy density ψ_{iso}^{max}
N_{cyc}	Number of loading and unloading cycles
$\tau_{cyc,k}$	Time interval for each cycle
Viscoelasticity	
D_{red_v}	Reduced dissipation according to the Clausius-Duhem inequality for the viscoelasticity
$\mathbf{Q}_k$	Auxiliary non-equilibrium stress tensor
$\dot{\bar{\mathbf{S}}}^{0,\infty}$	The 2nd Piola-Kirchhoff stress tensor
$\mathbf{Q}_k\|_{n+1}$	Approximation of $\mathbf{Q}_k$ at timepoint t_{n+1} with numerical integration
$\mathbf{Q}_k\|_n$	Approximation of $\mathbf{Q}_k$ at timepoint t_n with numerical integration
$\bar{\mathbf{S}}^{0,\infty}\|_n$	The 2nd Piola-Kirchhoff stress tensor at timepoint t_n
$\bar{\mathbf{S}}^{0,\infty}\|_{n+1}$	The 2nd Piola-Kirchhoff stress tensor at timepoint t_{n+1}
Δt	The time increment $t_{n+1} - t_n$
Solver specific	
L_{min}	The characteristic size of the smallest element in the mesh
c_d	The wave speed
μ_0	Lame's first constant
λ_0	Lame's second constant

Table D 2: Input parameters for the material model

User defined parameters for undamaged hyperelastic response	Parameter names in the code	Description
H_{11}	Mat XP034 PR01 a11, Mat XP005 PR01 a11	Measure of fiber orientation along the axial direction
H_{22}	Mat XP034 PR02 a22, Mat XP005 PR02 a22	Measure of fiber orientation along the circumferential direction
μ_k	Mat XP034 PR03 mp, Mat XP034 PR06 mn, Mat XP005 PR03 mp, Mat XP005 PR06 mn	Fiber stiffness along the fiber direction ($k = \parallel$) or perpendicular to the fiber direction ($k = \perp$)
γ_k	Mat XP034 PR04 gp, Mat XP034 PR07 gn, Mat XP005 PR04 gp, Mat XP005 PR07 gn	Shape parameter associated with a line element along the fiber direction ($k = \parallel$) or perpendicular to the fiber direction ($k = \perp$)
δ_k	Mat XP034 PR05 dp, Mat XP034 PR08 dn, Mat XP005 PR05 dp, Mat XP034 PR08 dn	Shape parameter associated with an area element along the fiber direction ($k = \parallel$) or perpendicular to the fiber direction ($k = \perp$)
υ	Mat XP034 Poisson Ratio, Mat XP005 Poisson Ratio	Poisson ratio
User defined parameters for Mullins effect		
η_{m0}	Mat XP034 PR10 eta0m, Mat XP005 PR10 eta0m	Maximum stiffness loss due to the Mullins effect
α_m	Mat XP034 PR11 alphm, Mat XP005 PR11 alphm	Stiffness loss evolution due to the Mullins effect during unloading and reloading
Permanent set		
η_{r0}	Mat XP034 PR12 eta0r, Mat XP005 PR12 eta0r	Maximum residual stress contribution
α_r	Mat XP034 PR13 alphr, Mat XP005 PR13 alphr	Residual stress evolution during unloading and reloading
Viscoelasticity		
${\mu'_k}^{-1}$	Mat XP034 PR15 mvis1, Mat XP034 PR15 mvis2, Mat XP034 PR15 mvis3, Mat XP005 PR15 mvis1, Mat XP005 PR15 mvis2, Mat XP005 PR15 mvis3	Stiffness-like parameter of the Maxwell element
τ_k	Mat XP034 PR14 tvis2, Mat XP034 PR14 tvis2, Mat XP034 PR14 tvis3, Mat XP005 PR14 tvis1, Mat XP005 PR14 tvis2, Mat XP005 PR14 tvis3	Relaxation time
Solver specific		
ρ	Mat XP034 Density, Mat XP005 Density	Density

APPENDIX E, LC1 FORCE DISPLACEMENT CURVES OF THE EXPERIMENTS

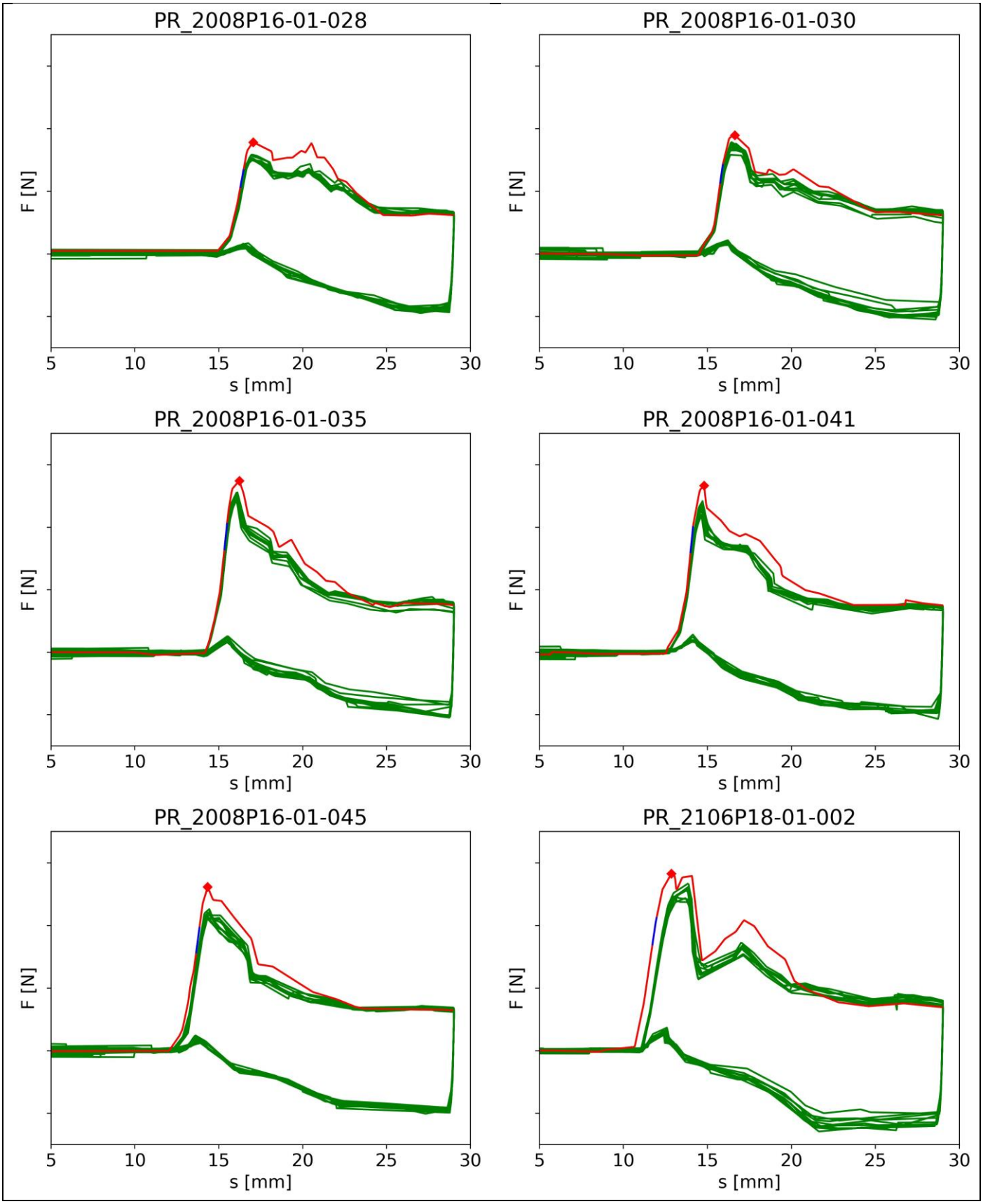

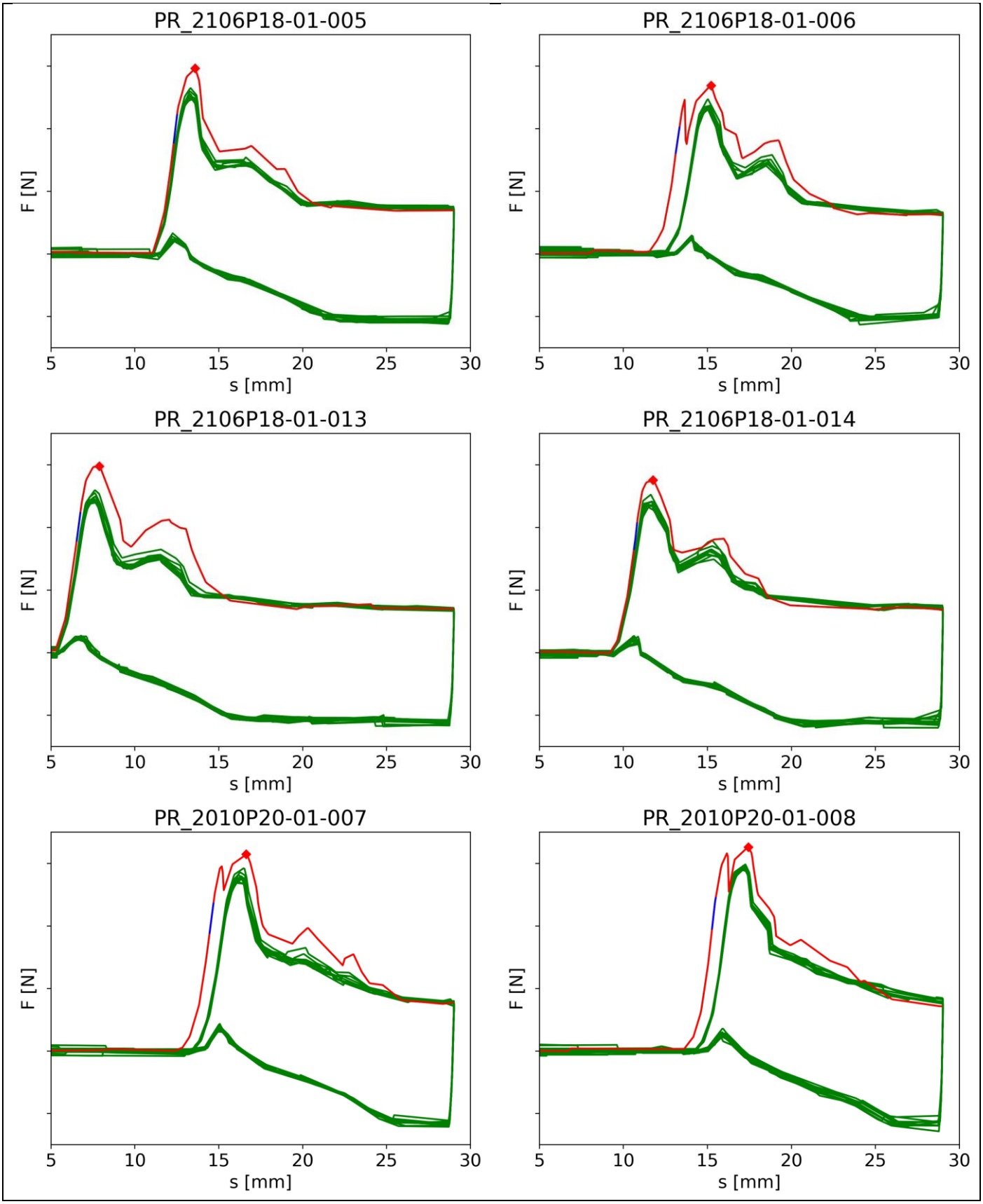
PR_2106P18-01-005
PR_2106P18-01-006
PR_2106P18-01-013
PR_2106P18-01-014
PR_2010P20-01-007
PR_2010P20-01-008
F [N]
s [mm]
5
10
15
20
25
30

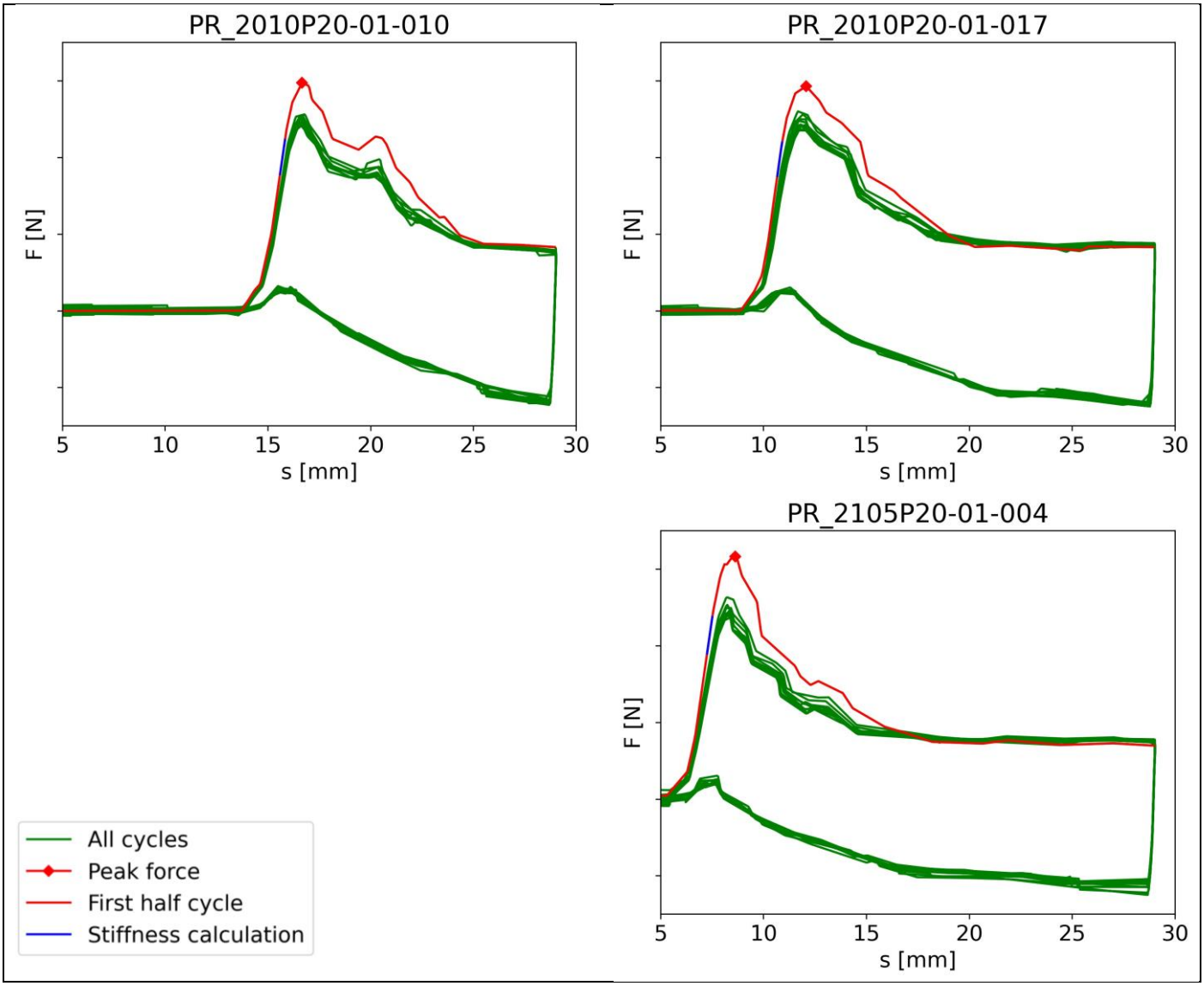
PR_2010P20-01-010
PR_2010P20-01-017
PR_2105P20-01-004
F [N]
s [mm]
5
10
15
20
25
30
All cycles
Peak force
First half cycle
Stiffness calculation

APPENDIX F, LC2 FORCE DISPLACEMENT CURVES OF THE EXPERIMENTS

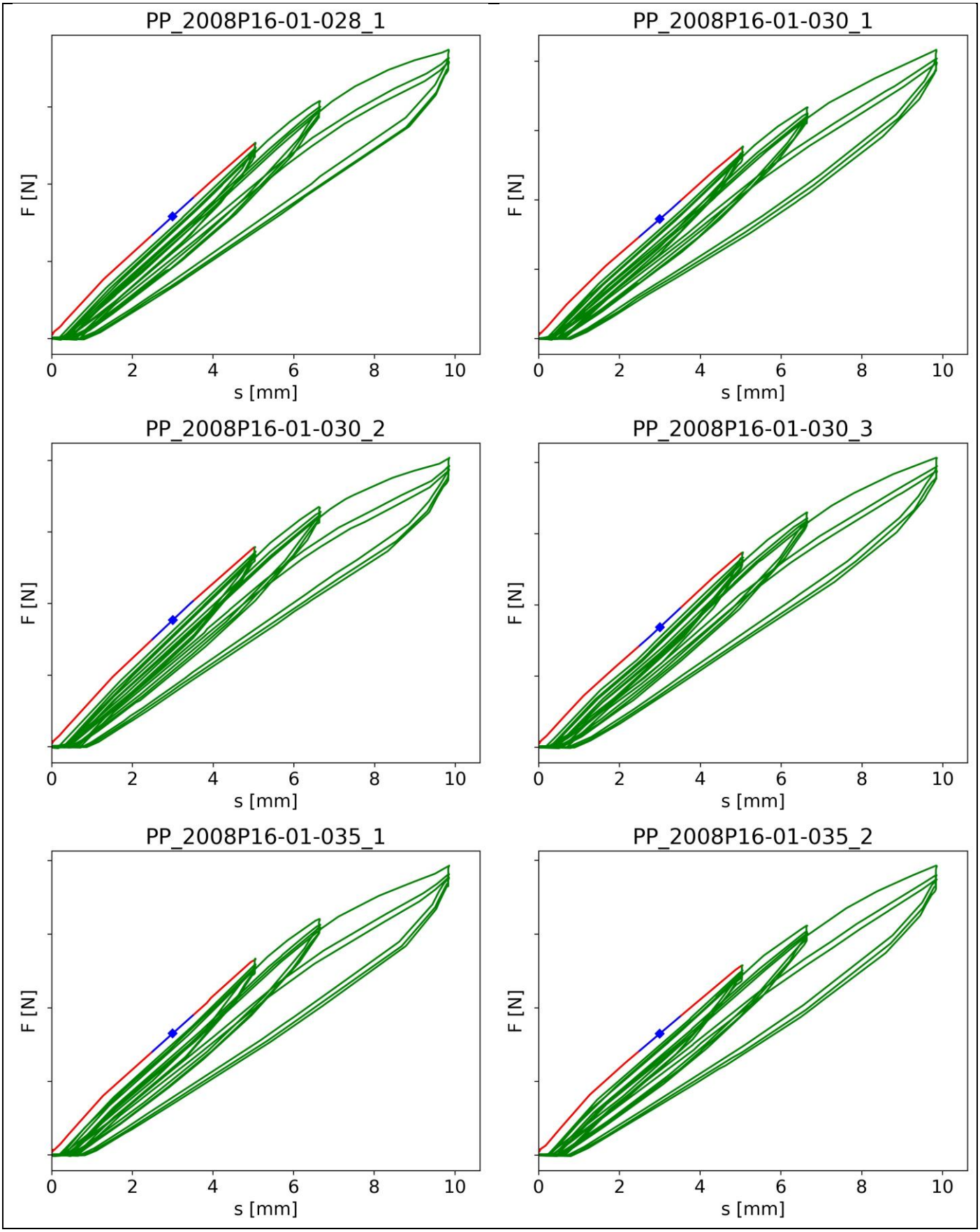

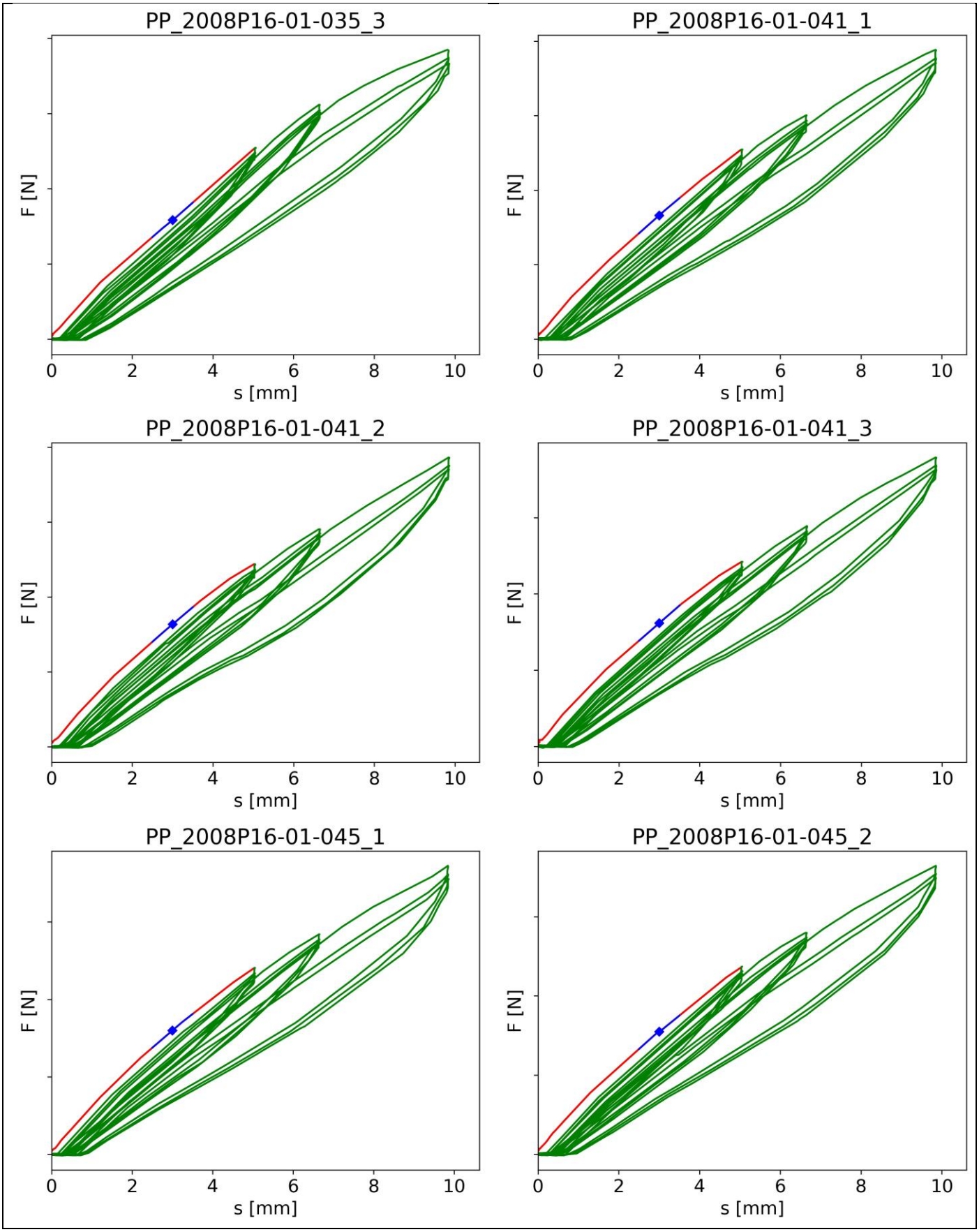
PP_2008P16-01-035_3
PP_2008P16-01-041_1
PP_2008P16-01-041_2
PP_2008P16-01-041_3
PP_2008P16-01-045_1
PP_2008P16-01-045_2
F [N]
s [mm]
0
2
4
6
8
10

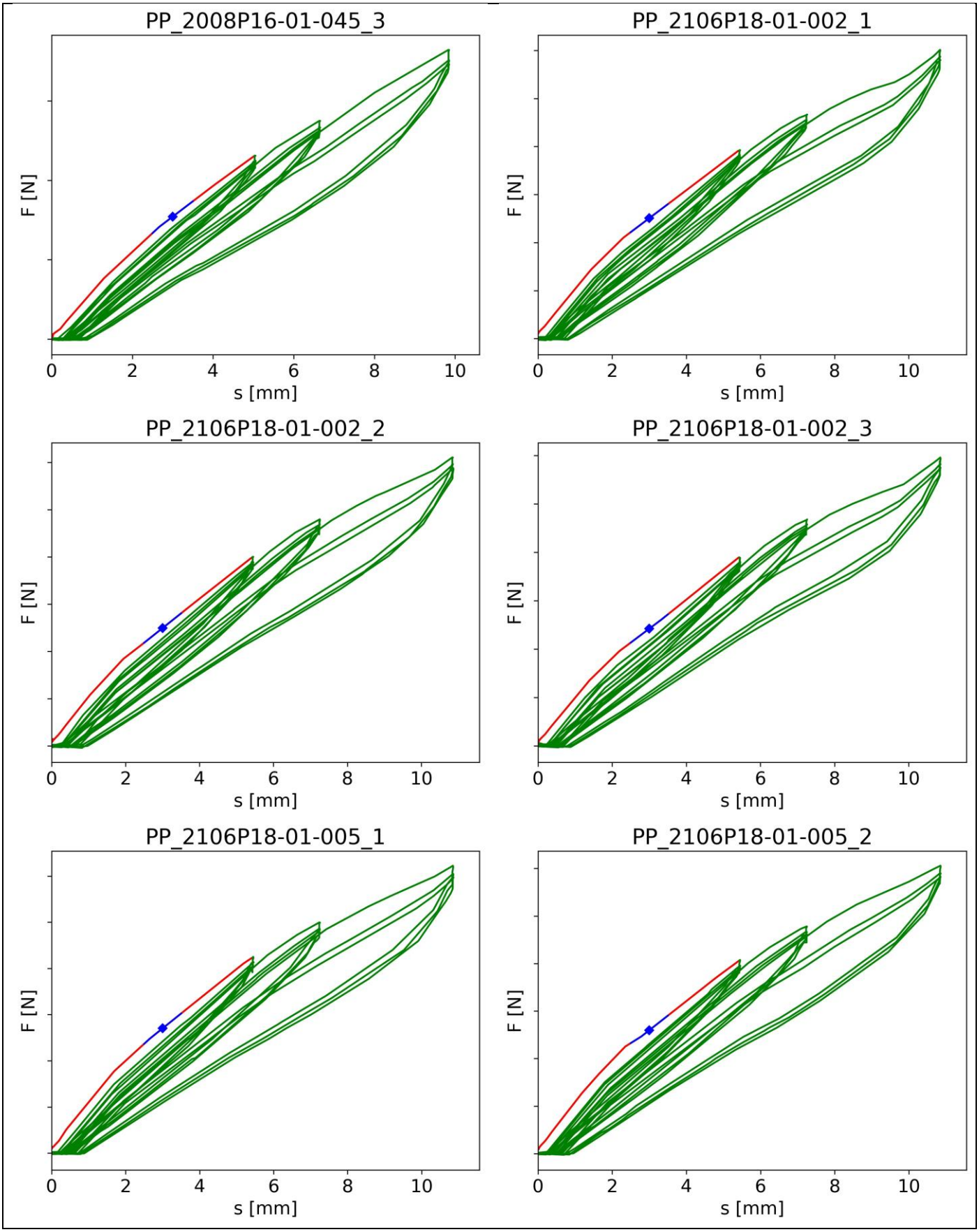
PP_2008P16-01-045_3
PP_2106P18-01-002_1
PP_2106P18-01-002_2
PP_2106P18-01-002_3
PP_2106P18-01-005_1
PP_2106P18-01-005_2
F [N]
s [mm]
0
2
4
6
8
10

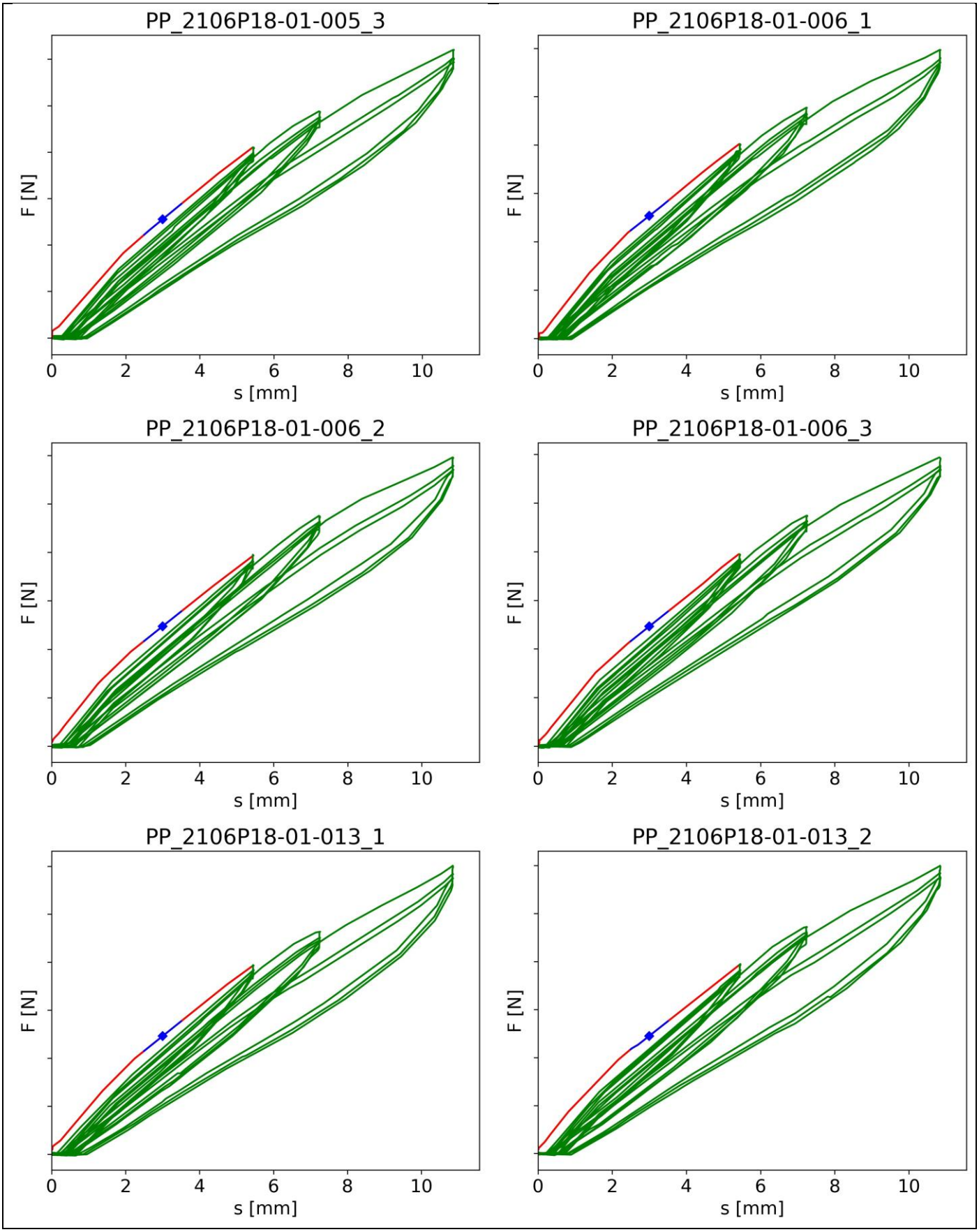
PP_2106P18-01-005_3
PP_2106P18-01-006_1
PP_2106P18-01-006_2
PP_2106P18-01-006_3
PP_2106P18-01-013_1
PP_2106P18-01-013_2
F [N]
s [mm]
0
2
4
6
8
10

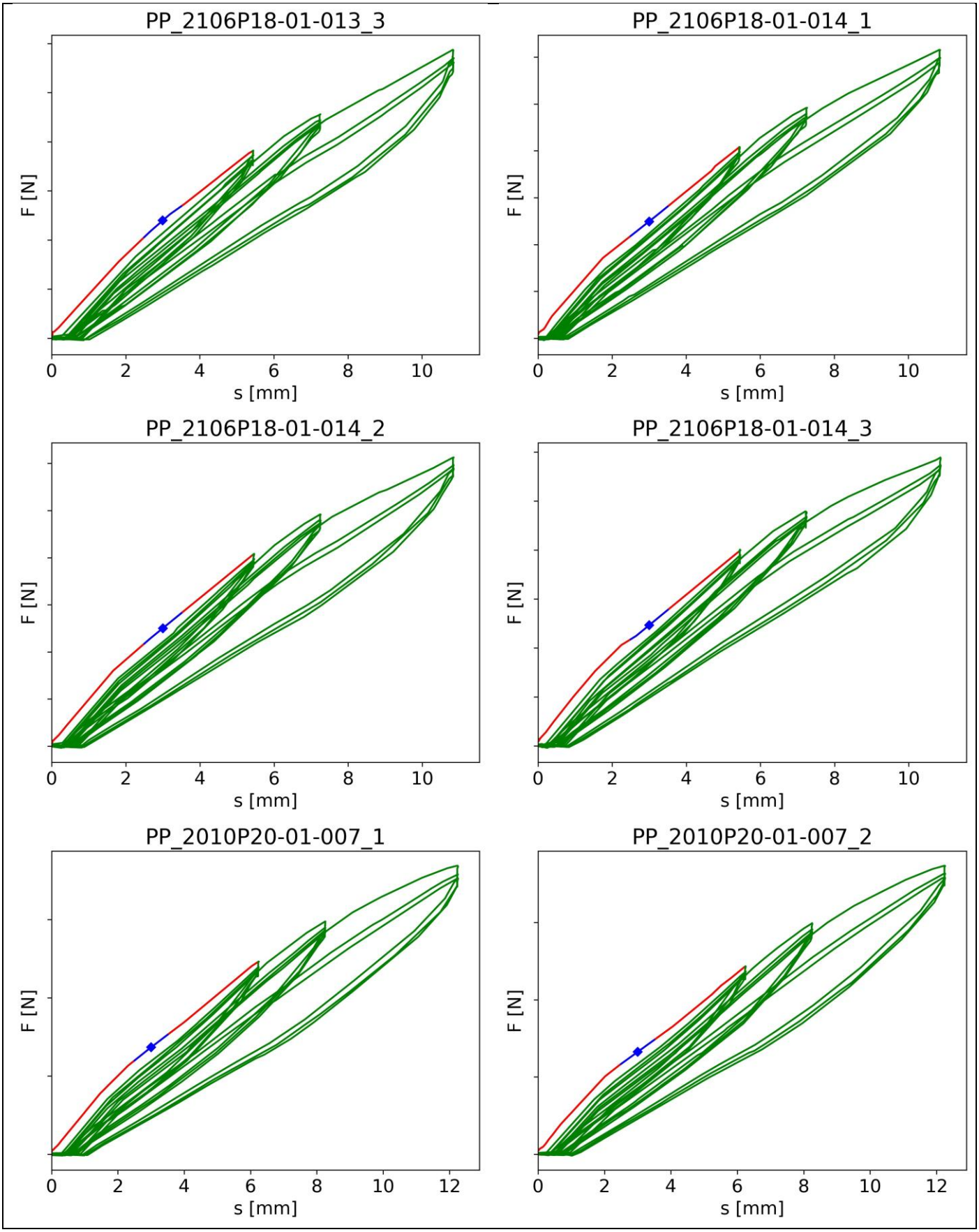
PP_2106P18-01-013_3
PP_2106P18-01-014_1
PP_2106P18-01-014_2
PP_2106P18-01-014_3
PP_2010P20-01-007_1
PP_2010P20-01-007_2
F [N]
s [mm]
0
2
4
6
8
10
12

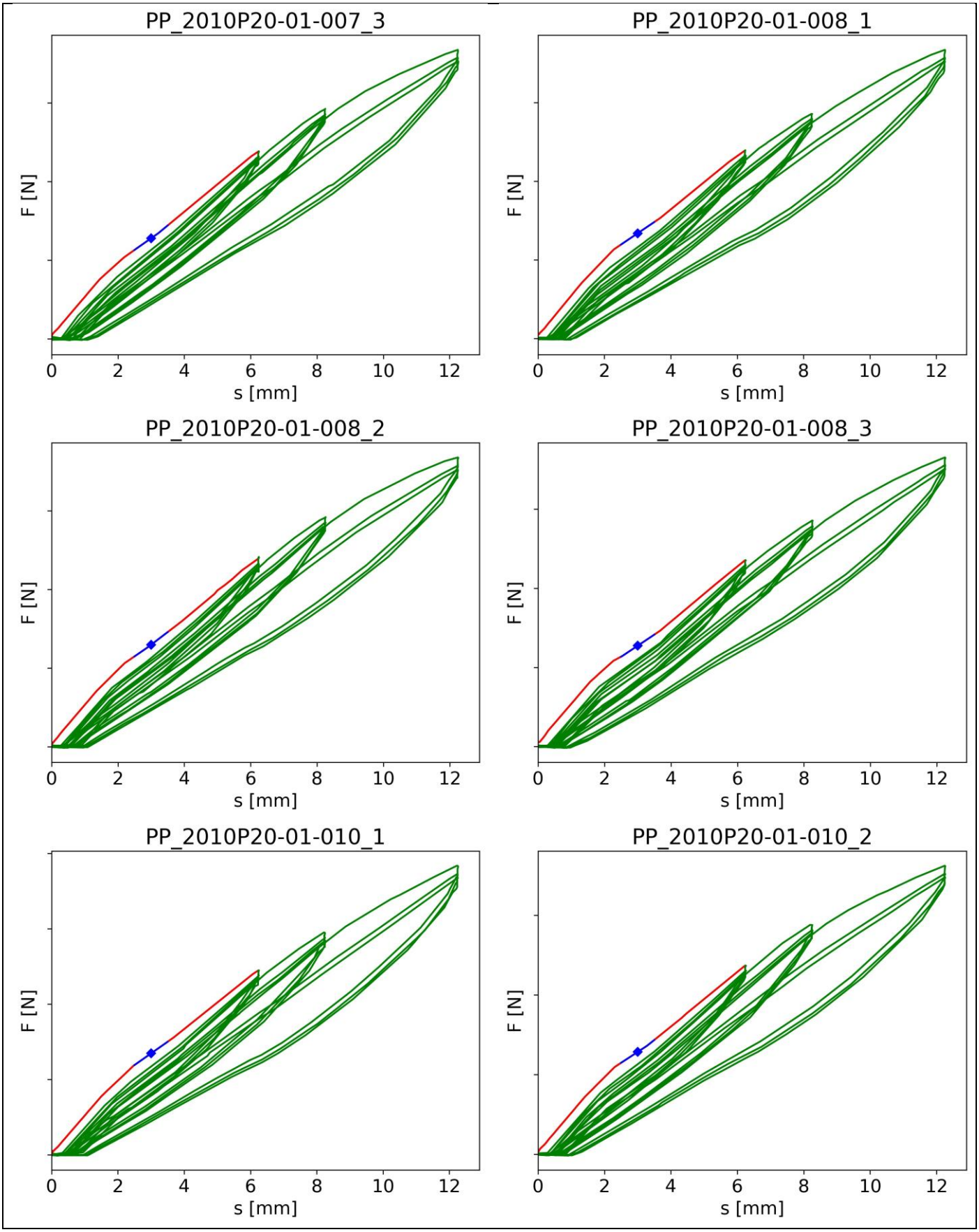
PP_2010P20-01-007_3
PP_2010P20-01-008_1
PP_2010P20-01-008_2
PP_2010P20-01-008_3
PP_2010P20-01-010_1
PP_2010P20-01-010_2
F [N]
s [mm]
0
2
4
6
8
10
12

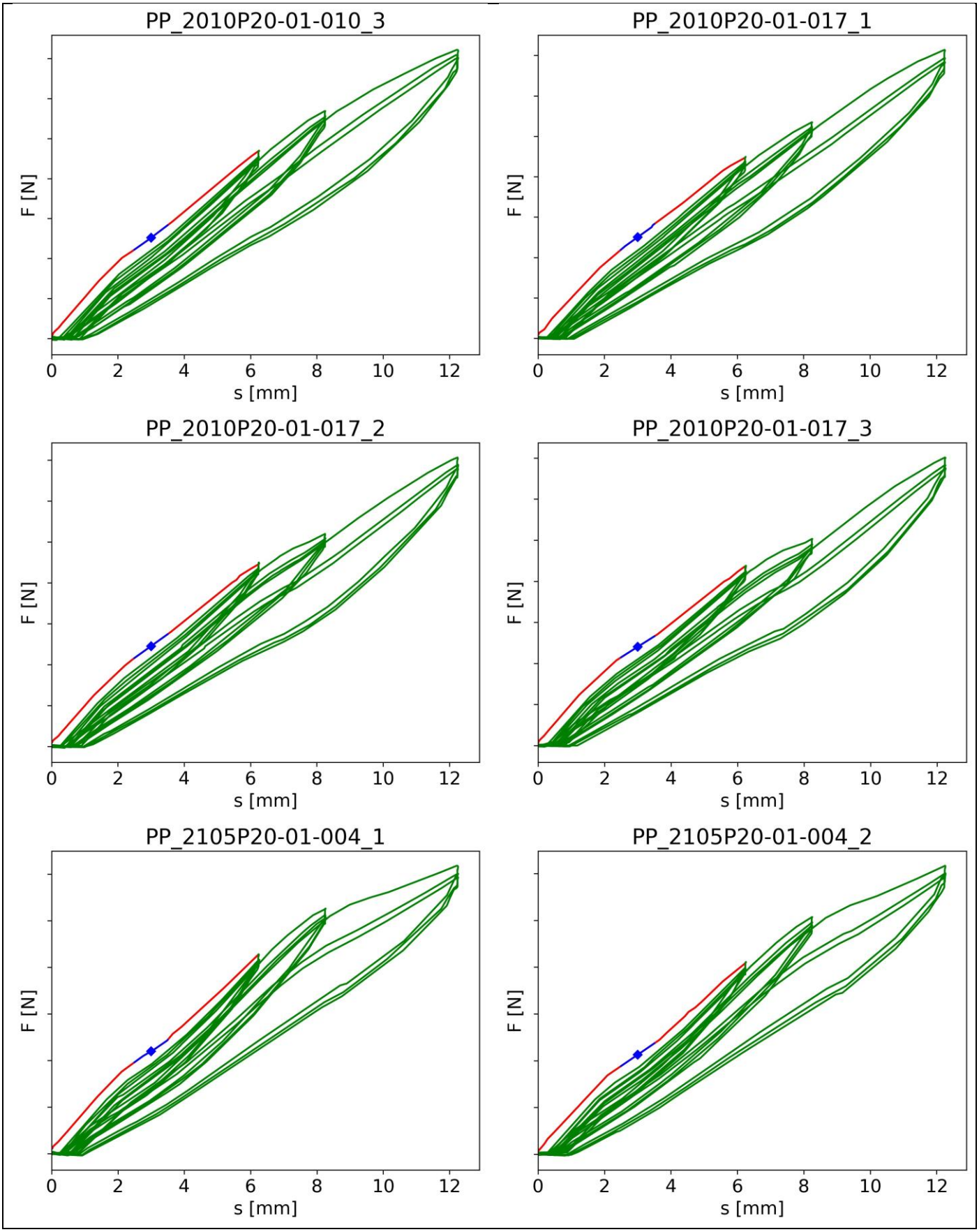
PP_2010P20-01-010_3
PP_2010P20-01-017_1
PP_2010P20-01-017_2
PP_2010P20-01-017_3
PP_2105P20-01-004_1
PP_2105P20-01-004_2
F [N]
s [mm]
0
2
4
6
8
10
12

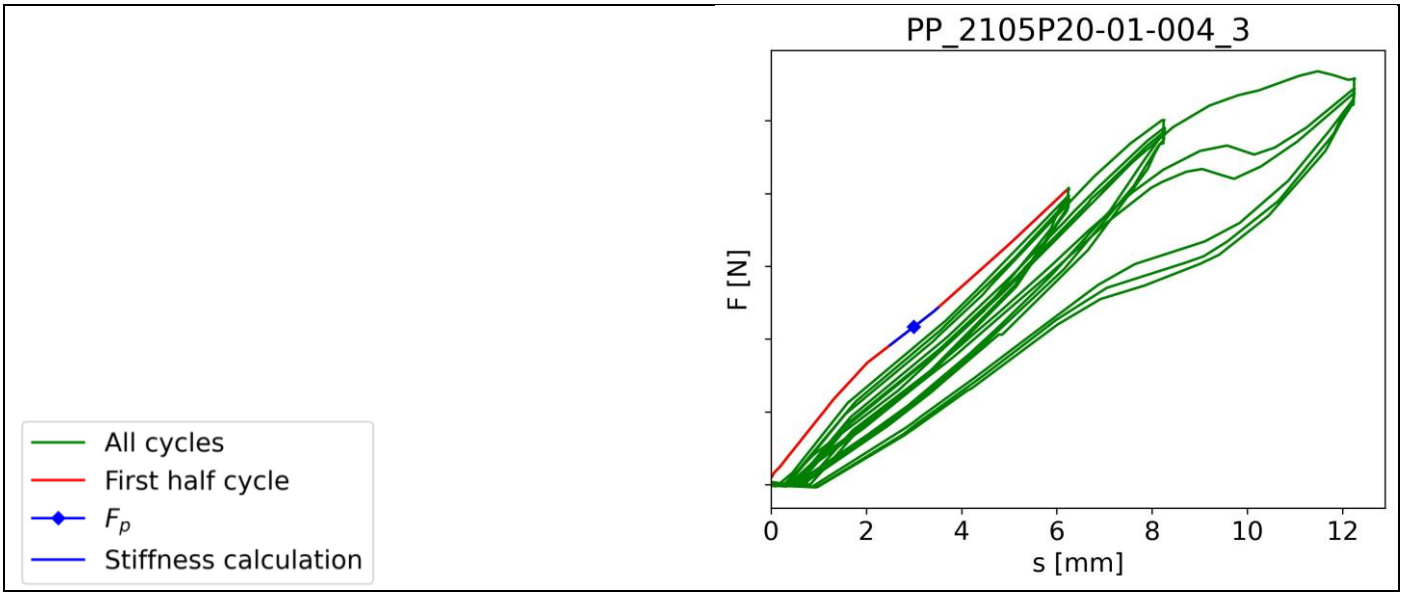
PP_2105P20-01-004_3
F [N]
s [mm]
0
2
4
6
8
10
12
All cycles
First half cycle
F_p
Stiffness calculation